CANADIAN THESES ON MICROFICHE

THÈSES CANADIENNES SUR MICROFICHE

National Library of Canada
Collections Development Branch

Canadian Theses on
Microfiche Service

Ottawa, Canada
K1A 0N4

Bibliothèque nationale du Canada
Direction du développement des collections

Service des thèses canadiennes
sur microfiche

NOTICE

The quality of this microfiche is heavily dependent upon the quality of the original thesis submitted for microfilming. Every effort has been made to ensure the highest quality of reproduction possible.

If pages are missing, contact the university which granted the degree.

Some pages may have indistinct print especially if the original pages were typed with a poor typewriter ribbon or if the university sent us an inferior photocopy.

Previously copyrighted materials (journal articles, published tests, etc.) are not filmed.

Reproduction in full or in part of this film is governed by the Canadian Copyright Act, R.S.C. 1970, c. C-30. Please read the authorization forms which accompany this thesis.

THIS DISSERTATION
HAS BEEN MICROFILMED
EXACTLY AS RECEIVED

AVIS

La qualité de cette microfiche dépend grandement de la qualité de la thèse soumise au microfilmage. Nous avons tout fait pour assurer une qualité supérieure de reproduction.

S'il manque des pages, veuillez communiquer avec l'université qui a conféré le grade.

La qualité d'impression de certaines pages peut laisser à désirer, surtout si les pages originales ont été dactylographiées à l'aide d'un ruban usé ou si l'université nous a fait parvenir une photocopie de qualité inférieure.

Les documents qui font déjà l'objet d'un droit d'auteur (articles de revue, examens publiés, etc.) ne sont pas microfilmés.

La reproduction, même partielle, de ce microfilm est soumise à la Loi canadienne sur le droit d'auteur, SRC 1970, c. C-30. Veuillez prendre connaissance des formules d'autorisation qui accompagnent cette thèse.

LA THÈSE A ÉTÉ
MICROFILMÉE TELLE QUE
NOUS L'AVONS REÇUE

Canada

NL 339 (r. 86/09)

National Library of Canada
Ottawa, Canada
K1A 0N4

Bibliothèque nationale du Canada

79

TC –	67334
ISBN	0-315-19426-X

CANADIAN THESES ON MICROFICHE SERVICE – SERVICE DES THÈSES CANADIENNES SUR MICROFICHE

PERMISION TO MICROFILM – AUTORISATION DE MICROFILMER

- Please print or type – Écrire en lettres moulées ou dactylographier

AUTHOR – AUTEUR

Full Name of Author – Nom complet de l'auteur
WILLIAM GEORGE TIGHE

Date of Birth – Date de naissance
11/12/53

Canadian Citizen – Citoyen canadien
☑ Yes / Oui ☐ No / Non

Country of Birth – Lieu de naissance
CANADA

Permanent Address – Résidence fixe
8321 112 street
Edmonton, Alberta
T6G 1K4

THESIS – THÈSE

Title of Thesis – Titre de la thèse
PLASMA DYNAMICS AND LASER-PLASMA INTERACTION IN THE CO_2 LASER-HEATED SOLENOID

Degree for which thesis was presented
Grade pour lequel cette thèse fut présentée
PhD

Year this degree conferred
Année d'obtention de ce grade
1985

University – Université
UNIVERSITY of ALBERTA

Name of Supervisor – Nom du directeur de thèse
DR. A.A. OFFENBERGER + DR. C. CAPJACK

AUTHORIZATION – AUTORISATION

Permission is hereby granted to the NATIONAL LIBRARY OF CANADA to **microfilm** this thesis and to **lend** or **sell copies of the film.**

The author reserves other publication rights, and neither the thesis nor extensive extracts from it may be printed or otherwise reproduced without the author's written permission.

L'autorisation est, par la présente, accordée à la BIBLIOTHÈQUE NATIONALE DU CANADA de **microfilmer** cette thèse et de **prêter** ou de **vendre des exemplaires du film.**

L'auteur se réserve les autres droits de publication; ni la thèse ni de longs extraits de celle-ci ne doivent être imprimés ou autrement reproduits sans l'autorisation écrite de l'auteur.

ATTACH FORM TO THESIS – VEUILLEZ JOINDRE CE FORMULAIRE À LA THÈSE

Signature
William Tighe

Date
March 26/1985

NL-91 (r. 84/03)

Canada

THE UNIVERSITY OF ALBERTA

PLASMA DYNAMICS AND LASER-PLASMA INTERACTION IN THE CO_2 LASER-HEATED SOLENOID

by

© William G. Tighe

A THESIS

SUBMITTED TO THE FACULTY OF GRADUATE STUDIES AND RESEARCH
IN PARTIAL FULFILMENT OF THE REQUIREMENTS FOR THE DEGREE
OF Doctor of Philosophy
IN
Electrical Engineering

Department of Electrical Engineering

EDMONTON, ALBERTA
Spring 1985

THE UNIVERSITY OF ALBERTA

RELEASE FORM

NAME OF AUTHOR William G. Tighe

TITLE OF THESIS Plasma Dynamics and Laser-Plasma Interaction in the CO_2 Laser-Heated Solenoid

DEGREE FOR WHICH THESIS WAS PRESENTED Doctor of Philosophy

YEAR THIS DEGREE GRANTED Spring 1985

Permission is hereby granted to THE UNIVERSITY OF ALBERTA LIBRARY to reproduce single copies of this thesis and to lend or sell such copies for private, scholarly or scientific research purposes only.

The author reserves other publication rights, and neither the thesis nor extensive extracts from it may be printed or otherwise reproduced without the author's written permission.

(SIGNED) William Tighe

PERMANENT ADDRESS:

8321 112 street
Edmonton, Alberta
Canada T6G 1K4

DATED March 18 1985

THE UNIVERSITY OF ALBERTA

FACULTY OF GRADUATE STUDIES AND RESEARCH

The undersigned certify that they have read, and recommend to the Faculty of Graduate Studies and Research, for acceptance, a thesis entitled 'PLASMA DYNAMICS AND LASER-PLASMA INTERACTION IN THE CO_2 LASER-HEATED SOLENOID' submitted by William G. Tighe in partial fulfilment of the requirements for the degree of Doctor of Philosophy in Electrical Engineering

A Offenberger
Supervisor

C R Capjack
Supervisor

C. R. James

External Examiner

Date March 18 1985

Dedication

With the warmest love and deepest respect I dedicate my thesis to my mother and to the enduring memory of my father. Their encouragement, confidence and pride in my work provided an unending source of motivation and inspiration.

Abstract

Several experimental and theoretical aspects of the laser-heated solenoid have been examined.

The use of a long pulse CO_2 laser in the production and heating of magnetically confined plasma columns is described. The propagation of heating (or bleaching) waves and shock waves along the axis of the solenoid is examined theoretically. From experimental observation, the axial behaviour is found to be well described by the self-regulated bleaching wave model of Burnett and Offenberger(1976).

The radial expansion of the column is shown to be strongly dependent on the focussing ratio of the laser input optics. With a fast focus (f/5) the early expansion rate is nearly twice that found with a slower arrangement (f/15). It is also found that a wider plasma column results with the faster focussing ratio. The radial behaviour is observed through radial density profiles taken at various times during the column development. A finite ionization time (~20 nsec) is observed and found to be in agreement with theoretical calculation. The rapid formation of a density minimum on axis, essential to the trapping of the laser beam, is verified. Short-lived density fluctuations are observed.

Energy balance is discussed. It is found that most of the laser energy is used in producing and heating of the plasma. Plasma temperatures of 40-50 eV are determined by the spectral shift observed in stimulated Brillouin spectra. These temperatures agree well with calculations based on energy balance. Thomson-scattered spectra show lower plasma temperatures of 20-30 eV. Numerical simulations indicate that only the central core of the plasma column reaches the higher temperatures. The scattered spectra involved an integration over colder plasma regions which likely accounts for the lower temperatures.

The long interaction length provided in this experimental arrangement, produced very high levels of both stimulated Brillouin (SBS) and stimulated Raman (SRS) scattering of the input laser light. Peak reflectivities of 20-25% have been observed with the SBS signal. These levels are in good agreement with calculations based on a convective growth model. The SRS signals are observed with peak reflectivities of .7%, found to be in good agreement with an absolute instability model.

The two-dimensional computer codes SHELL and HEATER, used to simulate the magnetohydrodynamic behaviour of the plasma in the laser-heated solenoid, are described. The HEATER subroutine follows the laser beam propagation and accounts for beam absorption, refraction and diffraction. Comparisons between experimental, computational, and theoretical results are given throughout and are, in most cases, found to be excellent.

Acknowledgements

I would like to thank my supervisor Dr. Allan Offenberger for his support (both scientific and financial) throughout the course of this study. I feel very fortunate to have been able to work with Dr. Offenberger. He is, to me, a model of the truly dedicated scientist and teacher. I am also indebted to Dr. Offenberger for allowing me to make use of the equipment in his research laboratory and for introducing me to members of the Laser-Plasma Physics community.

I would like to thank Dr. Clarence Capjack who also acted as a supervisor in this work. I am very grateful for his help with the computer codes and various aspects of plasma theory. His advice was always friendly and accurate. I also appreciate his financial support.

Much of the work presented in this thesis was only possible through the assistance of Drs. Don McKen, Robert Fedosejevs, and Wojciech Rozmus. Dr. McKen did much of the initial work in the design and construction of the apparatus. Dr. Fedosejevs did a great deal of work in the Brillouin and Raman studies and played a major role in their success. Dr. Rozmus contributed largely to the theoretical work associated with the Raman studies and was always available with insightful discussions. I learned a tremendous amount from these three scientists and I greatly value their friendship.

I would like to thank Dr. Jim McMullin, Dr. Richard Marchand and Mr. Steven Knudsen for their assistance in running the computer codes which were used in this study.

The funding for this project as provided by the governments of Canada and the Province of Alberta through ERRF (Energy Resources Research Fund) is gratefully acknowledged. I am very grateful for the financial support provided by the Department of Electrical Engineering in terms of teaching and research assistantships.

The technical support for this project was invaluable. I would particularly like to thank Mark Arnfield, Brian Betts, and Doug Whyte. The work of the machine shop staff, in particular Herb Gans and Gerry Soligo, was consistently fast, friendly and of the highest quality. A special thanks for the superb optics provided by Barry Arnold. Also for their technical and often philosophical advice, I am grateful to Doug Way-Nee and Martyn Billing.

For their friendship, co-operation and assistance, I must thank my fellow graduate students, Steven Au, Calvin Dormier, Randy Giles, Mohammed abdel-Halim, Rajender Razdan, Yarub al-Shiraida, Dennis Simeoni, Lori Small, Farouk Soliman, Ed Sumbar, and many others. For making life in the department a whole lot easier, a special thanks to Barbara Peck. I would like to thank my special friends Randy and Mary Giles, Richard Lamoureaux, Gary and Joan Margrave and Dean McKay for the good times spent in the mountains.

Finally but most importantly, I would like to thank my entire family. Their support was invaluable.

Table of Contents

Chapter Page

1. Introduction 1

1.1 Preliminary remarks 1

1.2 Motivation 1

1.3 Problems to be Investigated 4

1.4 Previous Work 5

1.4.1 Preliminary Remarks 5

1.4.2 Theoretical Considerations 6

1.4.2.1 Laser-Induced Breakdown 6

1.4.2.2 Laser Heating of Plasma 6

1.4.2.3 Laser Beam Propagation 8

1.4.2.4 Numerical Simulations 10

1.4.2.5 Stimulated Scattering 12

1.4.3 Review of Experimental Work 13

1.4.3.1 Stimulated Scattering 19

1.4.4 Results from this Study 21

2. Experimental Methods 24

2.1 Preliminary remarks 24

2.2 The Apparatus 25

2.2.1 The E-Beam CO_2 Laser 25

2.2.2 The Laser Cavity 26

2.2.3 The Solenoid Apparatus 28

2.2.4 The Solenoid 32

2.3 Diagnostic Techniques 37

2.3.1 Streak Photography 37

2.3.2 Interferometry 39

2.3.3 Thomson Scattering 42

2.3.4 Stimulated Scattering 50

2.3.5 Detection of the SBS Signal 51

2.3.6 Detection of the SRS Signal 52

3. Theory 54

3.1 Preliminary remarks 54

3.2 Laser-Induced Gas Breakdown 55

3.3 Laser Beam Absorption 62

3.4 Axial Wave Propagation 65

3.5 Optical Detonation 73

3.6 Radial Dynamics 76

3.7 Energy Balance and Plasma Heating 82

3.8 Two Dimensional Numerical Model 87

3.8.1 SHELL 87

3.8.2 HEATER 89

3.9 Stimulated Scattering 91

3.9.1 Preliminary Remarks 91

3.9.2 General Mechanisms 92

3.9.3 Stimulated Brillouin Scattering 95

3.9.4 Stimulated Raman Scattering 97

4. Experimental Results and Observations 104

4.1 Preliminary Remarks 104

4.2 Axial Development 105

4.2.1 Results and Analysis 105

4.3 Radial Behaviour 113

4.3.1 Radial Streak Photography 113

4.3.1.1 Results and Analysis 115

4.3.2 Radial Density Profiles 119

4.4 Stimulated Scattering 136
4.4.1 Stimulated Brillouin Scattering, SBS .136
4.4.2 Stimulated Raman Scattering, SRS 145
4.4.3 Thomson Scattering Results 151
5. Simulation Results 159
5.1 Preliminary Remarks 159
5.2 Simulation Runs 160
5.3 Simulation Results, 3-D Representations 161
5.4 Simulation Results, 2-D Profiles 176
5.4.1 Axial Effects 180
5.4.2 Radial Effects 190
5.5 Concluding Remarks 198
6. Summary and Conclusions 199
6.1 Preliminary Remarks 199
6.2 Summary of Results 199
6.2.1 Axial Propagation 199
6.2.2 Radial Behaviour 203
6.2.3 Plasma Density and Temperature 205
6.2.3.1 Density 205
6.2.3.2 Temperature 207
6.2.4 Stimulated Scattering 209
6.3 Problems for Further Investigation 209
6.4 Final Conclusions 211
References 213

List of Tables

Table Page

5.1 Run Parameters used in Simulation Study 162

5.2 Average Parameters behind Axially Propagating Front 186

List of Figures

Figure Page

1.1 The Laser-Heated Solenoid: Basic Arrangement 2

2.1 CO_2 Laser Pulse Shape 27

2.2 Laser-Heated Solenoid: Basic Experimental Arrangement 29

2.3 Axial Variation of the Hydrogen Fill Pressure 31

2.4 Axial Variation of the Magnetic Field Strength 33

2.5 Magnetic Field: Temporal Variations 35

2.6 Streak Photographs:
a) Axial (f/5 focus) and b) Radial (f/15 focus) 38

2.7 Relation between Incident and Scattered Radiation in Thomson Scattering 43

2.8 Experimental Arrangement for Thomson Scattering 45

3.1 Dependence of Radial Expansion on B-field Strength and Plasma Density: Ion Transport Model 79

4.1 Axial Streak Photographs:
a) Split Solenoid (f/5 focus)
b)Single Solenoid (f/15 focus) 106

4.2 Axial Propagation of the Plasma Column: Fill Pressures from 7-25 Torr, Laser Energies from 300-500 Joules 108

4.3 Temporal Dependence of the Axial Propagation of the Plasma Front: Experimental Parameters as in Figure 4.2 110

4.4 Axial Velocity of Plasma Front vs Laser Intensity and Hydrogen Fill Pressure 111

4.5 Radial Streak Photographs (Single Solenoid-f/15 focus) 114

4.6 Radial Propagation of the Plasma Column 117

4.7 Interferograms (Single Solenoid-f/5 focus):
a) no plasma, b) plasma front, c) plasma column
(arrows indicate location of fringe shifts) 120

4.8 Late-time Interferogram Fringe and Density Profile, 4.5 cm from the focal region using f/15 focussing 123

4.9 Density Profile Sequence at the Breakdown Front, 4.5 cm from the focal region, using f/15 focussing: z=the distance from the front 125

4.10 Density Profile Sequence at the Breakdown Front, 1.0 cm from the focal region, using f/5 focussing: z=the distance from the front 127

4.11 Perturbed Interferogram Fringe and Differentially Inverted Density Profile 129

4.12 Density Profile Sequence at the Breakdown Front, 10.0 cm from the focal region, using f/5 focussing 131

4.13 Density Profile Sequence at the Breakdown Front, 10.0 cm from the focal region, using f/5 focussing 132

4.14 Late-time Interferogram Fringe and Density Profile, 10.0 cm from the focal region using f/5 focussing 135

4.15 CO_2 (upper beam) and SBS signal (lower beam) Oscilloscope Traces for varying Experimental Conditions 137

4.16 SBS Results: Reflectivity versus Laser Intensity 139

4.17 SBS Results: Input, Output and Theoretically Fitted Spectra 142

4.18 SBS Results: Prompt and Delayed Spectra 144

4.19 CO_2 (upper beam) and SRS signal (lower beam) Oscilloscope Traces.
a) and b) from different laser shots but similar experimental conditions 146

4.20 SRS Results: Reflectivity versus Laser Intensity 148

4.21 SRS Results: Spectral Characteristics 149

4.22 Thomson Scattering Data (Raw and Smoothed): T=60 nsec (3.17 A/Channel) 153

4.23 Thomson Scattering Data (Raw and Smoothed): T=250 nsec (3.17 A/Channel) 154

4.24 Thomson Scattered Experimental and Theoretical Profile: T=60 nsec (3.17 A/Channel) 155

4.25 Thomson Scattered Experimental and Theoretical Profile: T=250 nsec (3.17 A/Channel) 156

5.1 Laser Profile used in Simulation Study 163

5.2 Electron and Ion Temperature Distributions: Simulation Run 7 at T=100 nsec 165

5.3 Plasma Density and Laser Absorption Distributions: Simulation Run 7 at T=100 nsec 166

5.4 Laser Flux Distribution: Simulation Run 7 at T=100 nsec 168

5.5 Axial and Radial Ponderomotive Forces: Simulation Run 7 at T=100 nsec 170

5.6 Electron and Ion Temperature Distributions: Simulation Run 7 at T=300 nsec 173

5.7 Plasma Density and Laser Absorption Distributions: Simulation Run 7 at T=300 nsec 174

5.8 Electron Temperature and Density Distributions: Simulation Run 8 (lower initial density) 175

5.9 Electron Temperature and Density Distributions: Simulation Run 3 (higher initial density) 177

5.10 Electron and Ion Temperature Distributions: Simulation Run 11 at T=300 nsec 178

5.11 Plasma Density and Laser Absorption Distributions: Simulation Run 11 at T=300 nsec 179

5.12 Axial Profiles of Temperature and Density for Simulation Run 5 181

5.13 Axial Profiles of Temperature for Simulation Runs 2 and 8 183

5.14 Axial Propagation of Plasma Front: Simulation Runs 5, 2 and 8 184

5.15 Axial Profiles of Temperature and Density for Simulation Run 15 188

5.16 Radial Profiles of Temperature and Density for Simulation Run 5 191

5.17 Radial Profiles of Temperature and Density for Simulation Run 15 193

5.18 Radial Propagation of Plasma Column: Simulation Runs 5 and 15 194

5.19 Radial Profiles of Density for Simulation Runs 8 and 2 196

5.20 Radial Profiles indicating Thomson Scattering Experimental Conditions from Simulation Run 5 197

6.1 Summary of a) Axial and b) Radial Plasma Dynamics. Experimental, Modelling, and Theoretical Conditions are Described in the Text. 200

6.2 Summary of a) Density and b) Temperature Characteristics of the Plasma Column. Experimental, Modelling, and Theoretical Conditions are Described in the Text. 201

CHAPTER I

Introduction

1.1 Preliminary remarks

The laser-heated solenoid is a plasma device in which the plasma is confined radially by a solenoidal magnetic field and heated by laser energy. A basic system is shown in Figure 1.1.

In this experiment, the core of the solenoid is filled with hydrogen gas. A CO_2 laser pulse is focussed into the gas, the gas breaks down and forms the initial plasma. With further absorption of laser energy, the plasma, confined radially but free to expand axially, develops into a long column.

The formation of the plasma column, the characteristics of the plasma (the temperature and density) and the interaction of the laser with the plasma are the main areas investigated in this study.

1.2 Motivation

The primary motivation for this study was provided by a fusion reactor scheme suggested by Dawson et al.(1971). This proposal was based on the heating of a magnetically confined plasma using a high power laser.

A fusion reactor requires plasma temperatures of ~10 keV while the required density depends on the confinement time, τ, as given by the Lawson criteria;

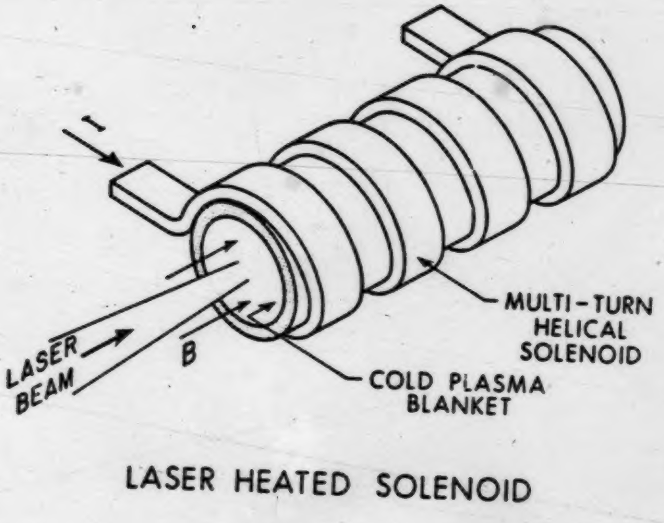
I
LASER BEAM
B
MULTI-TURN HELICAL SOLENOID
COLD PLASMA BLANKET
LASER HEATED SOLENOID

Figure 1.1 The Laser-Heated Solenoid: Basic Arrangement

$$n\tau > 10^{14}\ \mathrm{cm^{-3}sec} \qquad (1.1)$$

For the laser-heated solenoid reactor scheme, densities of 10^{17}-10^{18} cm^{-3} were suggested. The magnetic field strength required to radially confine such a plasma was found to be ~400-450 kG. Moreover, to keep axial losses in the same order as the radial losses, a solenoid several hundred meters long was indicated.

The CO_2 laser was proposed as the source of the input energy. This laser is comparatively efficient and capable of high energy, long pulse output. A major consideration in the selection of the CO_2 laser is that, under the described plasma conditions, the absorption length of its 10.6 μm radiation very closely matches the length of the proposed device. A ~1000 kilojoule and several 100μsec long laser pulse would be required to heat the plasma to the desired thermonuclear temperatures.

Recently, Suckewer et al.(1983) have proposed that a device similar to the laser-heated solenoid could be used in x-ray laser development. In initial experiments a ~500 joule, 60-70 nsec CO_2 laser pulse was used to produce a plasma with peak electron temperatures of 100-400 eV and electron densities of $(1\text{-}3)\cdot 10^{18}$cm^{-3}. The plasma was formed from either solid (Carbon and Teflon) or gaseous (CO_2, O_2, and Ne) targets and was confined radially by a 50-90 kG magnetic field. These parameters closely match those used in the experimental and numerical simulation studies of the laser-heated solenoid. These developments, therefore, provide further motivation for these investigations.

1.3 Problems to be Investigated

Aside from the questions involved in developing the very high energy, long pulse CO_2 laser and the very long linear magnetic solenoid, many questions concerning the interaction of the laser and plasma are raised by the proposed reactor and x-ray laser schemes.

Crucial to the concept of heating long plasma columns is the trapping of the laser energy by the plasma. Theoretically, it is well known that a density minimum on axis can effectively trap the laser energy. This is due to the negative refractive index of an ionized gas. As the laser diverges from a low density region on the axis to higher density regions, it is refracted back toward the axis. If the radial density profile is parabolic then the beam will refocus and propagate in the plasma much as in a waveguide. The formation and stability of the trapping density profile can be investigated experimentally.

In the laser-heated solenoid the expected mechanism by which the laser energy is absorbed by the plasma is classical inverse bremsstrahlung. Most of the energy is absorbed by the electrons and then collisionally transferred to the ions. It is important that the ions be heated at the same rate as the electrons to avoid thermal runaway and less effective heating of the ions. The energy transport processes and overall energy balance questions must be carefully examined.

The bleaching effect, whereby successive layers of plasma are heated and made transparent to the incident laser radiation, is important for efficient and uniform heating of the plasma. The effect is characterized by the propagation of a heating wave. During this process the plasma remains effectively stationary. Alternatively, plasma motion may become significant allowing axial shock waves to develop resulting in non-uniform heating. Experimentally, these processes may be distinguished by their different temporal, plasma-density and laser-intensity dependencies.

Finally, the interaction of the laser and the plasma may lead to non-linear effects such as stimulated Brillouin scattering and stimulated Raman scattering. These processes could alter the laser-plasma coupling and their role must be investigated.

1.4 Previous Work

1.4.1 Preliminary Remarks

In this section, an outline of background material will be presented with emphasis on the results from other laser-heated solenoid experiments. Many of these results will be considered in detail in later chapters. A comprehensive review of research related to the laser-heated solenoid up to ~1976 is provided by Kristiansen and Hagler(1976).

1.4.2 Theoretical Considerations

1.4.2.1 Laser-Induced Breakdown

Observation of laser-induced breakdown in gases was generally explained by electron avalanche ionization. In this process, seed electrons are accelerated in the electric field of the laser, reach the ionization energy and produce further free electrons via electron-neutral collisions. In the case of high intensity lasers, multiphoton ionization was also considered as a mechanism.

A breakdown wave, propagating back from the laser focus toward the laser, was observed (Ramsden and Davies(1964)) and explained by an optical detonation process (Ramsden and Savic(1964), Raizer(1965)). Here, an ionizing shock front expands outward from the laser focus. Incoming laser energy is strongly absorbed in this ionized gas and so, the absorbing region propagates back toward the laser.

1.4.2.2 Laser Heating of Plasma

The heating of materials with laser radiation was studied by many authors (Afanse'ev(1966), Dawson(1964), Krokhin(1965)). This led to the investigations of Dawson et al.(1971) into the use of high-power, long-wavelength lasers to heat magnetically-confined plasmas to fusion temperatures.

Rehm(1970) studied the effect of laser heating on a plasma. If the plasma length is greater than the absorption length for the incoming laser energy, then Rehm described the plasma response in terms of two temporal parameters and showed that either a heating wave or a shock wave may result. In effect, at early times no plasma motion is induced and successive layers of the plasma are heated and made transparent to the laser radiation. This is the heating or bleaching wave solution. At later times, induced plasma motion leads to the development of a shock wave. The time scale for the phenomena depends on the rate at which energy is added to the plasma and the rate at which it can be convected away.

Laser heating of a plasma was also considered by Steinhauer and Ahlstrom(1971a, 1971b, 1974). The time scales involved were very short (sub-nanosecond) so that plasma motion was not considered. Axially non-uniform and magnetically confined plasmas were treated and plasma responses similar to the bleaching wave solution were found.

Burnett and Offenberger(1976) developed a bleaching wave model which involved a matching of the plasma length and the laser absorption length. Expressions derived for the length of the plasma column and the velocity of the bleaching front were verified through comparisons with one-dimensional computer simulations. It was further proposed that the axial propagation was self-regulating and that the Alfven velocity would represent a maximum value.

Ahlborn et al.(1982) used an optical detonation model to describe the formation of plasma columns in a solenoidal field. In this model, the laser energy is absorbed in a very narrow region of the plasma column. As it expands, the shock front propagates axially, ionizing the neutral gas as it goes. By analyzing details of the shock transition, a propagation velocity was obtained. A self-regulating mechanism was proposed resulting in a uniform velocity depending only on the plasma density and the laser intensity. Behind the front an equilibrium column is described. Here the power absorbed is balanced by the power lost through conduction and radiation. An expression for the maximum temperature on axis was determined.

1.4.2.3 Laser Beam Propagation

Associated with the question of the heating of the plasma is the question of the propagation of the laser beam through the plasma.

Trapping of the laser beam has been shown to occur when the radial density profile has a minimum on axis. This is a so-called favorable density profile. Using geometric optics, Steinhauer and Ahlstrom(1971a) showed that with a parabolic density profile the laser beam is, indeed, trapped and is, furthermore, characterized by periodic focussing and de-focussing.

Feit and Fleck(1976) treated the laser beam propagation and plasma heating self-consistently. Starting with an initially uniform radial density distribution, numerical calculations showed that as the plasma was heated, it expanded and created a favorable density profile. Though only followed over very short distances, beam trapping was observed and found to display periodic focussing and de-focussing.

Mani et al.(1975) used normal mode analysis in studying the problem of laser beam propagation in a plasma. By considering a Gaussian beam in an axially uniform plasma with a parabolic radial density profile, it was verified that the laser beam was trapped and displayed total periodicity. McMullin et al.(1978, 1979a) applied normal mode analysis to the more general problem of beam propagation in an axially varying, absorbing plasma, with a radial density profile characterized by a density minimum on axis but including non-quadratic terms. It was shown that even small departures from a parabolic profile resulted in severe aberration of the beam.

Feit et al.(1977) again treated the problem of beam propagation in a plasma. By making simplifying assumptions, the plasma heating and beam propagation were separated allowing numerical calculations to be made over long plasma lengths. The electron density profile again developed with a minimum on axis. The profile shape, however, was non-quadratic and the beam, while trapped, exhibited extreme aberration. It was felt that the loss of periodicity would remove possible difficulties of resonant interaction of the beam with density variations in the plasma.

1.4.2.4 Numerical Simulations

A number of computer codes have been developed to simulate the processes encountered in the laser-heated solenoid. The 2-dimensional calculations of Feit and Fleck(1976) have been mentioned and while quite complete, the code was limited to short distances (a few centimeters) and short time periods (a few nanoseconds).

Burnett and Offenberger(1976) developed a 1-dimensional Lagrangian code with which the radial dynamics of the laser-heated solenoid was followed. The code was used to follow the heating and radial expansion of an initially cold (1 eV) but fully ionized plasma under the influence of a strongly focussed, short ($\sim$20 nsec), Gaussian laser pulse ($\sim$25 joules). The processes were followed out to $\sim$40 nsec with and without a confining magnetic field. A radial shock was observed to develop very quickly and propagate outward at a nearly constant velocity ($\sim 4.5 \cdot 10^6$ cm/sec). With the application of a magnetic field the shock intensity and velocity were seen to decrease ($\sim 2.5 \cdot 10^6$ cm/sec). The inhibiting effect of the magnetic field also led to higher temperatures.

Burnett and Offenberger(1976) also dealt with the heating of a plasma column with a long duration (15 μsec) laser pulse. In this case, inertial terms in the governing equations were ignored. In particular, it was assumed that magnetic field convection would dominate magnetic field diffusion and that thermal conduction would exceed thermal convection. It was shown, however, that this does not put unrealistic constraints on the model. The behaviour of the plasma radius, temperature, and density was followed through the duration of the laser pulse for varying magnetic field strengths. With stronger fields, radial confinement was enhanced and electron temperatures were dramatically increased.

A 2-D model of the laser-heated solenoid was described by McMullin et al.(1979b). The magnetohydrodynamic equations were transformed using the magnetic field lines as a co-ordinates. The laser was assumed to propagate with constant radius and absorption of the laser energy was through inverse bremsstrahlung. Initially, the plasma was taken to be fully ionized and at a temperature of 1 eV. The plasma density was uniform at a value of $2x10^{14}cm^{-3}$. Processes were followed for 1 μsec through 5 cm. In good agreement with experiment, the simulations showed a bleaching front propagating axially at a velocity of ~6 cm/μsec. The plasma behind the front reached temperatures of 40-45 eV. A density minimum on axis was clearly established behind the bleaching front. At the front a strong axial shock was seen to develop.

Makomaski and Pietrzyk(1980) also give results from a 2-D simulation of the laser-heated solenoid. In this code, the laser beam was initially focussed and then individual rays were followed. Absorption by inverse bremsstrahlung was included but refraction of the rays was not considered. With time, then, the outer rays were absorbed in higher density regions and only the central rays continued to propagate. The beam, then, became increasingly narrow near the front. A result of this was that while at early times an axial shock did develop, it was seen to decay after ~280 nsec.

A radial shock, as seen in the 1-D models, was observed to develop rapidly, producing a density minimum on axis. With initial conditions similar to those used by McMullin et al.(1979b), plasma temperatures were seen to rise to 40-50 eV which agrees well with other models and experiment. These simulations also showed that only a small percentage (~10%) of the total energy of the plasma was involved with plasma motion. This indicates that bleaching wave models which ignore this motion should describe the plasma response reasonably well.

1.4.2.5 Stimulated Scattering

In laser-heated solenoid experiments both stimulated Brillouin and stimulated Raman scattering have been observed. However, it is the coupling of high intensity laser pulses to solid targets, as used in studying inertial confinement fusion (ICF), which has provided much of the motivation for understanding stimulated scattering processes.

A large amount of theoretical work has been done into the nature of these phenomena. Drake et al.(1975) and Forslund et al.(1975a) have dealt fairly completely with the formalism for both SBS and SRS. Descriptions of the processes and aspects of the theory will be included in Chapter 3.

In the work outlined in this thesis, the SBS and SRS data have been used, primarily, to determine the condition of the plasma.

1.4.3 Review of Experimental Work

The proposals of Dawson et al.(1971) prompted the use of CO_2 lasers to heat underdense plasmas and to investigate the phenomena encountered in the laser-heated solenoid.

Johnson and Chu(1974a) used a 30 joule, 150 nsec CO_2-laser pulse to ionize helium at pressures of ~30 torr. The evolution of the electron density profile was followed and showed the rapid formation of a minimum on axis. The effects of beam trapping in this favorable density profile were reported. The propagation of a radial shock was observed and found to be in good agreement with the 1-D MHD model of Burnett and Offenberger(1974). The preservation of these phenomena in the presence of a confining magnetic field was reported by Johnson and Chu(1974b).

The effect of a strong magnetic field on laser-induced breakdown was studied by Cohn et al.(1972). It was observed that with an applied magnetic field, the gas pressure at which breakdown occurred was significantly reduced. The effect was found to be particularly significant at lower gas pressures (<100 torr) and was explained in terms of a reduction in electron diffusion from the focal region.

Magnetic effects were further investigated by Loter et al.(1974). Detailed measurements of the evolution of the plasma temperature during breakdown were reported. It was observed that while higher temperatures were reached without a magnetic field, the rate at which the temperature dropped was significantly reduced with the application of the field.

Research programs dealing directly with the laser-heated solenoid were initiated by several groups. Methods were developed to eliminate the gas in the focussing region and thereby prevent the development of the backward travelling wave and allow the formation of long plasma columns. The primary questions addressed by this research were the effectiveness of the laser-plasma coupling, the radial and axial dynamics of the plasma column, and the evolution of the plasma density and temperature.

Rutkowski et al.(1975) used a puff-filling technique to supply gas to the plasma tube. A small orifice restricted gas flow out of the plasma tube and into the evacuated, laser-focussing region. The orifice was made just large enough to allow the laser energy to pass into the gas. Approximately 28 torr of hydrogen was puffed into the plasma tube which was placed in the core of a solenoid. The solenoid provided radially confining fields with strengths up to 100 kG. An electron-beam controlled CO_2 laser provided ~1 μsec pulses with energies up to 250 joules.

Rutkowski et al.(1975) reported the production of plasma columns 12-20 cm in length. The presence of a density minimum on axis was clearly shown though it was shown to be more difficult to establish such a favorable density profile in the presence of a strong magnetic field. The plasma temperature also displayed a dependence on the magnetic field. With a confining field, maximum temperatures of ~130 eV were observed while with no field the diagnostic technique implied an upper bound of 70 eV for the plasma temperature. It was felt that the temperature measurements reflected plasma conditions only in a very narrow region in the centre of the plasma column.

The axial and radial dynamics of the plasma boundary were reported. Radial confinement in the presence of the magnetic field was clearly demonstrated. The axial propagation was very nearly constant. Velocities of 6 cm/μsec were reported in the unmagnetized case while in the magnetized case the velocity was significantly slower at 3 cm/μsec. Identification of the mechanism (i.e. bleaching wave or detonation wave) for axial propagation was not resolved.

Offenberger et al.(1976a) reported the production of 20 cm plasma columns in a solenoidal magnetic field. In this experiment, a large gas reservoir was used to fill both the core of the solenoid and the laser-focussing region. Prior to firing the laser, the focussing region was rapidly evacuated. Again, a small aperture was used to prevent gas flow from the solenoid core and thereby provide an effective gas-vacuum interface.

A CO_2 laser provided ~1μsec pulses with energies up to 125 joules. The solenoid provided field strengths up to 110 kG. Hydrogen gas at fill pressures up to 20 torr was used.

The observed axial dynamics of the plasma column contrasted in some respects to that reported by Rutkowski et al.(1975). The application of the magnetic field was seen to increase, not decrease, the propagation velocity of the breakdown front. The longer columns were produced with an applied field and not without, as previously reported. The velocity of the front was not uniform but was initially rapid and then decreased with time.

Confinement of the radial expansion by the magnetic field was demonstrated. As the magnetic field strength was increased, the plasma radius decreased. At maximum field strengths, a nearly constant radius was observed over the entire plasma length. Collimated laser energy at the output end of the solenoid was observed only in the presence of a plasma column. This provided strong evidence of a radial density profile favorable to laser beam trapping.

Dufresne et al.(1978) described experiments in which a high energy (200 joule), long pulse (1-2μsec) CO_2 laser was used to produce 8 cm plasma columns confined by a 60 kG solenoidal field. A puff-filling technique similar to that described by Rutkowski et al. was used. The core was filled with hydrogen gas at pressures of 5 - 55 torr.

The dependence of the velocity of the axial front on the ratio of laser energy flux, W, to gas density, ρ, was investigated. The velocity measurements were made 300 nsec following the initial breakdown. W/ρ values ranged from $5\mathrm{x}10^{20}$-$8\mathrm{x}10^{21}$ cm^{3}sec^{-3} with the results showing three distinct propagation regimes. At high laser intensity and low pressure, the velocity dependence was characteristic of a bleaching wave. At low laser intensity and high pressure, the velocity dependence was characteristic of a subsonic, deflagration-like shock wave. In the intermediate range, a supersonic shock described the propagation of the front. The theoretical model of Ahlborn and Zuzack(1969) was used to explain the different regimes.

Scudder et al.(1978) and Scudder(1979) describe a detailed study of the axial breakdown wave in the laser-heated solenoid. The experimental arrangement was similar to that used by Rutkowski et al.(1975). The plasma columns (up to 40 cm long) were produced with 1μsec, 400 joule, CO_2-laser pulses focussed onto hydrogen gas (from 5 to 30 torr) and confined with a 100 kG magnetic field.

The radial and axial growth of the plasma were studied under varying plasma density and laser intensity conditions. Radial density profiles showed the formation of favorable trapping profiles at various axial positions. The longest columns were obtained in the presence of the magnetic field. Without the field the propagation effectively stopped when the laser pulse stopped. With a magnetic field the column continued to develop for several microseconds following the termination of the laser pulse. In general, the axial velocity was initially rapid followed by a period of slower propagation.

In order to distinguish between bleaching and detonation mechanisms for the axial propagation, the dependence of velocity on filling density was examined. The density dependence was found to be weak although at high densities ($\sim 2\text{x}10^{18}$ cm^{-3}) the data agreed quite well with a bleaching model. The velocity dependence on the laser power was also investigated. In this case, a bleaching model was found to give a good fit to the data.

At late stages of the column development ($\sim 1\mu$sec after the initial breakdown), Scudder et al.(1978) noted that sharp compressions developed at the breakdown front. The densities here reached twice the initial fill density, indicating the development of a shock front. Also at these later times, the breakdown front was observed to be very narrow, often less than the initial laser spot size. This was interpreted as being due to strong refraction of the laser beam.

Scudder(1979) concluded that at all densities, significant axial fluid motion was induced after $\sim 1\mu$sec, indicative of a shock wave. At earlier times and higher densities, a heating wave model predicted both the velocity and the temperature behaviour of the plasma column. At lower densities, however, neither model gave good agreement with the data. This was explained as being primarily due to ionization effects which were not included in bleaching wave models. Scudder(1979) considered, in detail, several mechanisms which could provide ionization ahead of the heating wave. It was concluded that electron thermal conduction was the only likely process and that it may limit the wave propagation, particularly at lower densities.

1.4.3.1 Stimulated Scattering

Offenberger et al.(1976b) observed stimulated Brillouin scattering from the underdense plasma of the laser-heated solenoid. The CO_2 laser used to create the plasma column also interacts with the plasma to generate SBS. By spectrally resolving the back-scattered radiation and using a kinetic approach to the scattering process, the electron and ion temperatures were calculated. The results were found to be in good agreement with estimates from 1-D calculations and from other experimental evidence. By varying the input laser intensity, the SBS growth rate was determined and it compared favorably with that expected for a convective instability.

The SBS radiation was seen to be related to the initial gain-switched spike of the input laser pulse. No saturation of the signal was observed and the peak backscattered power level was ~.2% of the incident power.

Using the experimental arrangement described by Rutkowski et al(1975), Massey et al.(1976) also observed SBS radiation from the laser-heated solenoid. Here, however, a saturation power reflectivity level of $\sim 5\%$ was observed.

Measured electron temperatures and estimated ion temperatures were used to determine expected wavelength shifts for the scattered radiation. These calculations were based on coherent-wave theory of the scattering. The calculated shifts compared well with the measured shifts.

Measurements of stimulated Raman scattering from an underdense plasma were first reported by Watt et al.(1978). In this experiment a CO_2 laser pulse (with focussed intensities up to 3×10^{9} W/cm^2) was fired into a low density (2×10^{16} cm^{-3}), low temperature (15 eV), 20 cm plasma column produced in a theta-pinch device. The non-linearity of the signal was verified and spectral shifts were measured and used to identify the scattered signal as SRS radiation. Total SRS reflectivity levels of $\sim 10^{-4}\%$ were reported.

Higher reflectivity levels of SRS ($\sim 10^{-2}\%$) were reported by Watt and Pietrzyk(1980). In this case, a CO_2 pulse was incident on a preformed and compressed plasma column in a fast-solenoid device. The plasma conditions (temperatures of 30-60 eV, densities of $\sim 3.5\times10^{17}$cm^{-3}) in this device are similar to those in the slow solenoid but are expected to be more uniform over the column length and so be more conducive to the SRS process.

Again, the non-linearity of the process was determined and the spectral measurements showed similar behaviour to those previously reported. The nonlinear scaling and growth rate calculations were used to suggest that the process represented an absolute rather than convective instability.

In the laser-heated solenoid experiments reported by Scudder(1979), low levels of SBS (reflectivities of 1-2 %) and no SRS signals were observed.

1.4.4 Results from this Study

The experimental apparatus, dealt with briefly here, will be described in detail in Chapter 2.

A CO_2 laser was used to produce and heat plasma columns confined by a solenoid magnet. The laser provided 2μsec pulses with energies up to 500 joules. Hydrogen gas was puff-filled into the core of the solenoid at fill pressures from 5-35 torr. The solenoid produced field strengths up to 70 kG.

Observations of the axial and radial dynamics were made. Axially the breakdown wave was found to be well described by a simple 1-D bleaching model (McKen et al., 1982). Density measurements near the laser focus indicated a finite ionization time of 20 nsec. This was found to be in good agreement with theoretical calculations. The rapid formation of a favorable, trapping profile was found to be a characteristic feature at the breakdown front. At late times (>1μsec), however, the density minimum on axis was generally weaker and occasionally absent. Only weak (<50%) or no compression was observed at these late times.

Occasional high density fluctuations were observed behind the front. These occurred only at early times in the column formation and were very short lived.

The radial behaviour was observed through both streak photographs and interferometrically determined, radial density profiles. It was found that the radial expansion of the plasma column agreed reasonably well with a model based on ion thermal conduction. There were, however, very dramatic effects observed in the radial expansion associated with the focussing ratio of the input laser. With the f/5 arrangement, the plasma was seen to expand initially at rates twice those observed with the f/15 arrangement. Similarly, with f/5 focussing the radial extent of the column was double that found with f/15 focussing.

Laser heating of the plasma was found to be very efficient. Approximately 85% of the incident laser energy was used in forming and heating the plasma column. From calculations based on energy balance, the plasma temperature was determined to be ~50 eV.

Comparatively high levels of stimulated scattering were observed (Fedosejevs et al.(1981), Offenberger et al.(1982a)). From an incident threshold intensity of 4x10^{10} W/cm^2, SRS signals were seen to grow rapidly and saturate at reflectivity levels of ~.7%. Temporally, the SRS signals appeared as a series of 5 nsec spikes which corresponded to high intensity spikes in the incident laser pulse. Spectrally, the SRS signals displayed a shot-to-shot variation in the wavelength shift from the incident radiation. This corresponded to density variations and the density values implied by the SRS wavelength shift agreed well with interferometric measurements.

High levels of SBS were also observed. Peak reflectivity values of 20-25% were seen. Temporally, the SBS signals were seen as very short (<3nsec) pulses corresponding to high intensity spikes in the input laser pulse. Indeed, the modulation of the laser pulse was found to be due to SBS signals feeding back into the laser cavity. Spectral measurements, when fitted with a kinetic wave model, yielded temperature values of ~40 eV. This agreed well with numerical calculations and other experimental measurements.

Detailed 2-D computer calculations were done to simulate the processes encountered in the laser-heated solenoid. The code combined the MHD calculations of SHELL as described by McMullin et al.(1979b) and the laser propagation calculations of HEATER as described by McMullin et al.(1982). Comparisons with the code were found, in most cases, to be very good.

CHAPTER II

Experimental Methods

2.1 Preliminary remarks

This chapter describes the apparatus, procedures followed and diagnostics used in producing and investigating the plasma in the laser-heated solenoid experiment.

There are two major components involved in the apparatus; the electron-beam (E-Beam) excited CO_2 laser and the linear magnetic solenoid.

In basic terms the procedure is as follows. The solenoid core is first puff-filled with hydrogen gas. Once the gas is stabilized, the laser is fired and the energy focussed at the input end of the solenoid. By this time the solenoid has been energized and provides an axial magnetic field which confines the laser-produced plasma column.

Numerous diagnostics were used and will be described in detail in later sections. The input laser beam energy and power, the puff-filled gas pressure, and the magnetic field strength were all monitored on a shot-to-shot basis. The luminous plasma boundaries (axial and radial) were followed by using a streak camera. Density and temperature characteristics of the plasma were obtained with ruby-laser interferometry and Thomson scattering. Highly sensitive gold and copper-doped germanium infra-red detectors were used to temporally resolve weak backscattered radiation. Infra-red and optical multichannel analysers were used to obtain signal spectra.

The experiment was run entirely from a control room which was screened from electromagnetic noise. The timing between various components of the experiment was controlled by a central, programmable, timing unit and several delay units. The timing was monitored with high-speed oscilloscopes.

2.2 The Apparatus

2.2.1 The E-Beam CO_2 Laser

The E-Beam CO_2 laser makes use of an electron beam to excite the lasing medium. The laser is capable of producing long, high-energy pulses which are necessary in the laser-heated solenoid experiment.

The electron beam was produced from a high field emission cathode which was energized by a 4-stage Marx capacitor bank. The Marx bank consisted of four 60 kV, 1.85 μF capacitors which required ~6 minutes to fully charge. A total of 13 kJ of energy were stored in this bank. Once switched, 240 kV were supplied and 15-20 kA of current were delivered to the electron gun. For insulation purposes, the capacitors were immersed in a high voltage oil bath.

The cathode consisted of an array of thin, stainless steel strips arranged edge-on on a ~120x15 cm plate. Because of the high voltage, a high vacuum ($<1\cdot10^{-5}$torr) had to be maintained in the gun chamber. This region of high vacuum was separated from the laser cavity (at 2 atmospheres pressure) by a thin titanium foil (.0015 inches thick) supported on a grid.

Having travelled across the high vacuum region, the electron beam passes through the foil and into the laser cavity. To provide a high interaction cross-section between the electrons and the laser gas mixture, a sustainer voltage is applied to a large graphite anode within the cavity.

The sustainer capacitor bank consisted of six 60 kV, 1.85 μF capacitors. These were arranged into three sets. Each set consisted of two capacitors in series. The three sets were connected in parallel. Charged to 90 kV, this capacitor bank stored 11.2 kJ of energy. These capacitors were also submerged in high voltage oil. The charging time for the sustainer bank was ~4 minutes.

2.2.2 The Laser Cavity

The laser cavity, with an active volume of ~20 litres, was filled with a gas mixture of helium, nitrogen and carbon dioxide at a ratio of $He:N_2:CO_2=3:2:1$ to a pressure of 2 atmospheres.

This gas mixture provided a long laser pulse (1-2 μsec) of high energy (250-500 joules) characterized by a short gain-switched pulse (~50 nsec wide) and a long tail. An oscilloscope trace showing the laser signal is given in Figure 2.1.

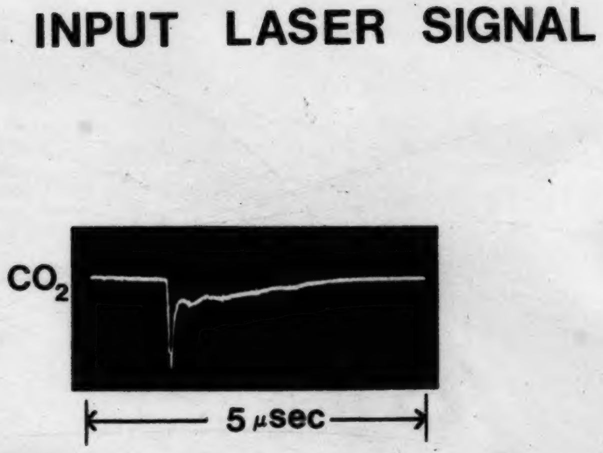

Figure 2.1 CO_2 Laser Pulse Shape

The spike-to-tail power ratio and the overall pulse length and energy can be varied by adjusting the gas ratio. Only very slight changes to the 3:2:1 ratio were ever used.

Both stable and unstable resonator optics were used in the cavity. Because of the reduced divergence (<400μrad) and higher output energy (~500 joules) the unstable optics were used nearly exclusively. Re-alignment of the cavity optics was required after every shot.

The laser output was through an optically flat, highly polished, 6"x6"x1.5", NaCl (salt) window. Salt is used because of its low absorption at infra-red wavelengths.

2.2.3 The Solenoid Apparatus

The laser pulse was directed into the solenoid apparatus, as shown in Figure 2.2. This apparatus consists of the solenoid itself and a steering-focussing arrangement for the incoming pulse.

Two distinct focussing arrangements were used. In one case, an off-axis parabolic mirror was used to both turn and focus the laser light. The parabola had a focal length of 50 cm giving an f/5 focus.

The other focussing method is that shown in Figure 2.2. Here, a 90° turning mirror steers the beam to a spherical mirror. This mirror directs the beam back through a hole in the turning mirror and provides on-axis focussing. Since the unstable laser cavity produces an annular beam, very little laser energy is lost due to this Cassegrain arrangement. The

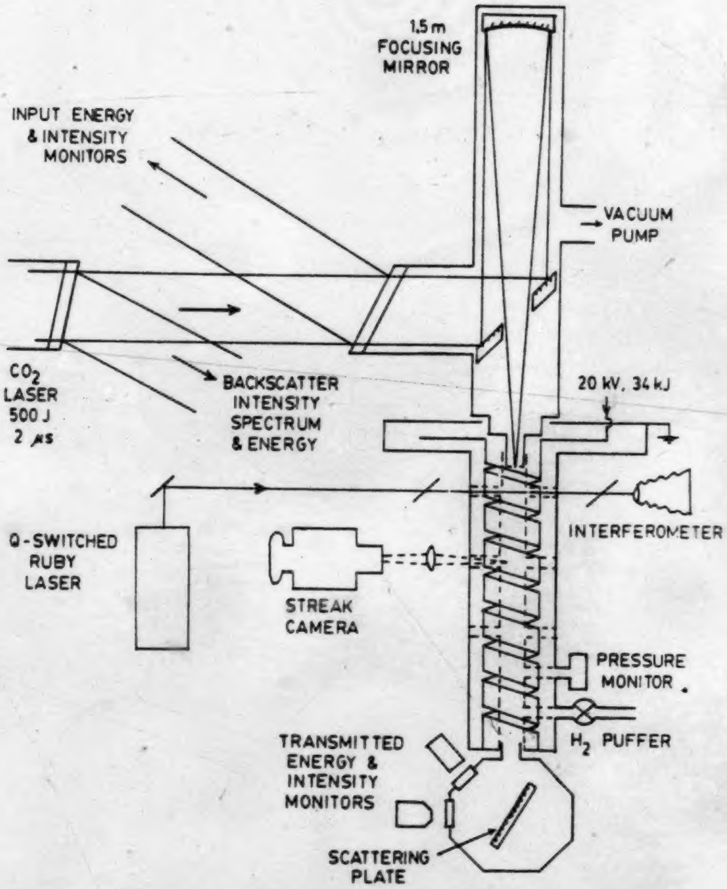
1.5 m
FOCUSING
MIRROR
INPUT ENERGY
& INTENSITY
MONITORS
VACUUM
PUMP
CO_2
LASER
500 J
2 μs
BACKSCATTER
INTENSITY
SPECTRUM
& ENERGY
20 kV, 34 kJ
Q-SWITCHED
RUBY
LASER
INTERFEROMETER
STREAK
CAMERA
PRESSURE
MONITOR
H_2 PUFFER
TRANSMITTED
ENERGY &
INTENSITY
MONITORS
SCATTERING
PLATE

Figure 2.2 Laser-Heated Solenoid: Basic Experimental Arrangement

focal length was 1.5 meters giving an f/15 focus.

The different focussing arrangements produced different focal spot and focal depth characteristics. With the f/5 optics, the focal spot was ~385 μm in diameter and the focal depth (where the laser intensity drops to 1/2 of its maximum) was ~1 cm. With the f/15 optics, the focal spot was ~300 μm and the focal depth was ~2.5 cm.

If the laser energy was focussed in even a low density gas, a detonation wave, travelling back toward the laser, would result. The plasma produced by such a detonation wave would absorb the laser energy before it had penetrated into the solenoid region. For this reason, the laser-focussing region was evacuated to pressures ≤100 millitorr.

Initially the entire solenoid apparatus is evacuated. Hydrogen gas is then puffed into a plexiglas inner tube inside the solenoid core. The gas is prevented from flowing into the focussing region by a small aperture (~4.2mm diameter), just large enough to allow penetration by the laser light. A profile of the pressure along the axis of the solenoid is shown in Figure 2.3. The pressure ratio at the gas-vacuum interface is seen to be better than 20:1. The uniformity of the pressure (after ~2 msec) along the solenoid axis is also apparent.

The hydrogen gas was puffed in using an electromagnetic valve which could be opened for variable lengths of time. This allowed for easy variation of the filling density without changing the relative timing of the system.

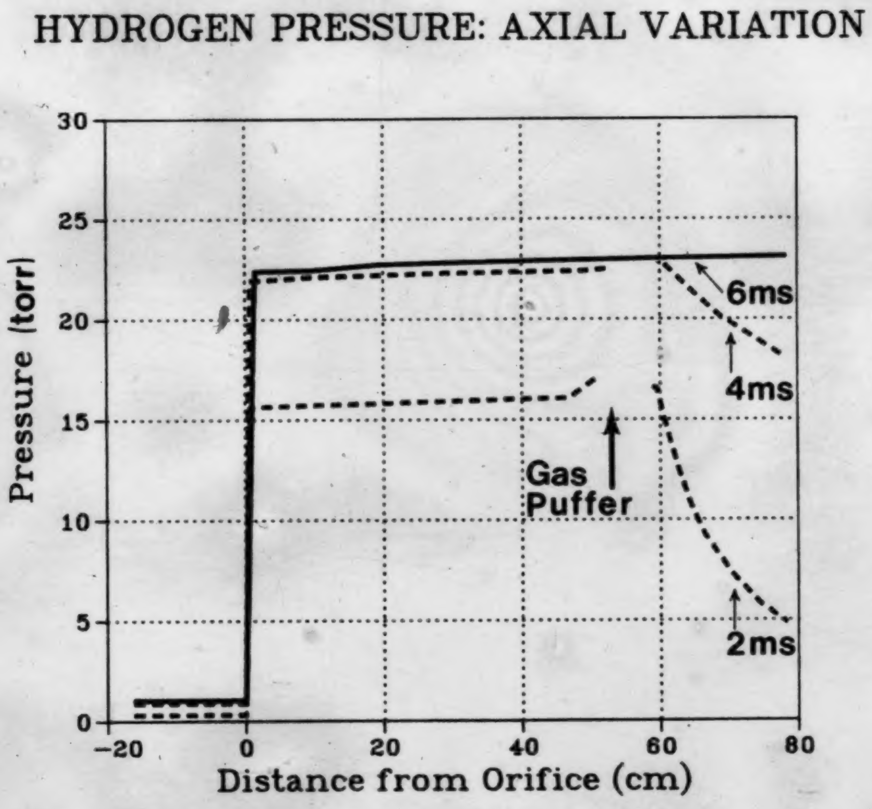

HYDROGEN PRESSURE: AXIAL VARIATION

Figure 2.3 Axial Variation of the Hydrogen Fill Pressure

2.2.4 The Solenoid

The solenoid provides an axial magnetic field which permeates the plasma and restricts radial expansion.

Two solenoid designs were used during the course of this study; the split-coil and the single-coil solenoid.

The split-coil solenoid consisted of two 20 cm coils separated by a 5 cm region designed to give access for observation and diagnostics. The reduction in magnetic field strength in this region was ~40% and resulted in significant radial losses. In order to produce long plasma columns which extended into the second half of the solenoid, a flux-coupling metal sleeve was inserted in this diagnostic region. This resulted in a field reduction factor of ~10%.

Much useful data was obtained with the split-coil but the coupling sleeve made the central diagnostic region superfluous. For this reason a single-coil solenoid was designed and implemented. The majority of the results were obtained with the single-coil solenoid.

The single-coil was a 7-turn helix machined from a solid bronze rod. It had an internal bore of 4 cm and provided a maximum central field strength of ~70 kG. The axial variation of the field is shown in Figure 2.4.

The magnet was energized from a bank of twelve 20 kV, 14 μF capacitors connected in parallel. A total energy of 36 kJ was stored in this capacitor bank. The charging time for the bank was ~3 minutes. In order that the magnetic field be uniform, all capacitors must fire simultaneously.

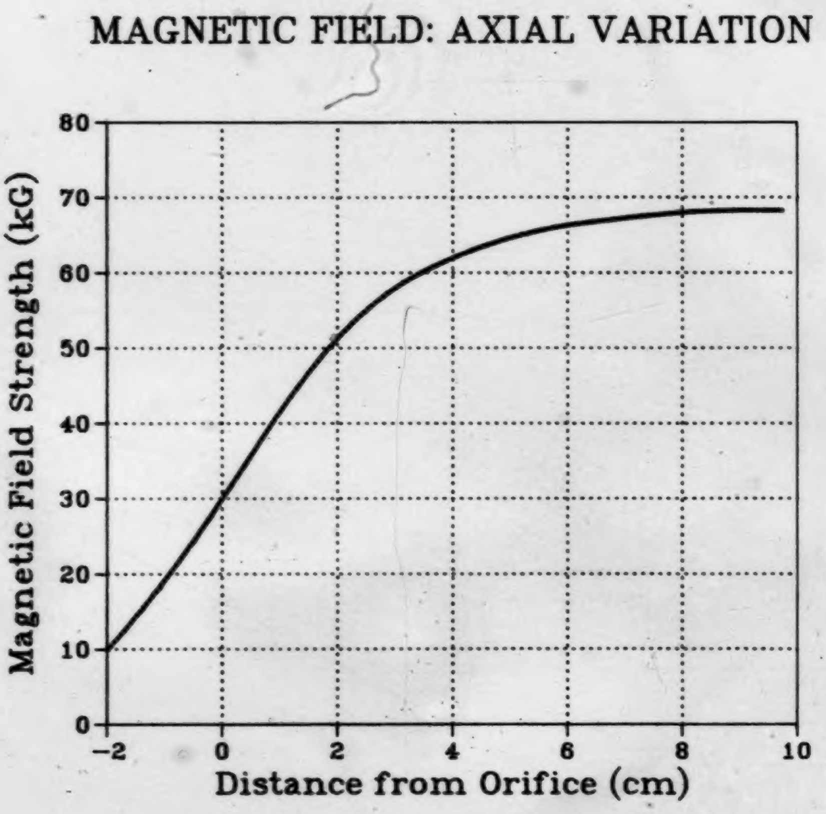

Figure 2.4 Axial Variation of the Magnetic Field Strength

These capacitors were switched by individual spark gaps triggered by a main gap.

The circuit inductance was .12 μhenrys resulting in a quarter-period time of 7 μsec for the current and the magnetic field. When the experiment is set-up so that breakdown occurs when the magnetic field reaches its maximum value, the field decreases by less than 3% during the first microsecond following breakdown. The magnetic field, then, is approximately constant during the development of the plasma column. An oscilloscope trace showing the temporal variation of the magnetic field, detected by a pick-up coil, is given in Figure 2.5. The input, CO_2 laser signal is also shown, superimposed.

The low circuit inductance was obtained by using a co-axial return current. This was carried by an outer aluminum casing with a diameter of ~10 cm. To prevent arcing the region between the solenoid and the outer casing was filled with either SF_6 or Freon-12 at low pressure (1-5 psig).

A plexiglas tube with inner diameter ~2.5 cm and outer diameter ~3.5 cm was inserted into the bore of the solenoid. It was into this inner tube that the hydrogen gas was puffed. The tube sat firmly in the solenoid, supported by O-rings at each end to absorb shock.

The plasma was observed through windows placed along the outer casing at regular intervals. In some cases the windows were aligned with the spacing between turns in the

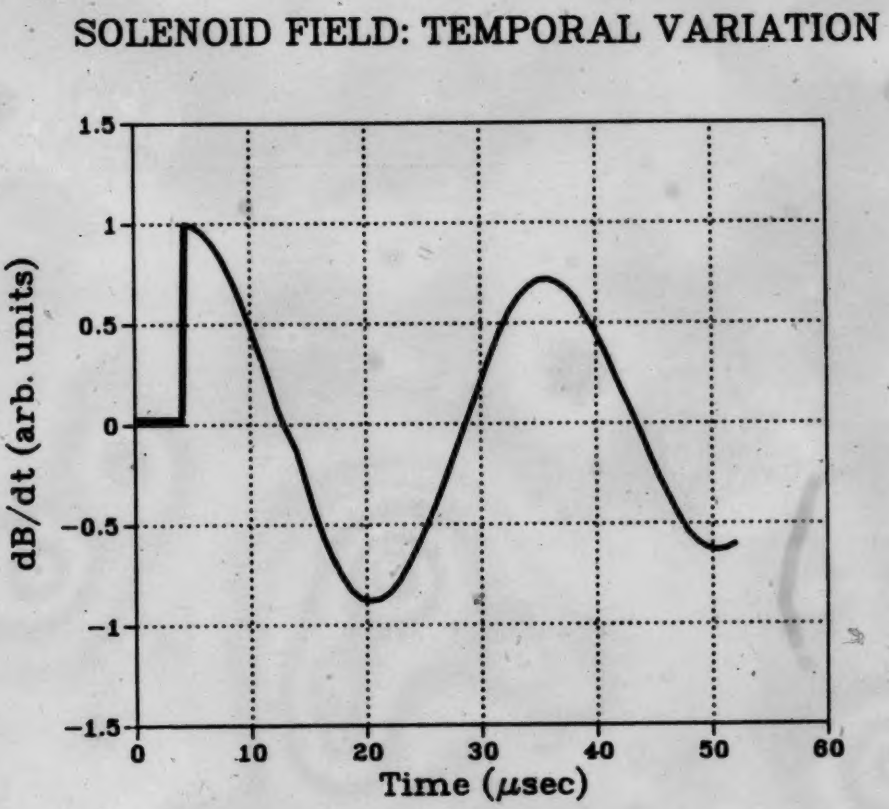

Figure 2.5 Magnetic Field: Temporal Variations

solenoid while in others, access ports were machined through the coil. The space between the turns in the solenoid was ~1 cm across. The ports machined in the coil were initially 1 cm in diameter but were later increased to 1.6 cm for better access.

In cases where direct access to the plasma was required, as in interferometry or Thomson scattering, matching ports were machined into the inner plexiglas tube. To maintain vacuum and to prevent leakage of the insulating gas into the plasma region, a system of O-rings, nylon sleeves and glass or plexiglas windows was used in these ports.

As shown in Figure 2.2, the output end of the solenoid was connected to a small chamber containing a scattering plate. Laser energy which passed through the solenoid into the end chamber was scattered by the plate. The energy and power were monitored by detectors mounted outside the chamber. Energy measurements were calibrated by using a NaCl beam splitter to deflect 8% of the laser energy incident on the plate onto a calibrated calorimeter. By comparing the energy detected off the plate to the incident energy, a calibration factor was determined.

2.3 Diagnostic Techniques

2.3.1 Streak Photography

The luminous boundary of the plasma was followed photographically using a TRW high-speed streak camera.

The streak camera images the plasma light onto a slit placed before a photocathode. The signal is amplified and imaged electronically to a phosphorescent screen. The slit is then re-imaged onto the base of the recording film. When activated the image is swept upwards at a controlled rate. Each position along the film then corresponds to progressively later times.

To follow the axial development, the camera is oriented so that the slit is aligned with the central axis of the solenoid. Plasma light can only be detected when emitted from an observation window. On the axial streak photograph, this results in a series of parallel lines each representing the time history of the plasma light from a single location along the axis. Figure 2.6-a shows an example of an axial streak.

To follow the radial development of the plasma, the camera is rotated 90° so that the slit is perpendicular to the solenoid axis. The light detected is emitted from a single axial location. The radial streak photograph gives directly the rate of radial expansion of the plasma column at this axial location. Figure 2.6-b shows an example of a radial streak.

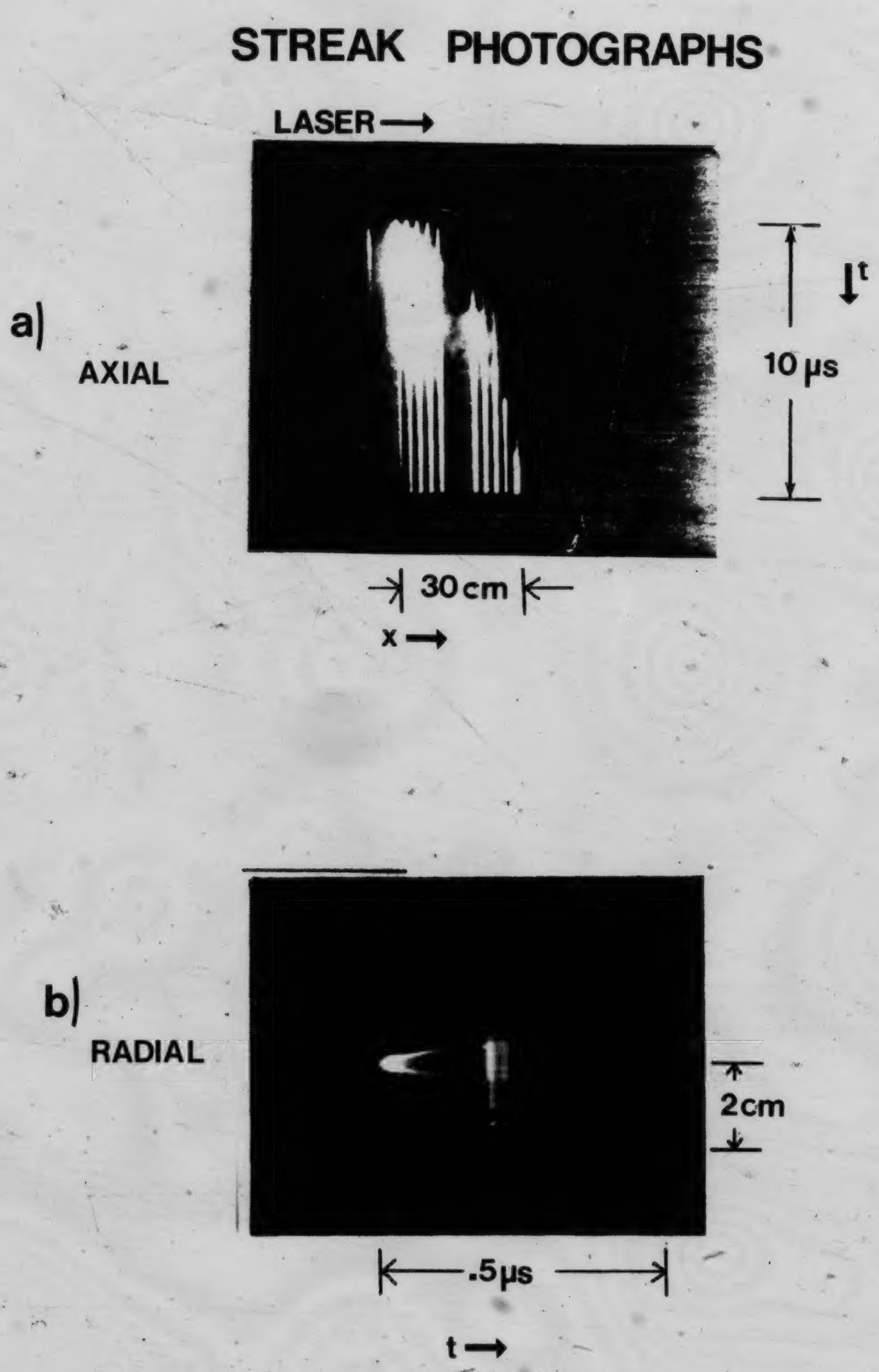
STREAK PHOTOGRAPHS
LASER →
a)
AXIAL
t
10 μs
30 cm
x →
b)
RADIAL
2 cm
.5 μs
t →

Figure 2.6 Streak Photographs:
a) Axial (f/5 focus) and b) Radial (f/15 focus)

Sweep times from 2 to 10 μsec were used for axial streaks. For radial streaks, sweep times from 100 to 500 nsec were used. The calibration of the streak photograph is dealt with in Chapter 4.

To prevent mis-firing of the camera because of electrical and magnetic interference, the camera was kept several meters from the experimental area. In the case of radial streaks, the plasma light from the selected axial window was re-imaged in front of the camera with a large aperture lens.

Although the variation of the plasma luminosity in time is also detected by the streak photograph, its relation to other plasma parameters (density, temperature, ionization state) is complex and difficult to interpret.

2.3.2 Interferometry

A Mach-Zehnder interferometer was used to obtain electron density information.

The index of refraction for a plasma depends directly on the electron density. A change in the plasma density causes a change in the index of refraction which in turn causes a phase shift in the light passing through. This results in a shift in the interference pattern which, under certain geometric constraints, can be inverted to provide the electron density profile. Details of the inversion techniques are given in Chapter 4.

The Mach-Zehnder is particularly useful in this application since it can easily be constructed around the solenoid apparatus, is readily aligned and allows for straight-forward imaging of the plasma.

The mirrors and splitters used in the interferometer were 10 cm diameter quartz flats. These were bolted onto a heavy aluminum plate. This support plate was securely bolted to the solenoid table at the desired axial location.

A ruby laser provided a 35 nsec, 200 millijoule pulse for the light source. The relatively short pulse effectively freezes the hydrodynamic motion at an instant in time. The laser output pulse was telescoped to a ~2 cm diameter to give a very uniform, low divergence beam.

The degree of the fringe shift, in units of fringes, depends on the plasma density, the plasma diameter, and the wavelength of the light source, so that, N, the fringe shift, is given by,

$$N = (\lambda e^2/2\pi mc^2)\cdot\int\{n\cdot dl\}$$

and, for uniform density,

$$= (n\cdot e^2\cdot\lambda L)/(2\pi\cdot m\cdot c^2) \qquad (2.1)$$

where,

n=the electron density
e=the electron charge
λ=the wavelength of the light source
m=the electron mass
L=the plasma diameter

With a ruby light source (λ=6943 A), a 1 cm plasma and with densities in the range $5 \cdot 10^{16}$ - $1 \cdot 10^{18} cm^{-3}$ then the corresponding fringe shifts will be in the range .2 - 3 fringes. This degree of fringe shifting is suitable for analysis indicating that the ruby laser is an appropriate light source for the plasma conditions expected in this experiment.

A helium-neon (He-Ne) alignment laser was directed along the axis of the ruby laser. By fixing the path of the He-Ne laser to match exactly the path of the ruby laser, the interferometer was accurately aligned.

The beam was directed into the plasma through windows made simply of plate glass. These windows proved adequately flat, however, they were fragile and fractured easily. Cleanliness on these surfaces or on any of the interferometer pieces was essential.

By adjusting the orientation of the interferometer optics, various interference patterns can be obtained. The interferometer was set up to provide 20-30 straight line fringes/cm aligned perpendicularly to the solenoid axis.

A transparent resolution card was placed in the solenoid core at the observation position. Careful imaging of this card on the film plane ensured that the plasma was properly focussed. This also provided the necessary spatial calibration factor.

On a particular shot, a density profile can be taken only at a single axial location at a particular moment in time. To determine the time dependence of the density required a number of shots. To determine any large scale variations of the density with axial position, the entire apparatus was shifted to a new axial location.

Axial variations over the dimension of the solenoid window could be observed with a single shot. Actually, the axial variations over this distance (1.0-1.9 cm) can be considered small and the variations interpreted as being due to temporal changes.

Further discussion concerning the interpretation of the interferograms will be given in Chapter 4.

2.3.3 Thomson Scattering

Thomson scattering has proven to be an extremely useful plasma diagnostic. In this procedure, incident electromagnetic radiation is scattered primarily off of the free electrons in the plasma. Figure 2.7 shows the geometric relation between the incident and the scattered radiation. The angle θ is the scattering angle between the incident wave vector ($\underline{k}_0$) and the scattered wave vector ($\underline{k}_s$). The differential wave vector, $\underline{k}$ is also indicated in Figure 2.7.

In most plasmas the Debye length, $\lambda_d(=\sqrt{\{kT_e/8\pi ne^2\}})$ is the smallest distance over which the electrons are correlated. A scattering parameter, α_s, compares the Debye length and the scattering scale (phase) length ($1/|\underline{k}|$). The size of this parameter describes the primary scattering process and indicates what information can be extracted from

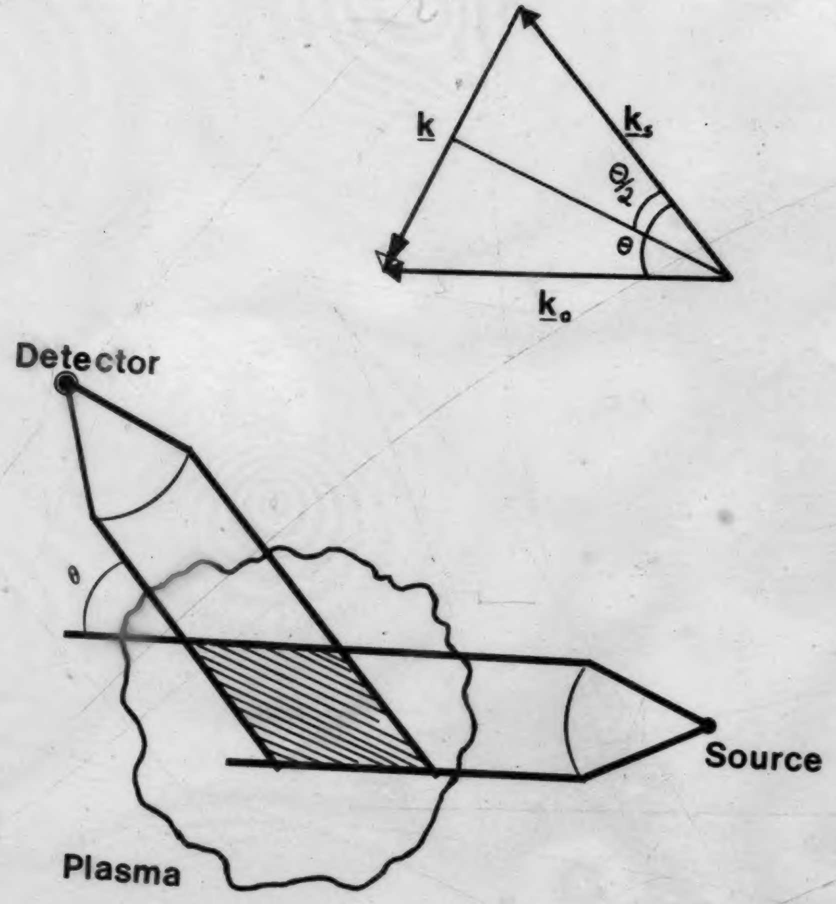
k
k_s
θ/2
θ
k_o
Detector
θ
Source
Plasma

Figure 2.7 Relation between Incident and Scattered Radiation in Thomson Scattering

the scattered spectra.

When $\alpha_s<<1$ the scattering is incoherent and the scattered spectra is Gaussian. The width of the distribution gives a measure of the electron temperature. When $\alpha_s>>1$ the scattering is collective. The scattered spectra consists of a central ion feature and two detached satellites. The position of the satellites depends on the electron density and the width of the central feature depends on both the ion and electron temperatures.

In this experiment the scattering angle was fixed at 90°. The incident radiation is ruby light (λ_0=6943A) and so, with,

$$\alpha_s = 1/(k\cdot\lambda_d) = \lambda_0/\{4\pi\cdot\lambda_d\cdot\sin(\theta/2)\}$$

then,

$$\alpha_s \simeq 10^{-8}\sqrt{\{N/T\}}$$

where, $|N|=|cm^{-3}|$ and $|T|=|ev|$

For typical plasma parameters, ($N\simeq10^{17}$, $T\simeq50ev$), the scattering parameter is approximately unity ($\alpha_s\simeq1$).

In this α_s domain the spectrum departs from a Gaussian, developing shoulders on each side. By fitting the data, both the electron temperature and density can be obtained.

Further details concerning the theory of Thomson scattering and the analysis of the spectral data are given in Chapter 4. The experimental set-up used for Thomson scattering is shown schematically in Figure 2.8.

To obtain a large scattered signal, a large incident signal is required. However, it is essential that the

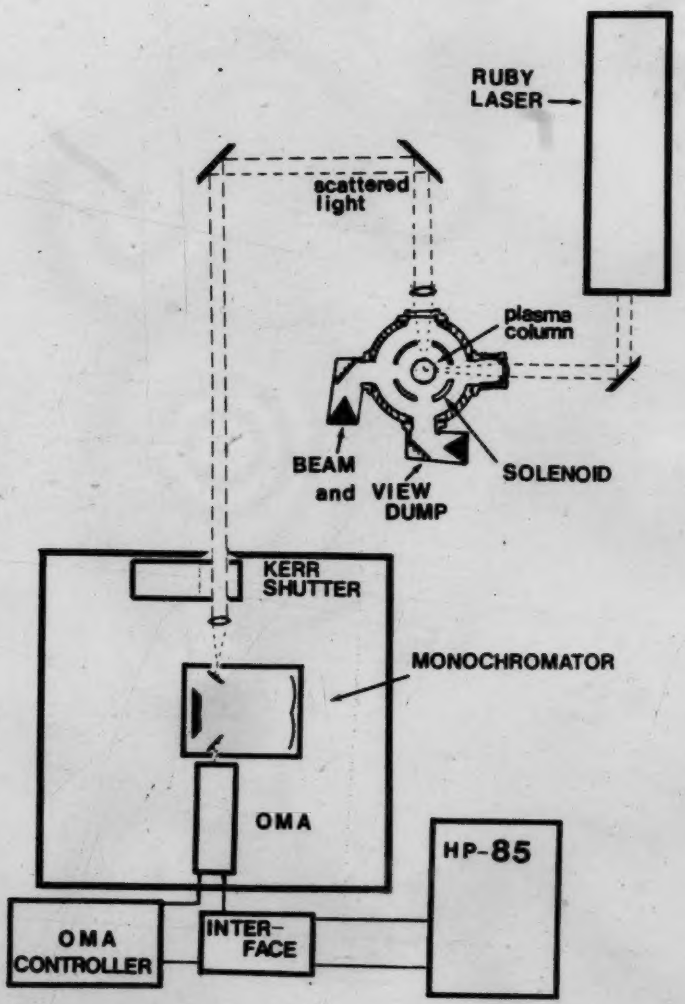
RUBY LASER
scattered light
plasma column
BEAM and VIEW DUMP
SOLENOID
KERR SHUTTER
MONOCHROMATOR
OMA
HP-85
OMA CONTROLLER
INTER-FACE

Figure 2.8 Experimental Arrangement for Thomson Scattering

probing radiation does not influence the plasma conditions. Calculations show that with ruby laser energy below ~10 joules, the amount of energy absorbed by the plasma is not significant enough to perturb the plasma temperature and density.

The same ruby laser used for interferometry was also used here except that an amplifying stage was added. This provided a 1-2 joule, ~40 nsec laser pulse.

To further enhance the scattered signal, the incident light was polarized horizontally. As with the radiation pattern of a dipole antenna, horizontal polarization maximizes the signal.

The laser pulse was telescoped to a diameter of ~2.5 cm to reduce the energy density and to prevent damage to the steering mirrors. Nevertheless, high quality, gold-coated mirrors were required to direct the beam.

The input optics consisted of a 2 cm lens with a 10 cm focal length on an adjustable mount. This lens also provided the vacuum seal and was the only optical surface in the input system thereby reducing stray light. The adjustable mount allowed small changes to be made in the axial and radial location of the focal volume in the plasma.

A glass micro-balloon (~200μm diameter) was positioned in the solenoid core at the desired location for the scattering volume. A He-Ne alignment laser, whose path matched that of the ruby laser, was then focussed onto the balloon. The He-Ne light scattered from the balloon was used to align the collection optics and the detection system. Because of slight changes in the orientation of the input lens when the system was pumped out, the alignment was made with the system under vacuum.

The scattered light passes out of the plasma through a glass window, through an aperture and into the collection lens. This lens matched the input lens with a diameter of 2 cm and a focal length of 10 cm. The collection lens was set-up to provide a parallel output beam which was directed into the detection system.

Before describing the detection system, methods used to prevent stray light will be discussed.

A large amount of stray light was generated by the ruby light scattering off of the surfaces in and around the ruby laser cavity, from surfaces inside and outside the solenoid structure, and from optical surfaces in the Thomson scattering set-up. By placing the detection system in a light-tight container and by incorporating black cloth screens around the laser and the solenoid, only light that was scattered directly into the collection path was detected.

To reduce the light scattered from internal solenoid surfaces, a beam dump and a viewing dump were included in the system. These were identical units made up of two pieces of blue-green filter glass (OB-10 glass) which effectively absorbs ruby light.

The first piece of glass was set approximately at Brewsters angle to the light cone coming from the focal volume. The second surface was set at Brewsters angle to light reflected from the first. The surfaces required careful cleaning since they readily became coated with blow-off from the plasma. When dirty, the first surface in the beam dump was easily damaged due to enhanced absorption of the ruby laser energy.

The glass was also fragile and fractured on occasion when the solenoid was activated. Securing the pieces with a shock absorbing rubber compound proved to be an effective cure for this problem.

The detection system consisted of a 1/4 meter monochromater and an optical multichannel analyser (OMA). This apparatus was set inside a large box several meters from the experimental area. The box had a single input hole.

Bremsstrahlung radiation and, in particular, the Hydrogen-α (6600 A) emission interfered with signal detection. A Kerr shutter was required in order to reduce the amount of plasma radiation entering the monochromator.

The Kerr shutter was set up so that only light polarized in the direction of the scattered signal would pass through. The shutter was activated by a high voltage gate pulse which kept it open for ~20 nsec. This effectively eliminated the bremsstrahlung radiation and brought the H-α radiation to acceptable levels.

Precise timing of the Kerr shutter was achieved by scattering suitably attenuated ruby light off a microballoon placed in the solenoid core. The timing of the Kerr shutter was adjusted until the signal detected (with a photomultiplier) behind it was maximized. Reliable and consistent switching was essential.

The scattered light was focussed onto the 150μm input slit of the monochromator. An f/5 focussing system was used to provide 1:1 imaging of the scattering volume. The monochromator provided 132 A/mm dispersion. The output of the monochromator went directly onto the face of the OMA vidicon.

The detector target of the OMA consists of several million photodiodes on a 16 mm diameter silicon disk. The detector has a sensitivity of ~10 photons/count and a range of ~16,000 counts/channel.

An electron beam scans a 12.5 mm x 12.5 mm region of the target, providing a 512 x 512 array of picture elements each ~25μm in diameter. A channel is a vertical line of picture elements and a track is a horizontal line of channels. The scan is programmable and may consist of many parallel tracks giving a two dimensional output. The scan time is adjustable from 20-140 μsec/channel.

In the multi-track mode, 5 tracks separated by 20 picture elements were typically used. Each track was 100 channels across and each channel was 20 elements high. The dispersion of the monochromator provided a horizontal scale factor of 3.17 A/channel.

The OMA control and the data acquisition were performed through an HP-85 micro-computer. The number and vertical separation of the tracks, the height of the channel and the scan time were all preset and down-loaded from the HP-85 to the OMA controller.

A trigger pulse started the OMA scan. With the start of the sweep, the OMA controller provided a synchronous pulse which was used to fire the rest of the experiment. The firing sequence was the same as previously described. With a scan rate of 100 μsec/channel, approximately 20 channels would be scanned prior to the onset of the CO_2 laser and the subsequent arrival of the scattered ruby light.

Following the shot, the data was transferred to the HP-85 and stored in memory. The scan was then repeated to provide background counts which were then subtracted from the data thereby producing the scattered spectrum. This data and the associated control parameters were then stored on magnetic tape.

To determine the level of stray ruby light, the ruby laser was fired alone, with the solenoid evacuated. To determine the level of plasma light, the experiment was run without firing the ruby laser.

2.3.4 Stimulated Scattering

The CO_2 radiation, incident on the plasma column, can interact with and, indeed, enhance plasma waves resulting in scattered electromagnetic radiation.

The spectra of the scattered radiation depends on the character of the plasma wave. The nature of the plasma wave, in turn, depends on the condition of the plasma. The analysis of the scattered spectra can thereby provide an effective plasma diagnostic.

A detailed description of the scattering processes is given in Chapter 3.

The backscattered radiation returns along the path of the input CO_2 laser. The output window of the laser cavity was set at a slight angle (~5°), acting as a beam splitter for the backscattered radiation. Approximately 8% of the scattered light was reflected from this window and directed into the detection area. In the detection area the backscattered signal was split and then temporally and spectrally resolved. The set-up is shown in Figure 2.2.

2.3.5 Detection of the SBS Signal

The SBS signal was temporally resolved with a liquid nitrogen cooled, gold-doped, germanium detector. This device has a risetime of ~1 nsec and a sensitivity (at 10.6 μm) of ~10^{-3} volts/watt into 50 ohms.

The spectrum was obtained by dispersing the signal with an infra-red monochromator which provided a dispersion of 3.2 A/channel. An infra-red multichannel analyzer (IRMA) was used to detect the signal from the monochromator.

The IRMA is a pyro-electric detector. The target area is 10mm x 10mm with an effective channel width of ~33 μm. The temperature of the target material increases when incident radiation is absorbed. This alters the internal electric polarization thereby releasing surface charge which is detected by a scanning electron beam. The scan is entirely one dimensional.

The stray light level was determined by firing into very low density plasma from which there is no scattered radiation. Stray light levels were not appreciable.

The calibration procedure involved the placement of a NaCl back reflector into the incident CO_2 path. This placed a known signal into the detection system, allowing the absolute levels of backscattered radiation to be determined.

2.3.6 Detection of the SRS Signal

The SRS signal was temporally resolved with a liquid helium cooled, copper-doped germanium detector. The device has a risetime of ~1 nsec and a sensitivity (at 10.6 μm) of ~20 volts/watt into 50 ohms. The increased sensitivity was required because of the weaker nature of the SRS signal.

The signal spectrum was obtained by dispersing it with a salt (NaCl) prism. This provided a dispersion of 66.3 A/channel. The dispersed signal was detected with the IRMA.

Stray light levels were determined in the same way as with the SBS signal. In this case, large SBS signals were back reflected along with the SRS signals. To reduce the SBS, an SF_6 absorption cell was placed in the detection path. SF_6 strongly absorbs radiation near 10.6μm but readily transmits the longer wavelength (~14μm) SRS radiation.

CHAPTER III

Theory

3.1 Preliminary remarks

Background theory covering several aspects of laser-plasma interaction in the laser-heated solenoid is presented in this chapter. Calculations are based on typical experimental conditions.

Following Raizer(1977), the processes involved in laser-induced gas breakdown are discussed. A calculation of the time required to achieve full ionization is given. The absorption of laser energy by inverse bremsstrahlung is described and a calculation of electron-ion temperature ratio is given.

A detailed description of the one-dimensional axial propagation of bleaching waves is presented. The emphasis is on the models of Rehm(1970) and of Burnett and Offenberger(1976). Pre-ionization is an important consideration in these models and the conclusions of Scudder(1979) in this regard are discussed. The optical detonation model of Ahlborn et al.(1982) is outlined and discussed.

A simple model for the radial expansion of the plasma, based on ion diffusion and inverse bremsstrahlung heating, is given. Expansion rates are then calculated. Maximum radii are estimated using the model of the plasma column developed by Ahlborn et al.(1982).

Two-dimensional (2-D) effects are considered. The 2-D magnetohydrodynamic code called SHELL (McMullin et al.,1979) and the laser heating package called HEATER (McMullin et al.,1981) are described and test results are given.

Finally, stimulated scattering is considered. Stimulated Brillouin and Raman processes are described. Threshold conditions, growth rates and saturation mechanisms are discussed.

3.2 Laser-Induced Gas Breakdown

Following the development of the laser, experiments (Meyerand and Haught(1963), Ramsden and Davies(1964), and others) indicated that by focussing ruby laser light, sufficiently high intensities could be achieved so as to cause breakdown in gases.

For sufficiently high laser intensity, ionization may occur through the multiphoton photo-electric effect. In this process, n photons are simultaneously absorbed. For ionization, the total photon energy, $n \cdot h\nu$, must exceed the ionization energy. The ionization energy for the hydrogen atom is 13.6 eV, while the photon energy for CO_2 laser light is .117 eV. Thus, 117 CO_2 photons must be simultaneously absorbed to ionize the hydrogen atom. The probability for such an occurrence is given by (Raizer, 1977, section 3.1),

$$P = \omega \cdot n^{3/2} \cdot \{(2.727 \cdot e^2 \cdot E_0^2)/(8 \cdot m \cdot \omega^2 \cdot I)\}^n \text{ sec}^{-1} \qquad (3.1)$$

where,

?

e = the electron charge = $1.6022 \cdot 10^{-19}$C
m = the electron mass = $9.1095 \cdot 10^{-31}$kg
$\omega = 1.78 \cdot 10^{14}$ sec^{-1} (CO_2 radiation)
I = 13.7 eV = $2.18 \cdot 10^{-18}$joules (Hydrogen)
E_0= the electric field amplitude

With $|E_0| = |\text{volts/cm}|$, equation (3.1) becomes,

$$P = 1.78 \cdot 10^{14} \cdot n^{3/2} \cdot \{1.39 \cdot 10^{-15} \cdot E_0^2\}^n \text{ sec}^{-1}$$

With the number of photons required to be absorbed, $n = 117$, and taking as a typical experimental value $E_0 = 1 \cdot 10^7$ volts/cm, the probability for a multiphoton ionization event is $P = 1.2 \cdot 10^{-83}$sec^{-1}. This indicates that the process is rather improbable and a much more likely ionization mechanism is that of electron-avalanche.

In electron-avalanche or cascade ionization, some free electrons are required to be initially present in the gas. In collision with neutral atoms, these seed electrons can absorb photons and are, thereby, accelerated. Once an electron has been accelerated to the ionization potential, collisional ionization can occur and another free electron be produced. Both the original and the newly freed electron are now accelerated and the avalanche begins.

If the initial number of seed electrons is N_0 and the time required for the electron density to double is τ_d, then the electron density, N, at some time, t, is,

$$N = N_0 \cdot 2^{t/\tau_d} \tag{3.2}$$

Taking an initial seed density $N_0 = 1$ cm^{-3}, and a final electron density (for neutral dominated conditions), $N=1\cdot10^{13}\mathrm{cm}^{-3}$, then, the ionization time, τ_i is,

$$\begin{aligned}\tau_i &= \tau_d\cdot\log_2(N/N_0)\\ &\simeq 43.2\cdot\tau_d\end{aligned} \tag{3.3}$$

The doubling time, τ_d, is basically the time required for an electron to reach the ionization energy. From a classical point of view, the electron gains energy by oscillating in the electric field, $\underline{E}$, of the laser light. Collisions with neutrals randomizes this motion thereby increasing the electron temperature. Considering only elastic collisions, the rate of increase of electron energy, ϵ, is given by,

$$d\epsilon/dt = [\{M\cdot e^2\cdot E^2/m\cdot(\omega^2+\nu_m^2)\} - 2\cdot(m/M)\cdot\epsilon]\cdot\nu_m \tag{3.4}$$

where ν_m is the collision frequency, ω is the laser frequency, and M is the mass of the ion.

There are two important details to consider before estimating the electron doubling time. These are the loss of electrons through diffusion and the loss of electron energy through inelastic collisions.

The diffusion time, τ_t, is given by,

$$\tau_t = L^2/D \tag{3.5}$$

where L is a characteristic length and D is the diffusion coefficient. The diffusion coefficient depends on the electron energy ϵ, the collision probability P, and the pressure p (in torr) such that for neutral dominated conditions,

$$D = 2\cdot 10^{7}\{\epsilon/(P\cdot p)\}^{(1/2)} \qquad (3.6)$$

Averaging collision probabilities (Brown, 1966) over electron energies from 0 to 14 eV, then in 20 torr hydrogen, $D \simeq 10^{5}$ cm^{2}/sec.

Taking the focal spot diameter as the characteristic length, then $L \simeq .04$ cm and the diffusion time is estimated to be $\tau_t \simeq 20$ nsec. If this diffusion time is much longer than the electron doubling time, then diffusion need not be considered.

The question of electron energy losses due to inelastic collisions is a complex one since, unlike elastic losses, inelastic losses do not occur with each collision. When an inelastic collision does occur the atom is left in an excited state. From this state it may be instantaneously ionized through a multiphoton process or return to the ground state through photon emission. In the first case the excitation energy is not lost and the avalanche continues unabated. In the second case the energy is totally lost and the avalanche is inhibited.

Raizer(1977, section 16) examines solutions to the transport equation for both of these cases but not for the intermediate case where only some fraction of the electron energy is lost to excitation. The equation solved is an approximation to the transport equation. It involves an expansion parameter which, in the high frequency case (laser frequency>>collision frequency), is the quantity u/v ($=eE_0/m\omega v$). The condition for the validity of the approximation is, then, $u \ll v$.

For electron temperatures of ~20 eV the thermal velocity is $\sim 3\cdot 10^8$ cm/sec. In order that the solutions be valid, the effective limit on the electric field becomes $E_0 \ll 3\cdot 10^7$ volts/cm.

Assumptions are made in order to simplify the problem. For instance, only monatomic gases are considered, elastic losses of electron energy are ignored, the elastic collision frequency is assumed to be independent of the electron energy and inelastic collisions involving electrons with energies greater than the ionization energy are considered to occur instantaneously.

In the first case, without excitation losses, Raizer shows that apart from a factor close to unity, the electron doubling time is simply the time required to reach the excitation energy.

Elastic losses in equation (3.4) can be ignored since the maximum energy achievable, limited by these losses, is,

$$\epsilon_{mx}=M\cdot e^2E^2/\{2m^2(\omega^2+\nu_m^2)\} \qquad (3.7)$$

For values typical of this experiment, $\epsilon_{mx}=2$ keV. Clearly, these losses will not prevent the electrons from reaching the ionization energy of ~14 eV. Equation 3.4 can then be simplified to,

$$d\epsilon/dt = e^2E^2\nu_m/(m\omega^2)$$

and integrating,

$$\tau_d=I\cdot m\omega^2/e^2E^2\nu_m \qquad (3.8)$$

Again, averaging over the electron energy range $0<\epsilon<14$ev, the collision frequency (Brown, 1966) is estimated to be 10^{11} sec^{-1}. Using a typical electric field value, $E=10^7$ volts/cm, the doubling time is 25 psec. With $\tau_d<<\tau_t$, the neglect of diffusion effects is justified. From equation (3.3), the ionization time is estimated to be ~1.2 nsec.

In the second case which Raizer considers, the excitation energy is completely lost. The ionization frequency is determined from the expression,

$$\exp\{(a-1)y\}\cdot[\cosh(y/z)+z\cdot\sinh(y/z)] -$$

$$- \exp\{-(a-1)y\}\cdot[\cosh(y/z)-z\cdot\sinh(y/z)]$$

$$= 2a(1+\beta)y + 2\{1-(1/z^2)\} \times$$

$$\times [y\cdot\cosh\{(a-1)y\} + \sinh\{(a-1)y\} - a\cdot y] \qquad (3.9)$$

where,

$$y=(1/a)\cdot[6\cdot(\nu_i+\nu^*)/\nu]^{1/2}$$

$$z=[1+(\nu^*/\nu_i)]^{1/2}$$

$$a=(I/I^*)^{1/2}$$

and, for CO_2 radiation,

$$\beta=.2$$

In this expression, ν is the energy acquisition frequency. This is given by, $\nu=1/\tau$, where τ is the time required for an electron, oscillating in the electric field, to reach the ionization energy. From equation (3.8) this is calculated to be $\nu=3.2\cdot10^{10}$ sec^{-1}. The excitation frequency, ν^*, is estimated by averaging the electron velocity and the excitation cross-section for hydrogen over the energy interval $I^*<\epsilon<I$, giving,

$$\nu^*=N_0\cdot\sigma^*\cdot v^*$$

$$=(1\cdot10^{18}\text{cm}^{-3})\cdot(5\cdot10^{-17}\text{cm}^2)\cdot(2\cdot10^8\text{cm/sec})$$

$$\simeq10^{10}\text{sec}^{-1}$$

Solving equation (3.9) numerically gives, $\nu_i\simeq5\cdot10^9$ sec^{-1}. This gives an electron doubling time, $\tau_d\sim200$ psec or a time of ~10 nsec for ionization.

However, this result involves numerous averages and estimates and there is a strong E-field dependence. With the electric field in the range, $6\times10^{6}<|E|<2\times10^{7}$ volts/cm then a range of 3 to 30 nsec is found for the ionization time.

3.3 Laser Beam Absorption

Once breakdown has occurred, the plasma continues to absorb the laser energy by way of the inverse bremsstrahlung process. An electron, oscillating in the electric field of the laser light, collides with an ion and the organized oscillatory motion of the electron is randomized, thereby increasing the electron temperature.

As the laser energy is absorbed by the plasma, the plasma energy increases as $K\cdot I$, where K is the absorption coefficient for inverse bremsstrahlung. Dawson(1964) provided a derivation of this coefficient. For a uniform, homogeneous plasma the inverse bremsstrahlung absorption coefficient is given by Johnston and Dawson(1973) as,

$$K = \frac{16\pi Z^{2}(N_{e}\cdot N_{i})e^{6}\ln\Lambda}{3c\nu_{0}^{2}(2\pi m\cdot kT_{e})^{(3/2)}\{1-(\nu_{p}/\nu_{0})^{2}\}^{(1/2)}} \qquad (3.10)$$

where

m =the electron mass
e =the electron charge
N =the electron density
kT_{e} =the electron temperature
$Z\cdot e$=the ion charge
N_{i} =the ion density
c =the speed of light
ν_{0} =incident laser frequency
ν_{p} =the plasma frequency

and,

$\ln\Lambda$=the Coulomb logarithm

The argument of the Coulomb logarithm is defined by the maximum to minimum impact parameter involved in the scattering process. In cases where the collision frequency is much less than the plasma frequency,

$$\Lambda = (4\pi\epsilon_0 m\cdot v_t)/(Ze^2\omega_p) \tag{3.11}$$

However, in cases where the collision is governed by the high frequency incident electromagnetic radiation, ω_0, and if the plasma is well underdense so that $\omega_0 >> \omega_p$ then the expression for the Coulomb logarithm must be adjusted (Shkarofsky et al.,1966) to give,

$$\Lambda = (4\pi\epsilon_0 m\cdot v_t)/(\zeta Ze^2\omega_0)$$

$$\text{where } \zeta = 1.781 \tag{3.12}$$

For plasma conditions typical of this study, the collisional Coulomb logarithm is, from equation (3.11),

$$\ln\Lambda \simeq 9.0 \tag{3.13}$$

The frequency dependent Coulomb logarithm can be estimated by assuming the density condition, $n/n_c = .025$, so that,

$$\begin{aligned} \ln\Lambda &= 9.0 - \ln\{\zeta\cdot(\omega_0/\omega_p)\} \\ &= 9.0 - \ln\{1.781/\sqrt{.025}\} \\ &= 6.8 \end{aligned} \tag{3.14}$$

For inverse bremsstrahlung absorption the input laser frequency governs the collision process so that, with the above density condition, $\ln\Lambda = 6.8$ and equation (3.10) reduces to,

$$K \simeq 7\cdot 10^{-35}\cdot N^2/T^{(3/2)}\ \mathrm{cm}^{-1} \qquad (3.15)$$

where $|N|=|\mathrm{cm}^{-3}|$ and $|T|=|\mathrm{ev}|$.

The reduction in absorption with increasing plasma temperature is of particular importance. The effect is such that as the plasma temperature increases, it becomes more transparent to the laser and the laser penetrates further into the plasma.

The inverse bremsstrahlung absorption length, L, is defined as, $L=1/K$ cm. With an electron density of $N=10^{18}\mathrm{cm}^{-3}$ the absorption length will range from .5 to 5 cm as the electron temperature ranges from 10 to 50 eV.

It is worthwhile at this point to estimate the electron-ion temperature ratio.

Neglecting thermal conduction losses, the heating equations can be written as,

$$\partial T_e/\partial t = (2/3)\cdot KI/nk - (T_e - T_i)/\tau \qquad \text{a)}$$

$$\partial T_i/\partial t = (T_e - T_i)/\tau \qquad \text{b)} \qquad (3.16)$$

where T_e = the electron temperature
T_i = the ion temperature.
τ = the electron-ion energy equipartition time

Defining,

$$a = (2/3)\cdot(K/nk)\cdot T_e^{(3/2)}$$

$$\simeq 3.\cdot 10^{-16} n \quad |\mathrm{ev}^{(5/2)}\mathrm{cm}^2/\mathrm{watts\text{-}sec}|$$

and,

$$b = 3.\cdot 10^{-8}\cdot n\cdot T_e^{(3/2)} \quad |ev^{(3/2)}/sec|$$

and combining the above equations (with $dI/dt=0$) into a single equation for T_e (Offenberger, 1977),

$$d^2T_e/dt^2 + (3/2)(1/T_e)(dT_e/dt)^2 +$$
$$+ (2b/T_e^{(3/2)})(dT_e/dt) = abI/T_e^3.$$

The spatial dependence has been dropped so that T_e is a function of time alone. From Rehm(1970), the time dependence for the electron temperature (based on bleaching wave heating) may be taken as,

$$T_e = T_0\cdot t^{2/5}.$$

Substituting this into the above equation for T_e one obtains,

$$T_e^{(5/2)} = (1.2\cdot aI)\cdot t.$$

Using this result in equation (3.16-a), and setting $\alpha_t = T_e/T_i$, one obtains,

$$\alpha_t = \{1 - .52\cdot(aI/bT_e)\}^{-1}. \qquad (3.17)$$

Using the above definitions for a, b, and T_e this becomes,

$$\alpha_t = \{1 - .15\cdot 10^9/(n\cdot t)\}^{-1}.$$

Or, with a typical experimental value of $n \sim 5\cdot 10^{18}\,cm^{-3}$,

$$\alpha_t = \{1 - 3.\cdot 10^{-11}/t\}^{-1}.$$

Clearly, for values of $t>1$ nsec, setting $T_e = T_i$ (i.e. $\alpha_t = 1$) will be valid.

3.4 Axial Wave Propagation

Rehm(1970) has found that the response of a plasma slab to incident laser radiation is governed by two parameters; the Bouguer number and the Boltzmann number.

The Bouguer number, α, is the ratio of the characteristic length, L, to the absorption length, L. So,

$$\alpha = \mathrm{L}/\mathit{L} \tag{3.18}$$

For $\alpha \ll 1$ very little laser energy is absorbed and the plasma is essentially transparent to the laser light. For $\alpha \gg 1$ the laser energy is entirely absorbed in a very narrow region within the plasma.

The Boltzmann number, β, is the ratio of the convective energy flux to the incident laser energy flux. So,

$$\beta = (a \cdot \rho C_v T)/I \tag{3.19}$$

where,

$\rho C_v T$= the internal energy per unit volume
a= the acoustic velocity
I= the incident laser intensity

With $\beta \ll 1$, the plasma response is governed primarily by laser absorption. Effects due to actual plasma motion will be small. If $\beta \gg 1$, the plasma motion becomes the main factor describing the response. Laser heating will only be a perturbation.

For $\beta \ll 1$, Rehm describes the plasma behaviour according to two time scales: the fluid response time, τ_m and the energy addition time, $\tau_{\cdot}$.

The fluid response time is the time required for an acoustic signal to travel a distance equal to the absorption length. Thus,

$$\tau_m = L/a \tag{3.20}$$

The energy addition time is the time required for a plasma element to double its initial internal energy through the absorption of laser energy. Thus,

$$\tau_* = (\rho C_v T)/(I \cdot K) \tag{3.21}$$

Clearly, $\beta = \tau_*/\tau_m$. If $\beta << 1$ then a plasma element will absorb energy much more rapidly than it can respond (acoustically) to another plasma element ($\tau_m >> \tau_*$).

Using these two time scales, Rehm describes two phases of the laser-plasma interaction. For early times, $t < \tau_m$, the plasma remains stationary and the governing equations can be solved analytically. At later times, $t > \tau_m$, plasma flow is induced by pressure gradients generated by the laser heating. In this case, the early time solution is supplemented numerically.

With $\alpha >> 1$ and $\beta << 1$, length is scaled to the absorption length and time is scaled to the energy addition time. In one-dimension, the governing equations are,

conservation of mass (continuity):

$$\partial\rho/\partial t + (v\cdot\partial\rho/\partial x + \rho\cdot\partial v/\partial x) = 0 \qquad (3.22)$$

conservation of momentum:

$$m\cdot(\partial v/\partial t + v\cdot\partial v/\partial x + (1/\rho)\cdot\partial p/\partial x) = 0 \qquad (3.23)$$

conservation of energy:

$$\partial S/\partial t + v\cdot\partial S/\partial x = IK/\rho T \qquad (3.24)$$

equation of state:

$$p = p_0\cdot\exp(S) = \rho T/\gamma \qquad (3.25)$$

where,

ρ=density
v=velocity
p=pressure
S=entropy per unit mass

Absorption is taken to be via classical inverse bremsstrahlung.

Following Rehm, the dependent variables are expanded in powers of β,

$$f = f^{(0)} + \beta f^{(1)} + \beta^2 f^{(2)}\ldots$$

Taking the laser intensity at the laser-plasma interface to be constant, the zeroth-order set of equations are then solved exactly.

In the long time limit, t>>1 (scaled in units of τ_+), Rehm finds two plasma regions interfaced at a position χ (scaled in units of L).

$$\chi = (2/3)\cdot[(5/2)\cdot t]^{(3/5)} \qquad (3.26)$$

Then, for $x \ll \chi$ the temperature and intensity equations become,

$$T^{(0)} \simeq [(5/2)\cdot t]^{(2/5)}\cdot\{1 + x/[(5/2)\cdot t]^{(3/5)}\}$$
$$I^{(0)} \simeq 1 + x/[(5/2)\cdot t]^{(3/5)} \qquad (3.27)$$

and for $x \gg \chi$,

$$T^{(0)} \simeq 1 + 2\cdot\exp\{x + 2/3\cdot[(5/2)\cdot t]^{(3/5)}\}$$
$$I^{(0)} \simeq 2\cdot\exp\{x + 2/3\cdot[(5/2)\cdot t]^{(3/5)}\}/[(5/2)\cdot t]^{(2/5)} \qquad (3.28)$$

The parameter χ defines the front of a propagating heating wave. Behind the front the temperature decreases linearly with position. Ahead of the front the temperature exponentially approaches the ambient temperature.

Using equation (3.15) and (3.21), the expression for χ, equation (3.26), may be scaled to normal units with time in seconds and distance in centimeters. This gives,

$$\chi = (9.52\cdot 10^{24})\cdot(I^{(3/5)}\cdot t^{(3/5)}\cdot N^{-(7/8)})\ |\mathrm{cm}| \qquad (3.29)$$

where,

$|I| = \mathrm{watts/cm^2}$ $\quad |N| = \mathrm{cm^{-3}}$

This heating wave propagates without introducing any plasma motion ($t \ll \tau_m$). The process is explained as follows. The laser energy is absorbed in a narrow region ($\alpha \ll 1$). The plasma temperature in this region rises rapidly. As the temperature rises, the absorption drops rapidly allowing the laser to pass through the region. The adjacent region absorbs the laser energy and is consequently heated. In this way the heating wave propagates.

Because successive layers of the plasma are made transparent to the laser radiation, the laser is said to bleach through the plasma and the heating wave is referred to as a bleaching wave.

With $\beta \ll 1$ and $\alpha \gg 1$ or $\alpha \simeq 1$ but for times which are comparable to the fluid response time, a numerical solution is used to supplement these results. Rehm finds that steep gradients develop in the plasma density (plasma motion now becomes significant) indicating the formation of a shock. Since laser energy is continuously deposited behind the shock, it is expected that the front will propagate as a detonation wave. Optical detonation and shock formation will be discussed in a later section.

Burnett and Offenberger(1976) have derived a self-regulating bleaching wave solution for the situation where $\beta \ll 1$ and $\alpha \simeq 1$.

The ratio of the plasma length, L, to the absorption length, $\mathcal{L}$ ($=1/K$), was taken to be (Krokhin, 1971), $K \cdot L \simeq .67$.

Using equation (3.15) for *K* and solving for the electron temperature T,

$$T = (C_1 \cdot N^2 \cdot L)^{(2/3)} \qquad (3.30)$$

where $C_1 = 1 \cdot 10^{-34}$.

If the laser energy of intensity I, impinging on a volume element, $dV = dA \cdot dL$, in a time dt, is completely absorbed, then the internal energy of the plasma element will be,

$$E_i = (I \cdot dt \cdot dV)/dL$$

however, substituting, $E_i = (3/2) \cdot N \cdot kT \cdot dV$ and re-arranging gives,

$$dL/dt = I/(C_2 \cdot N \cdot T) \qquad (3.31)$$

where $C_2 = (3/2)k$. Using equation (3.30) for T, one obtains,

$$L^{(2/3)} \cdot dL = \{I/(C_1^{(2/3)} \cdot C_2 \cdot N^{(7/3)})\} \cdot dt$$

Integration (assuming I and N to be constant) gives,

$$(3/5) \cdot L^{(5/3)} = (I \cdot t)/\{C_1^{(2/3)} \cdot C_2 \cdot N^{(7/3)}\}$$

or,

$$L = [(3/5) \cdot 1/\{C_1^{(2/3)} \cdot C_2\}]^{(3/5)} \cdot (I^{(3/5)} \cdot t^{(3/5)} \cdot N^{-(7/5)}) \qquad (3.32)$$

With, $C_1 \simeq 1 \cdot 10^{-34}$ and, $C_2 \simeq 2.4 \cdot 10^{-16}$ then,

$$L = (3.7 \cdot 10^{24}) \cdot (I^{(3/5)} \cdot t^{(3/5)} \cdot N^{-(7/5)}) \quad |cm| \qquad (3.33)$$

where, $|I|$=watts/cm^2 and $|N|$=cm^{-3}

This expression for L (where $a \simeq 1$) and that given by Rehm (where $a >> 1$) show identical intensity, density and temporal dependence. The constant of proportionality, however, is ~2.5 times larger when $a >> 1$. This is expected since if $\alpha \simeq 1$ some portion of the laser will not be absorbed, thereby reducing the energy content of the plasma. Furthermore, with $\alpha \simeq 1$ some laser energy is absorbed well behind the front and may not contribute to the velocity of the plasma front.

The parameters found in these bleaching wave models may be estimated from expected experimental conditions. With,

$$\begin{aligned} \beta &= \tau_{+}/\tau_{m} \\ &= (3/2)\cdot(NkT\alpha)/I \\ &= 2.4\cdot 10^{-13} NT^{3/2}/I \end{aligned}$$

where,

$$|I| = |\text{watts/cm}^2| \qquad |T| = |\text{ev}| \qquad |N| = |\text{cm}^{-3}|$$

For conditions found in this study, β is found to be in the range; $10^{-4} < \beta < 10^{-1}$ so that taking $\beta << 1$ is generally valid.

The value of the parameter α is somewhat less certain. In any case, as long as plasma motion is not induced, that is, as long as $t << \tau_m$, then a bleaching wave solution is expected.

The fluid response time is, however, α-dependent since,

$$\tau_m = L/a = L/(\alpha \cdot a).$$

The acoustic velocity, a, may be written,

$$a \simeq 10^6 \cdot T^{(1/2)} \text{ cm/sec}.$$

Using this expression and taking T=50 eV then,

$$\tau_m \simeq 1.4\cdot 10^{-7}(L/a)^{\text{[illegible]}}\ \text{sec} \qquad (3.34)$$

If the interaction is self-regulating and $a \simeq 1$ is valid throughout the experiment, then as the plasma column length increases, the fluid response time also increases. Using equation (3.33) for L, and setting $I=10^9$ watts/sec and $N=10^{18}$ cm^{-3}, then,

$$\tau_m = .88\cdot 10^{-2}\cdot t^{3/5}$$

Thus, $t<\tau_m$ until $t=\tau_m=7.2\mu$sec and no plasma motion is expected until late in the experiment.

If on the other hand, the absorption length remains constant and $\simeq 1$ cm throughout the course of the experiment, then τ_m would be a constant .14 μsec. This suggests that after a rather short period of time, plasma motion would be expected to generate a shock wave and the axial behaviour would no longer be described as a bleaching wave but rather as optical detonation.

Further discussion of the a parameter will be given in Chapter 4.

3.5 Optical Detonation

The laser-induced breakdown studies of Ramsden and Davies(1964) showed that following breakdown, an ionizing shock developed. This shock propagated in the anti-laser direction with a velocity of $\sim 10^7$ cm/sec. The propagation is explained by means of optical detonation.

Optical detonation begins with the absorption of laser energy in a narrow region of the plasma. The heated plasma expands rapidly outwardly into the ambient gas setting up a shock wave. At the shock front, the gas is ionized and, in the region nearest the incoming laser light, readily absorbs the laser energy. The absorbed energy maintains the shock and the propagation continues back toward the laser.

Because of its similarity to chemical detonation, the process is referred to as optical detonation. The velocity with which the front will propagate is shown to be the Chapman-Jouget point.

Ahlborn et al.(1982), have described the propagation of the plasma front along the axis of the laser-heated solenoid in terms of optical detonation. The laser energy is assumed to be absorbed in a narrow plasma region behind an ionizing shock front. As the plasma temperature rises, the laser penetrates further and drives the shock forward. The approach is similar to that of Raizer(1965) but with more detailed description of the shock interaction.

Following Ahlborn et al.(1982),the enthalpy behind the shock (moving with velocity, v) is given by,

$$h_2 = \{2\cdot(g_2)^2/(g_2+1)^2\}\cdot v^2$$

where $g_2 \simeq 1.2$ for an ionizing shock.

For complete ionization, the enthalpy required is given as,

$$h^{*} = (5/2)\cdot\{2kT/m_i\} + \{E_i+(D/2)\}/m_i \qquad (3.35)$$

where,

E_i=the ionization potential
D =the dissociation potential
m_i=the ion mass
kT=the gas temperature required for ionization
$\simeq .1\cdot\{E_i+(D/2)\}/m_i$

Taking $h_2=h^{*}$, v^2 may be written,

$$v^2 = 1.68\cdot(3/2)\cdot\{E_i+(D/2)\}/m_i$$

and with,

E_i=13.7 eV for hydrogen
D =4.5 eV for H_2
and $m_i=1.67265\cdot 10^{-17}$kg

then,

$$v \simeq 6.6 \text{ cm}/\mu\text{sec} \qquad (3.36)$$

This velocity is a minimum since a lower value would imply a lower enthalpy state than that required for ionization. Furthermore, it is noted that the process is self-regulating so that the optical detonation front propagates with a constant velocity.

The process is seen to be self-regulating since an increase in velocity implies that the temperature in the post-shock region increases which reduces the energy absorption (which is via inverse bremsstrahlung) which in turn will decrease the velocity. Alternatively, should the velocity decrease, then the temperature behind the shock would drop with the result that the energy absorption would increase and the velocity would adjust upward.

3.6 Radial Dynamics

As the plasma column develops, the plasma behind the ionization and heating fronts expands radially against the axial magnetic field lines. The one dimensional models presented above do not include effects associated with this expansion. These two dimensional effects will be considered later. Here a simple model of the radial behaviour is discussed.

The diffusion equation, $\partial N/\partial t = D\cdot\nabla^2 N$ (where D is the diffusion coefficient), is solved by the method of separation of variables (see Chen, 1974, pg.142) whereby the density, N, is defined by separate functions of time and space;

$$N(r,t) = T(t)\cdot S(r)$$

The temporal component has the solution,

$$T(t) = T_0\cdot e^{-t/\tau}$$

The spatial component obeys the equation,

$$\nabla^2 S = -(1/D\tau)\cdot S$$

In cylindrical co-ordinates this becomes,

$$d^2S/dr^2 + (1/r)\cdot dS/dr + S/(D_\perp\cdot\tau) = 0 \qquad (3.37)$$

The solution to this equation is a zeroth-order Bessel function. Satisfying the boundary condition that at the edge of the plasma ($r=r_0$) the plasma density is zero, yields the relation,

$$r_0/(D_\perp\tau)^{(1/2)} = 2.405 \qquad (3.38)$$

so τ, the characteristic thermal loss time, is given by,

$$\tau = (1/D_\perp)\cdot(r_0/2.405)^2 \qquad (3.39)$$

With an applied axial magnetic field, the radial energy losses should be dominated by the thermal diffusion of ions. For a hydrogen plasma, the ion diffusion coefficient perpendicular to the magnetic field is given by (Spitzer, 1962),

$$D_{\perp i} = \frac{(1.81\cdot 10^{19})\cdot T_i^{(5/2)}}{N\cdot \ln\Lambda(1+\omega_i^2\tau_i^2)} \qquad (3.40)$$

with $|T_i|$=ev and $|N|$=cm^{-3}.

The ion cyclotron frequency, ω_i, is given by,

$$\omega_i = eB/m_i c$$

$$= 9.56\cdot 10^6\cdot B \quad \mathrm{sec}^{-1} \qquad (3.41)$$

with $|B|$=kG.

The ion collision frequency, $\nu_i = 1/\tau_i$, is given by,

$$\nu_i = N\cdot\sigma_s(T_i/m_L)^{(1/2)}$$

with,

$$\sigma_s = 8\pi e^4 \ln\Lambda/(m_i v^2)^2$$

then,

$$\nu_i = 5.66\cdot 10^{-8}\cdot N\cdot \ln\Lambda/T_i^{(3/2)}. \qquad (3.42)$$

So that,

$$\omega_i\tau_i = 1.69\cdot 10^{14} B\cdot T^{(3/2)}/(N\cdot\ln\Lambda) \qquad (3.43)$$

with $|B|$=kG $|T_i|$=ev and $|N|$=cm^{-3}

The diffusion coefficient is, therefore, a function only of the plasma temperature, plasma density and the magnetic field strength.

Using this expression in equation (3.40) for the diffusion coefficient and substituting this result into the expression for the thermal loss time (equation 3.39) then the ion thermal radius may be plotted as a function of time for various magnetic field, plasma temperature, and plasma density values.

In Figure 3.1 this calculated radial position is plotted versus time for varying magnetic field strengths and plasma densities. The plasma temperature was set to 50 eV. The increased confinement with a stronger field is clear. This is due to a decrease in the Larmour radius and a stronger tying of the ions to the magnetic field lines.

As the plasma density is increased the behaviour becomes collisionally dominated and the confining effect of the magnetic field is considerably reduced.

Ahlborn et al.(1982) have obtained a relation giving an upper limit to R, the plasma column radius. As mentioned, this model describes the propagating front of the plasma column in terms of an ionizing shock. The region well behind the front is assumed to have reached a steady state. This equilibrium column is divided into three regions; the laser absorption zone on the axis, a surrounding heat conduction region, and an outer radiative cooling zone. By balancing the heat flux from the core with the cooling rate from the radiative cooling region, an expression for the column radius is obtained,

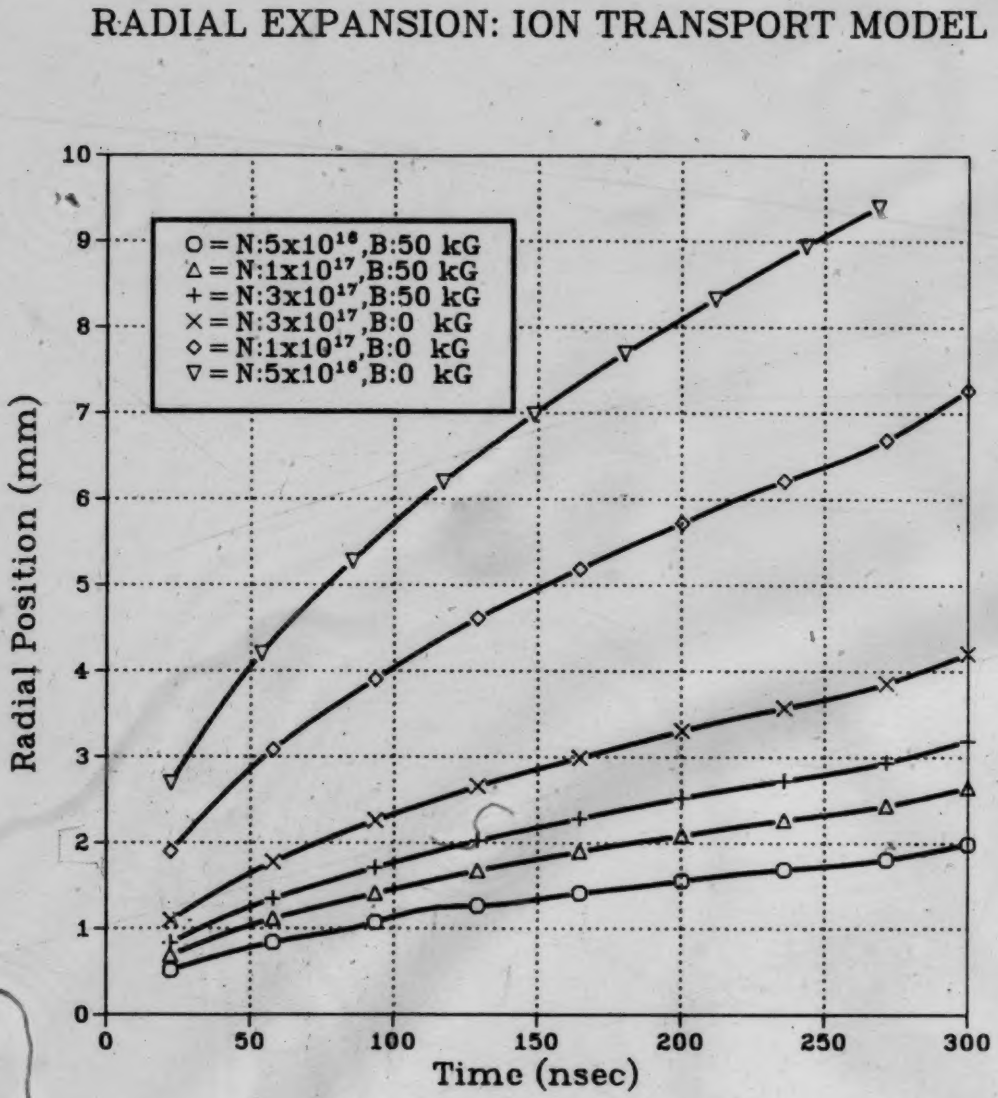

Figure 3.1 Dependence of Radial Expansion on B-field Strength and Plasma Density: Ion Transport Model

$$R = 3.7\cdot 10^{-2}(n/n_0)P^{(3/8)}B^{-(1/4)}\chi^{-(5/8)} \qquad (3.44)$$

where P=the input laser power |watts|
B=the magnetic field strength |gauss|
(n/n_0)=the ratio of on-axis density to fill density
and $\chi=\Delta R/R$
where, ΔR=temperature gradient scale length

This expression for the radius represents an upper limit since conduction heat losses in the outer region (which may be substantial) are not considered.

The density ratio can be estimated by assuming that the plasma conductivity is high enough that the magnetic field is transported by convection rather than diffusion. That is, the field moves with the plasma. This is the frozen field condition and yields the relation,

$$n/n_0=B/B_0 \qquad (3.45)$$

where B_0 is the external magnetic field and B is the imbedded field. If it is further assumed that locally the plasma pressure balances the magnetic pressure of the external field then,

$$2nkT + B^2/8\pi = B_0^2/8\pi . \qquad (3.46)$$

Substituting $n=n_0B/B_0$ into this equation and re-arranging gives,

$$B^2 + (16\pi n_0kT/B_0)\cdot B - B_0^2 = 0 .$$

With $A=8\pi n_0kT/B_0^2$, we have

$$B=B_0\cdot[\sqrt{A^2 + 1} - A]$$

or,

$$n/n_0=B/B_0=\sqrt{\{A^2+1\}}-A\,. \qquad (3.47)$$

Taking, for representative experimental values, $n_0=1\cdot10^{18}$ cm^{-3}, $B_0=50$ kG, and $T=50$ eV then $A\simeq.8$ and,

$$n_0/n\simeq2.0\,.$$

Letting $\Delta R/R=1$, using a typical experimental value of $P=10^4$ watts and with the above density ratio, equation (3.40) gives a limiting value for the column radius of 1.2 cm.

Ahlborn et al.(1982) have considered the density ratio in light of the Nernst-Wienecke effect. The Nernst effect is a result of hot ions diffusing out from the core producing azimuthal currents which in turn, through the Lorentz force, enhance the confinement of the plasma. The Wienecke effect is a result of the ionization of neutrals which have diffused into the core. In the presence of a magnetic field the diffusion of ions from the core is inhibited while the diffusion of neutrals is unaffected. In combination these effects can increase the plasma density on axis. Ahlborn et al. show that the density ratio can be written,

$$n_0/n=(T/1.7)^{(1/4)}.$$

Note that for $T=50$ eV, one obtains $n_0/n=2.3$, which is just slightly larger than that obtained from the frozen field and pressure balance conditions.

Using a derived relation for the plasma temperature in the column (discussed in the next section), Ahlborn et al.(1982) obtain, for the limiting column radius, the expression,

$$R = 2.4 \cdot P^{(1/4)} \cdot \chi^{-(3/4)} \cdot B^{-(1/2)}. \tag{3.48}$$

Using the same values as before, one obtains a maximum radius of $R \simeq 1.1$ cm.

The Nernst-Wienecke effect, then, does not lead to a significantly different limit to the column radius as compared to that predicted from the assumptions of pressure balance and high conductivity.

3.7 Energy Balance and Plasma Heating

In discussing energy balance, the temperature equations describing the heating and transport processes will be simplified by making certain assumptions.

First, advection terms will be ignored so that the total time derivative is given simply by $\partial T/\partial t$. Second, it will be assumed that the magnetic field is transported by convection rather than diffusion, thereby eliminating joule heating. Finally it will be assumed that energy transport is through thermal conduction rather than convection.

These are the same simplifying assumptions used by Burnett and Offenberger(1974). The resulting heating equations are,

---

$$\begin{aligned}\partial T_e/\partial t &= (2/3) \cdot \mathit{K} I/n\mathit{k} - (T_e - T_i)/\tau + \\ &\quad + (2/3n\mathit{k}) \cdot (1/r)\partial/\partial r\{K_{e\perp}(\partial T_e/\partial r)\} \\ &= a \cdot I - (T_e - T_i)/\tau + (2/3n\mathit{k}) \cdot (1/r)\partial/\partial r\{K_{e\perp}(\partial T_e/\partial r)\}\end{aligned}$$

$$\partial T_i/\partial t = (T_e - T_i)/\tau + (2/3nk)\cdot(1/r)\partial/\partial r\{K_{i\perp}(\partial T_i/\partial r)\} \tag{3.49}$$

where T_e=the electron temperature
and T_i=the ion temperature.

Burnett and Offenberger(1974) give the following inequality which must hold for the above assumptions to be valid.

$$P_t > P > P_m$$

where P is the input laser power

and where (in cgs with $|B|=|kG|$),

$$P_t=3\cdot 10^6\cdot K_{e\perp}\cdot B^2/16\cdot K\cdot n$$

and

$$P_m=3\cdot 10^6\eta\cdot c^2\cdot B^2/32\pi\cdot K\ .$$

These power levels are determined from limitations on v, the expansion velocity. P_m is related to the requirement that the magnetic field be frozen to the plasma expansion. This provides a lower limit on the expansion velocity so that the magnetic diffusion time will be much less than the time for expansion. P_t is related to the requirement that thermal conduction dominate thermal convection. This provides an upper limit for the expansion velocity.

These power levels can be evaluated and compared with the input power level, $P=10^8$ watts, to give the maximum B-field and the minimum plasma temperature under which these assumptions will be valid.

With, $\omega_e^2\tau_e^2>>1$ then, $K_{e\perp}\simeq 1.3\cdot 10^{24}T_e\cdot B^{-2}K$ which gives,

$$P_t= 2.4\cdot 10^{31}T_e/n.$$

Setting $n=5\cdot 10^{17}$ cm^{-3} and $P=10^{13}$ ergs/sec, then the condition that $P_t>P$ may be written,

$$T_e>20 \text{ eV}$$

The other power condition involves the plasma resistivity, η, which is given by,

$$\eta\simeq 2\cdot 10^{-14}\ln\Lambda/T_e^{(3/2)} \text{ (esu)}$$

where $|T_e|$=ev.

Using this expression for η, we have,

$$P_m= 6.6\cdot 10^{44}B^2/n^2.$$

With $n=5\cdot 10^{17}$ cm^{-3} and $P=10^{15}$ ergs/sec, then the condition that $P_m<P$ may be written,

$$B<150 \text{ kG}$$

These limitations on the plasma temperature and the field strength should be easily satisfied in the laser-heated solenoid experiments thereby validating the use of the quasi-static approximation.

Another simplification may be made by taking the ion thermal losses to dominate the electron thermal losses (i.e. $K_{i\perp}>>K_{e\perp}$). The ratio of these conductivities may be written,

$$K_{i\perp}/K_{e\perp}=\sqrt{(m/M)}\cdot\{1+(M/m)\cdot(\omega_i\tau_i)^2\}/\{1+(\omega_i\tau_i)^2\}$$

For conditions typical of this experiment, $.5<(\omega_i\tau_i)<10$. This gives $5<(K_{i\perp}/K_{e\perp})<40$ which justifies this simplification.

The rate of energy equilibration has previously been shown to be very rapid, $\tau\simeq20$ nsec, so that for times greater than this $T_e=T_i$ and the temperature equations may be further simplified.

The result of these simplifications is that heating from the incoming laser is balanced by radial ion thermal conduction losses. This gives,

$$I\mathcal{K}=1/r\cdot\{\partial/\partial r(K_{i\perp}\cdot r\partial T_e/\partial r)\}\,.$$

Approximating,

$$(1/r)\cdot\partial/\partial r(r\cdot\partial T_e/\partial r)\simeq(1/R)\cdot T_e/\Delta R$$

where R is the equilibrium plasma column radius. Assuming the laser beam size will match the plasma size then, $P=I\cdot\pi R^2$ and,

$$T_e = P\cdot(\Delta R/R)\cdot\pi\mathcal{K}/K_{i\perp} \tag{3.50}$$

With $\omega_i\tau_i>>1$, we have,

$$\mathcal{K}/K_{i\perp}= 3.124\cdot10^{-8}B^2/T_e \qquad |T_e|=|ev|\,.$$

Substituting into equation (3.45) gives

$$T_e^2 \simeq (3.124/\pi)\cdot P\cdot(\Delta R/R)\cdot B^2\cdot 10^{-8}$$

or,

$$T_e \simeq P^{(1/2)}(\Delta R/R)^{(1/2)}\cdot B\cdot 10^{-4} \qquad (3.51)$$

Ahlborn et al.(1982) found the same scaling for the plasma temperature in the equilibrium region behind the shock front in their model of the laser-heated solenoid.

Again, taking representative experimental values, $P=10^8$ watts, $B=50$ kG, and $\Delta R/R=1$ then the plasma temperature may be estimated. Substituting into equation (3.51) yields $T_e \simeq 50$ eV.

Considering the case where $\omega_i \tau_i$ is not large compared with unity, one obtains a more complicated expression for $K/K_{i\perp}$, namely,

$$K/K_{i\perp} \simeq 10^{-36}\cdot(10^2 n^2 + 2.9\cdot 10^{28} B^2 T^3)/T^4.$$

Substituting this into equation (3.50) yields a fifth order equation in T, the temperature. The solution now depends on the plasma density as well as the laser power and the magnetic field strength. Taking $P=10^8$ watts and $B=50$ kG as before and letting n vary from 10^{17}-10^{18} cm^{-3} yields a plasma temperature in the range of 55 to 85 eV.

Near the end region of the plasma column (or near the orifice), the calculations given above will no longer be valid since axial convection losses will dominate radial losses. If one assumes that these losses balance the laser heating then,

$$KI=(3/2)nkT_e/\tau$$

where τ, the characteristic convection loss time is defined as,

$$\tau= L/2a = L/(2.5\cdot 10^{6}T_e^{(1/2)})$$

Using equation (3.11) for K gives,

$$T_e = 5\cdot 10^{-8}(n\cdot I\cdot L)^{(1/3)}\ \mathrm{eV} \tag{3.52}$$

Using representative experimental values, $n=5\cdot 10^{17}$ cm^{-3}, $I=5\cdot 10^{8}$ W/cm^2, $L=2$ cm then the plasma temperature is estimated to be 40 eV.

3.8 Two Dimensional Numerical Model

3.8.1 SHELL

The two dimensional (2-D) code, SHELL, was developed by McMullin et al.(1979) to simulate the magnetohydrodynamics of a cylindrically symmetric plasma with an imbedded solenoidal magnetic field.

The SHELL code has the following features:

1. The plasma is treated as a 2-temperature, ideal MHD fluid.

2. A solenoidal magnetic field permeates the plasma.

3. Magnetic diffusion is allowed for by setting the electrical conductivity to be finite.

4. Electron-ion energy exchange is at the classical equipartition rate.

5. Shock waves are handled by including an artificial viscosity term.

6. A magnetic flux co-ordinate system is used.

Because the motion of the plasma is essentially one dimensional along the field lines, the selection of the field lines as a co-ordinate system can simplify the analysis. Furthermore, since heat conduction along the field lines is much greater than that perpendicular to them, the heat flow equations are more easily handled with a co-ordinate system which is tied to the field lines (Anderson, 1974).

To further simplify the calculations, the code takes the slope of a field line to be a small quantity, ϵ, so that terms of order ϵ^2 can be ignored. The condition that $\epsilon \ll 1$ is generally easily satisfied in the laser-heated solenoid experiment.

Using subscript 'z' to refer to axial components, subscript 'n' for radial components, subscript 's' to identify the species (electron or ion) and noting that N=the electron number density, M=the ion mass, V=the fluid velocity, P=the scalar pressure and, finally, the total derivative, d/dt, is the convective derivative:

$$d/dt = \partial/\partial t + V_z \cdot \partial/\partial z + V_n \cdot \partial/\partial r \quad .$$

The governing 2-D equations can be summarized:

---

conservation of mass(continuity):

$$dN/dt + N\{\partial V_z/\partial z + (1/r)\partial/\partial r(rV_n)\} = 0 \qquad (3.53)$$

conservation of momentum:

axially,

$$m \cdot N \cdot dV_z/dt = -\partial/\partial z(P+q_z)\ (B_n/4\pi) \cdot (\partial B_z/\partial r - \partial B_n/\partial z)$$

radially,

$$m \cdot N \cdot dV_n/dt = -\partial/\partial z(P+q_n)\ (B_z/4\pi) \cdot (\partial B_z/\partial r - \partial B_n/\partial z)$$

where, q = an artificial viscosity term (3.54)

temperature:

$$N \cdot dT_s/dt - (\gamma-1) \cdot T_s \cdot dN/dt =$$

$$= N \cdot dT_s/dt|_c + (\gamma-1) \cdot (NE^s_x - \underline{\nabla} \cdot \underline{Q}_s + J^2/\sigma_\perp) \qquad (3.55)$$

where, on the RHS,

the first term = the collisional energy exchange between species,
the second term = the external energy source term,
the third term = the heat conduction term,
and,
the final term = the Ohmic heating term.

These equations are transformed to magnetic flux co-ordinates and solved by a 2-step second order Euler method. The spatial derivatives were determined by central differences.

3.8.2 HEATER

HEATER (McMullin et al., 1981) is a 2-D code used to describe the propagation of the laser through the plasma. The effects of absorption, refraction, and diffraction of the beam by the plasma are included in HEATER. The power absorbed and the ponderomotive forces are calculated and returned to SHELL where they are used in calculating the plasma characteristics.

Considering only spatial variations of the laser beam, the electric field, $\underline{E}(r,z)$, will satisfy the Helmholtz equation. In cylindrical co-ordinates and with cylindrical symmetry, this gives,

$$(1/r)\cdot\partial/\partial r\{r\cdot\partial\underline{E}/\partial r\} + \partial^2\underline{E}/\partial z^2 + \\ + (\omega^2/c^2)\cdot\epsilon(r,z)\cdot\underline{E} = 0 \qquad (3.56)$$

where ϵ, the dielectric constant is given by,

$$\epsilon = 1 - (\omega_p^2/\omega^2)\cdot(1 - i\nu_m/\omega) \qquad (3.57)$$

where ω_p =the plasma frequency
ω =the incident laser frequency
ν_m =the electron collision frequency.

By defining,

$$E(r,z) = \{8\pi\omega/k(z)c^2\}^{(1/2)}\cdot\psi(r,z) \times \\ \times \exp\{i[{}_0\int^z k(z')dz'\ ]\} \qquad (3.58)$$

where,

$$k(z) = \omega/c\{\mathrm{Re}\,\epsilon(0,z)\}^{(1/2)}$$

then, the time-averaged electromagnetic flux, F, will be given by,

$$F = |\psi(r,z)|^2 .$$

The value of F is used in calculating the laser power absorbed and the ponderomotive forces.

Substituting equation (3.58) into (3.56) and by assuming that variations in ψ and $k(z)$ are small, gives,

$$\partial\psi/\partial z = (i/2k)\cdot[(1/r)\cdot\partial/\partial r\{r\cdot\partial\psi/\partial r\} - q^2\cdot\psi(r,z)] \tag{3.59}$$

where,

$$q^2(r,z) = (1/c^2)\cdot\{[\omega_p^2(r,z) - \omega_p^2(0,z)] - (i\omega_p^2(r,z)\nu_m)/\omega\}$$

The first term on the RHS of equation (3.59) describes the diffraction of the beam, while the second term includes both refraction and absorption. Equation (3.59) is solved numerically in HEATER by a cubic spline method.

3.9 Stimulated Scattering

3.9.1 Preliminary Remarks

The long scale length, homogeneous, underdense plasma of the laser-heated solenoid provides a useful medium in which to study stimulated scattering processes.

In this section physical mechanisms will be discussed. The use of spectral measurements of the scattered radiation in determining plasma conditions will be outlined.

3.9.2 General Mechanisms

The basic physical mechanism underlying stimulated scattering involves the beating of an incident electromagnetic (e-m) wave with a plasma wave to produce a scattered e-m wave.

Identifying the incident e-m wave with subscript '1', the reflected e-m wave with subscript '2' and the plasma wave with subscript '3', the matching conditions which must be satisfied are,

$$\omega_1 = \omega_2 + \omega_3$$

$$\underline{k}_1 = \underline{k}_2 + \underline{k}_3 \qquad (3.60)$$

The stimulated scattering process may be unstable since the reflected and incident e-m waves also beat and produce a ponderomotive force which serves to enhance the original plasma wave. This feedback mechanism allows the plasma wave and the reflected e-m wave to grow together.

Drake et al.(1974) developed a general formalism for the 3-wave parametric instability process. From an equilibrium condition consisting of electrons oscillating in the electric field of an incident e-m wave, an electrostatic plasma wave is introduced which produces a propagating density perturbation. The Vlasov equation for the electrons, including the ponderomotive force term $\nabla\psi/m$, is,

$$\partial f/\partial t + \underline{v}\cdot\nabla f + \{-(e/m)\underline{E} - \nabla\psi/m\}\cdot\partial f/\partial\underline{v} = 0 \qquad (3.61)$$

This equation is linearized and solved giving the electron response.

The ion response (now ignoring ponderomotive effects) is similarly obtained and then related to the electron behaviour through Poisson's equation. The resultant expression for the electron density fluctuation is then incorporated into the solution to the wave equation for the side-bands generated by the interaction of the incident e-m wave and the electro-static wave. This leads to a generalized plasma dispersion relation describing the process.

In the case of stimulated scattering the electro-magnetic components of the side-bands dominate. Furthermore, by considering only the high frequency (Stokes) component, a reduced dispersion relation is obtained,

$$1/\chi_e + 1/\{1+\chi_i\} = \{2k_1^2\nu_0^2/[\omega_1(\omega-\Delta\omega)]\}\cdot\psi^2(\theta,\phi) \qquad (3.62)$$

where,

$\chi_{e,i}$ are the electron, ion susceptibilities

$\nu_0=eE_1/m\omega_1$ is the electron quiver velocity

$\Delta\omega=c^2\underline{k}\cdot\underline{k}_1/\omega_1 - c^2k^2/2\omega_1$

The angular dependence is given by,

$$\psi(\theta,\phi) = |\sin(\phi)|\cos(\theta)$$

where θ is the angle between $\underline{k}_1$, the incident e-m wave, and $\underline{k}_3$, the plasma wave, and ϕ is related to the difference in polarization of the two e-m waves.

From the wave vector matching conditions, equation (3.60), it is clear that as $\theta \to 0$ then the scattered e-m wave propagates backward. From the given angular dependence, growth rates will be maximum and thresholds will be minimum for backscattered waves.

In determining the thresholds and the growth rates, the appropriate expressions for the electron and ion susceptibilities must be determined. These expressions will depend on whether the interaction is viewed from a hydrodynamic or kinetic stand-point.

Two types of instability can be described. If the damping of the plasma wave is strong then the instability will grow only as it moves from one spatial location to another. This is referred to as a convective instability. If the damping is weak then the instability will grow temporally in any fixed location. This is referred to as an absolute instability. Threshold conditions and growth rate equations depend on the nature of the instability.

Various processes, notably Landau damping, serve to prevent the growth of plasma waves. A requirement for instability is that these damping losses be overcome by the gain from the incident e-m wave. The instability is generally limited by saturation mechanisms which may either enhance the damping losses or disrupt the phase matching conditions and stop the growth.

3.9.3 Stimulated Brillouin Scattering

Stimulated Brillouin scattering (SBS) involves the interaction of the incident laser e-m wave with an ion-acoustic plasma wave.

An ion-acoustic wave is a normal mode of the plasma. It is generated by fluctuations in the ion density. Because of ion thermal motion and electric field effects the oscillation will propagate. The ion electric field is shielded by the electrons but becomes available to affect propagation because of the thermal motions of the electrons. The dispersion relation governing the propagation of the ion-acoustic wave, therefore, depends on the temperature of the ions, T_i and the electrons, T_e. In the hydrodynamic limit, it is given by,

$$\omega/k = \{(T_e + 3T_i)/m_i\}^{(1/2)} \tag{3.63}$$

With the experimental conditions present in the laser-heated solenoid, Offenberger et al.(1976b) have shown that heavy damping and, consequently, convective growth is expected. In this case, the threshold condition is given by,

$$(2\gamma_0^2 L)/(\gamma_3 c) >> 1 \tag{3.64}$$

where,

γ_0 = the homogeneous growth rate
γ_3 = the ion-acoustic damping rate
L = the effective plasma length
c = the speed of light

The homogeneous growth rate is given by,

$$\gamma_0 = (1/2)\cdot(v_0/c)\cdot(\omega_1/\omega_3)^{(1/2)}\cdot\omega_{pi}$$

where,

$v_0 = eE_1/m\omega_1$ = the electron quiver velocity
ω_{pi} = the plasma frequency (ion)

The gain is given by,

$$G = (1/4)\cdot(\omega_p^2/\omega_1^2)\cdot(v_0^2/v_t^2)\cdot\tau_3 k_1 L \qquad (3.65)$$

where,

$v_t = (kT/m)^{(1/2)}$ = the electron thermal velocity
$\tau_3 = \omega_3/(2\gamma_3)$ = ion-acoustic damping time

The parameter τ_3 is defined (Offenberger, 1981) by,

$$\tau_3 = \tau/[\{1 + \beta^2\cdot\mathrm{Re}(F_i)\}^2 + \tau^2] \qquad (3.66)$$

where,

$$F_i = 1 - 2\cdot x\cdot\exp[-x^2]\cdot\{\textstyle\int^x \exp[t^2]dt\} +$$
$$+\ i\sqrt{\pi}\cdot x\cdot\exp[-x^2]$$

$$\beta = \sqrt{(T_e/T_i)}$$

and $\tau = \sqrt{(\pi/2)}\cdot\beta^2(\Delta\omega/kv_i)\cdot\exp[-(1/2)\cdot(\Delta\omega/kv_i)^2]$

The reflectivity, the spectral shape, and saturation mechanisms will be discussed in terms of the experimental results in Chapter 4.

3.9.4 Stimulated Raman Scattering

Stimulated Raman scattering (SRS) involves the interaction of the incident e-m wave with an electron plasma wave to generate a scattered e-m wave.

Electron density fluctuations lead to the well known plasma oscillation which will propagate as an electron plasma wave because of the thermal motions of the electrons and electric field effects. The governing dispersion relation is given by,

$$\omega_3 = \{\omega^2 + 3k^2(kT/m)\}^{(1/2)} \tag{3.67}$$

where,

$\omega_p = \{(4\pi ne^2)/m\}^{(1/2)}$ = the plasma frequency

In the laser-heated solenoid, SRS was shown experimentally (Offenberger et al., 1982a) to be described by an absolute instability. In this case the growth rate is given by,

$$\gamma = [2\gamma_0(v_2v_3)^{-(1/2)}.\{1-(\pi^{-(1/2)}.\lambda^{-(2/3)})\} - \\ - (\gamma_2/v_2+\gamma_3/v_3)] \cdot [(v_2v_3)/(v_2+v_3)] \tag{3.68}$$

where,

$\gamma_0 = k_3v_0[\omega_p/(\omega_1-\omega_p)]^{(1/2)}/2\sqrt{2}$

= the homogeneous growth rate

with,
ω_1 = the incident laser frequency
ω_p = the plasma frequency
and v_0 = the electron quiver velocity

and,

$$\lambda = \gamma_0^2/(v_2 v_3)\cdot k'$$

with $k' = d/dx\{k_1 + k_2 - k_3\}$ (for scalar wavenumbers)
= the phase mis-match gradient

and where for the three waves,
$v_i (i=1,2,3)$ are the group velocities
$\gamma_i (i=1,2,3)$ are the damping rates

and I_1 is the intensity of the incident wave.

The growth equation incorporates two threshold conditions. In the absence of damping ($\gamma_3 = \gamma_2 = 0$) then in order that $\gamma > 0$, we have the requirement;

$$\pi^{-(1/2)} \cdot \lambda^{-(2/3)} < 1$$

or,

$$\lambda > \pi^{-(3/4)} \tag{3.69}$$

This indicates that the plasma inhomogeneity (characterized by the phase mis-match gradient, k') must not be too large.

In the absence of any inhomogeneity and with weak damping of the scattered e-m wave (so that $\gamma_3/v_3 >> \gamma_2/v_2$), then the growth equation will be proportional to $[2\gamma_0 (v_2 v_3)^{-(1/2)} - \gamma_3/v_3]$. This gives a second threshold condition;

$$\gamma_3/v_3 < 2\gamma_0/(v_2 v_3)^{(1/2)}$$

or,

$$\gamma_3 < 2\gamma_0 (v_3/v_2)^{(1/2)} \tag{3.70}$$

These two threshold conditions lead, separately, to minimum values of the incident laser intensity required to drive the absolute instability. The remainder of this section will involve calculations which will lead to estimates of these threshold levels. These estimates will be compared, in later chapters, with the experimentally observed threshold levels.

In determining estimates for the threshold laser intensity, the following expressions will be used:

The plasma frequency,

$$\omega_p=5.65\cdot 10^4\sqrt{(n_e)}\ \text{sec}^{-1}$$

The Debye length,

$$\lambda_d=7.43\cdot 10^2\sqrt{(T_e/n_e)}\ \text{cm}$$

The electron thermal velocity,

$$v_t=5.9\cdot 10^7\sqrt{T_e}\ \text{cm/sec}$$

And the wavenumbers (scalar values),

$$(k_1)^2=(1/c^2)\{\omega_1^2-\omega_p^2\}=(\omega_1/c)^2\{1-(n/n_0)\}$$

$$(k_2)^2=(1/c^2)\{\omega_2^2-\omega_p^2\}\simeq(\omega_1/c)^2\{1-2\sqrt{(n/n_0)}\}$$

$$(k_3)^2=(2/3v^2)\{\omega_3^2-\omega_p^2\}=(k_1+k_2)^2$$

where, n_0=critical density

For a CO_2 laser,

$$\omega_1=1.777\cdot 10^{14}\ \text{sec}^{-1}$$

And setting,

$$n_e=2.5\cdot 10^{17}\ \text{cm}^{-3}\quad \text{and}\ T_e=45\ \text{eV}$$

Then,

$$\omega_p=2.825\cdot 10^{13}\ \text{sec}^{-1}$$

$$\lambda_d=9.97\cdot 10^{-4}\ \text{cm}$$

$v_t=3.96\cdot 10^8$ cm/sec

$v_0=2.72\cdot 10^2\sqrt{I}$ cm/sec

and $n/n_0=.025$

So that,

$k_1=5.85\cdot 10^3$ cm^{-1}

$k_2=4.90\cdot 10^3$ cm^{-1}

$k_3=1.08\cdot 10^4$ cm^{-1}

and,

$\omega_3=2.83\cdot 10^{13}$ sec^{-1}

$\omega_2=1.49\cdot 10^{14}$ sec^{-1}

From the inhomogeneity condition, equation (3.69), the threshold is given by,

$$\lambda = \gamma_0^2/(k'v_2v_3) = \pi^{-3/4} \qquad (3.71)$$

Expressions for k', v_2, v_3, and γ_0 must be obtained. The wavenumbers are given by,

$dk_1/dx = -(\omega_x/k_1c^2)\cdot d\omega_x/dt$

$dk_2/dx = -(\omega_x/k_2c^2)\cdot d\omega_x/dt$

and $dk_3/dx = -(2\omega_x/3k_3v_t^2)\cdot d\omega_x/dt$

where ω_x is the plasma frequency at a position x along the solenoid.

Clearly, $k'_3 >> k'_{1,2}$ and one may set $k'\simeq k'_3$.

With a linear density gradient, the density at a position x along the solenoid is given by,

$n_x = n(1 + x/L)$,

where L is the density scale length.

Then, by definition,

$\omega_x = [\omega_p^2(1 + x/L)]^{1/2}$

so,

$$d\omega_x/dx = (1/2\omega_x)\cdot(\omega_p^2/L)$$

and substituting into the expression for k_3'

$$k' = \omega_p^2/(3k_3 v_t^2 L) = 1.57\cdot 10^5/L . \qquad (3.72)$$

From the definition of γ_0 (equation 3.68),

$$
\begin{aligned}
(\gamma_0)^2 &= (k_3)^2\{\omega_p/(\omega_1 - \omega_p)\}\cdot(v_0)^2/8 \\
&= 2.76\cdot 10^6\cdot v_0^2 \\
&= 2.04\cdot 10^{11}\cdot I \qquad |I|=|\text{watts/cm}^2| . \qquad (3.73)
\end{aligned}
$$

The velocities $v_{2,3}$ are given by,

$$v_2 \simeq 3\cdot 10^{10}\ \text{cm/sec}$$

$$v_3 = d\omega_3/dk_3 = (3/2)\cdot(v_t^2 k_3/\omega_3) = 8.98\cdot 10^7\ \text{cm/sec} .$$

Using these values and substituting equations (3.72) and (3.73) into equation (3.71), the threshold intensity is given by,

$$I=\pi^{-(3/4)}\cdot(1.57\cdot 10^5/L)\cdot(3\cdot 10^{10})\cdot(8.98\cdot 10^7)/(2.04\cdot 10^{11}).$$

Taking a density scale length of 20 cm,

$$I = 4.4\cdot 10^{10}\ \text{W/cm}^2 \qquad (3.74)$$

Similarly, a threshold intensity can be obtained from the damping condition. From equation (3.70), the threshold is given by,

$$
\begin{aligned}
\gamma_0 &= (\gamma_3/2)\cdot\sqrt{(v_2/v_3)} \\
&= 9.14\cdot\gamma_3 . \qquad (3.75)
\end{aligned}
$$

Taking γ_3 as the electron-ion collisional damping then,

$$\gamma_3 = 3\cdot 10^{-6} n_e \cdot \ln\Lambda / T_e^{(3/2)} = 7.5\cdot 10^{12}/T_e^{(3/2)}$$

where $\ln\Lambda$, the collisional Coulomb logarithm, has been set to 9.0.

Substituting into equation (3.75),

$$(\gamma_0)^2 = 4.7\cdot 10^{26}/T_e^3 .$$

From equation (3.73),

$$(\gamma_0)^2 = 2.04\cdot 10^{11}\cdot I .$$

Equating these expressions and using the above relation for the quiver velocity then the threshold intensity is given by,

$$I=2.304\cdot 10^{15}/T^3. \qquad (3.76)$$

The ambient electron temperature is affected by the transient heating prior to the SRS process. During this period (experimentally found to be ~5 nsec) there is no time for the electrons to transfer energy and the change in energy is entirely due to inverse bremsstrahlung absorption.

The change in electron energy, ϵ, is,

$$d\epsilon/dt = (3/2)nk\cdot dT_e/dt = KI \qquad (3.77)$$

where K=the inverse bremsstrahlung absorption coefficient. From equation (3.15),

$$K = 7\cdot 10^{-35}\cdot n^2/T_e^{(3/2)}$$

where $|T_e| = |ev|$.

Substituting this expression into equation (3.77) and setting the units so that $|T|=|ev|$ and $|I|=|W/cm^2|$,

$$T_e^{(3/2)}dT = \{(2/3)\cdot 7\cdot 10^{-35}\cdot n\cdot(10^7/1.6\cdot 10^{-12})\cdot I\}dt .$$

Setting $n = 2.5\cdot 10^{17} cm^{-3}$, then integration gives,

$$(T_e^{(5/2)} - T_0^{(5/2)}) = (182.5 \cdot I) \cdot \tau$$

where T_0=the initial electron temperature.

Taking T_0=45 eV and setting $I=5 \cdot 10^{10}$ W/cm^2 and with τ=5 nsec, then the electron temperature is calculated to be T_e=81 eV. Using this value in equation (3.76) gives the self-consistent value for the threshold intensity,

$$I \simeq 4.5 \cdot 10^{10} \text{ W/cm}^2 \qquad (3.78)$$

From either threshold condition, then, the SRS process is expected to onset for laser intensities in the range $4 - 5 \cdot 10^{10}$ W/cm^2, well within the experimental values.

The question of saturation mechanisms for the SRS instability will be dealt with in terms of the experimental results, in Chapter 4.

CHAPTER IV

Experimental Results and Observations

4.1 Preliminary Remarks

The results of several experiments using the laser-heated solenoid apparatus are presented in this chapter. These results are analyzed and discussed in light of the theoretical background presented in Chapter 3.

The experiments were directed toward characterizing the axial and radial development of the plasma column, determining the plasma density and temperature, and investigating the nature of the stimulated scattering processes.

During the course of the study, several different experimental arrangements were used. Stable and unstable resonator optics were used in the laser cavity. To direct the laser into the solenoid both f/5 and f/15 focussing systems were used. Finally, both split-coil and single-coil solenoids were used to confine the plasma. These components have been described in Chapter 2.

Many results depended on the experimental arrangement. Changing the focussing ratio of the incoming laser produced particularly significant effects. The conditions under which the data were obtained is specified throughout.

Variations in the laser energy, hydrogen fill density, and confining magnetic field strength led to a wide range of experimental conditions. Input laser energies ranged from

~150-~500 joules, hydrogen fill pressures from ~5-~30 torr and magnetic field strengths from 0-~70 kG.

The basic experimental procedures and the diagnostic techniques employed were detailed in Chapter 2.

4.2 Axial Development

The axial formation of the plasma column was determined entirely through the analysis of axial streak photographs. Examples of streak photographs are given in Figure 4.1.

The spatial and temporal calibration of the streak photographs are easily determined. Spatially, the distance between the lines on the photograph are directly related to the distances between the solenoid windows. Temporally, calibration was achieved by systematically varying the timing between a 30 nsec ruby-laser pulse and the triggering of the streak camera. The distance from the location of the ruby light on the streak photograph to the base of the photograph was measured. Plotting this distance versus the known time delay gave the appropriate calibration curve.

4.2.1 Results and Analysis

From a bleaching wave model, the location of the axial front depends on the laser intensity, the plasma density and time according to,

$$L \propto I^{(3/5)} \cdot t^{(3/5)} / N^{(7/5)}$$

In analyzing the axial streak data, these dependencies will be examined.

AXIAL STREAK PHOTOGRAPHS

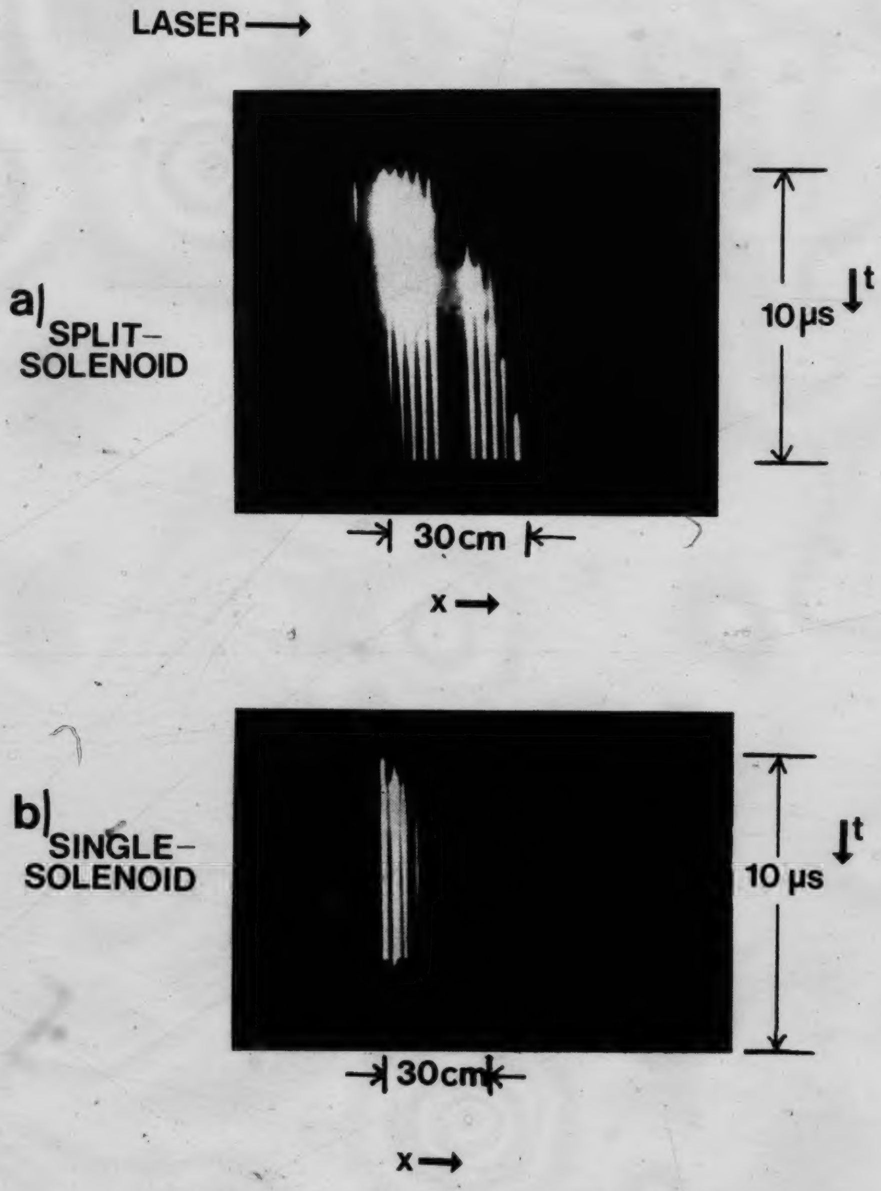
LASER ⟶
a) SPLIT-SOLENOID
10 μs
t
30 cm
x ⟶
b) SINGLE-SOLENOID
10 μs
t
30 cm
x ⟶

Figure 4.1 Axial Streak Photographs:
a) Split Solenoid (f/5 focus)
b)Single Solenoid (f/15 focus)

Axial streak photographs were taken with both split-coil and single-coil solenoids. Since the observation ports on the split-coil solenoid are closer together, data from this device are more appropriate for use in determining the location of the front and thus, its temporal dependence.

Twenty streak photographs were used in the temporal analysis of the front. These photographs were digitized, a cubic spline interpolating polynomial was generated, and the result was plotted. Results for 7 of the longer columns are shown in Figure 4.2. The error in the y-direction is ± .5 cm and in the x-direction it is ± .1 μsec.

Some general observations may be made concerning the axial behaviour of the column. During any particular shot, the axial velocity is initially fairly rapid and slows with time as the energy input decreases. The column, however, continues to develop even after the laser energy has depleted ($t>2\mu sec$).

For early times, $t<1\mu sec$, the column development was uniform enough so that a velocity value could be determined. Under varying conditions of fill pressure and laser energy, these values ranged from 3.90 ± .2 cm/μsec to 14.1 ± .3 cm/μsec. For typical experimental values ($p=16$ torr, $E=300$ joules) a velocity of 6.9 ± .3 cm/μsec was recorded. During very late times, $t>3.5\mu sec$, the velocity is also fairly uniform. During this period, the velocity ranged from .98 ± .04 cm/μsec to 2.3 ± .1 cm/μsec.

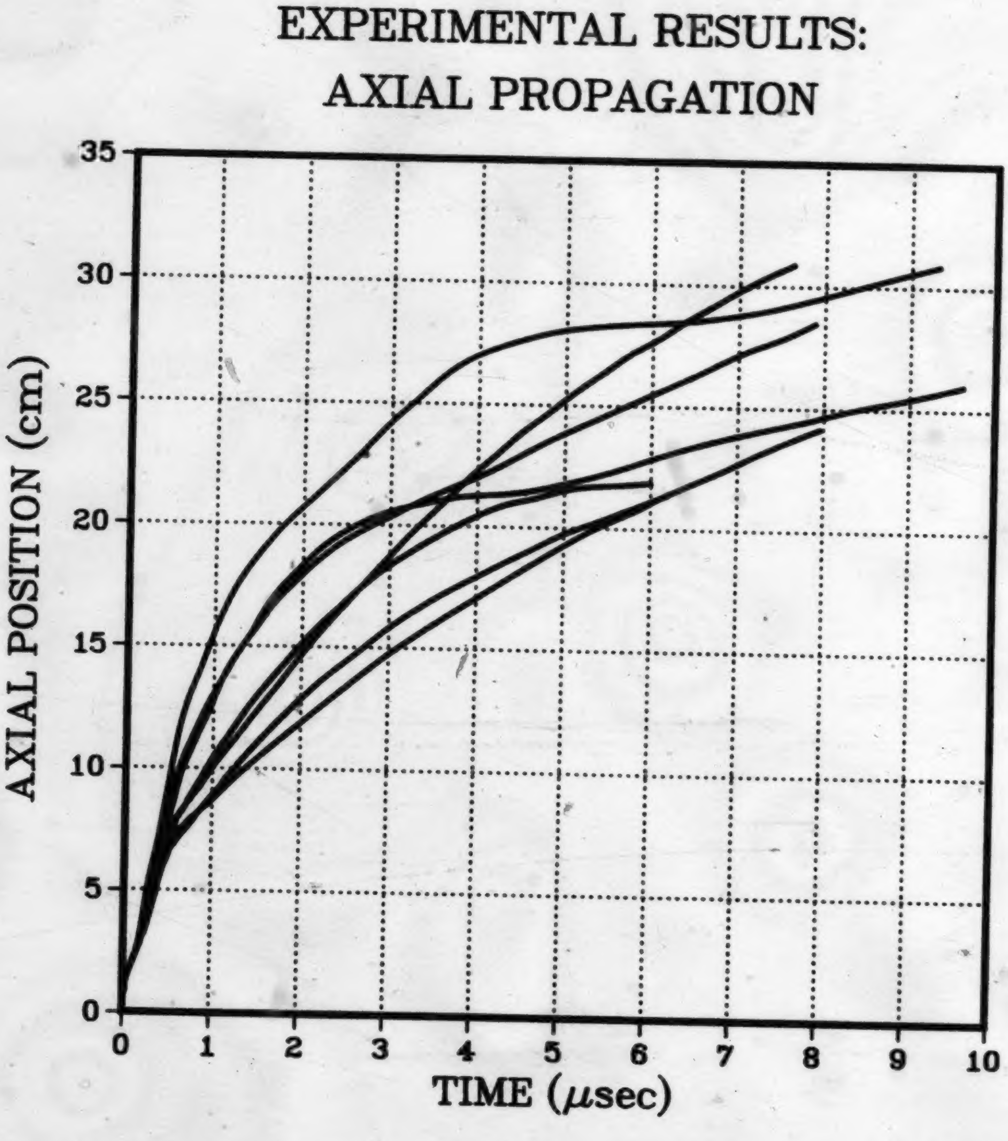

Figure 4.2 Axial Propagation of the Plasma Column: Fill Pressures from 7-25 Torr, Laser Energies from 300-500 Joules

In order to determine the power dependence of the axial position of the column with time, a log-log plot was made. The plot (for the same data given in Figure 4.2) is given in Figure 4.3. For the time period during which laser influences are possible ($t<2\mu\text{sec}$), a slope of .66 ± .15 was obtained for the best fit line through the data. The temporal dependence is given, then, by

$$L \propto t^{.66}$$

This is in reasonable agreement with a bleaching wave model which predicts a power of .6 in time.

The dependence of the axial velocity on laser intensity and plasma density was examined. In this regard, 15 axial streaks were analyzed. The data set selection was based on the quality of the streak photograph and the reliability of the supporting hydrogen fill pressure and laser energy data. This data was taken primarily with the single-coil solenoid and unstable resonator laser optics. Both f/5 and f/15 focussing optics were used.

While a wide range of values for the laser energy, E, and the hydrogen fill pressure, p, exist in this data set, the set is small and does not lend itself to a detailed analysis of the power dependence of these parameters. Instead, the bleaching model was tested by first estimating the velocity over the first μsec and plotting this value against $E^{(3/5)}/p^{(7/5)}$. This plot is given in Figure 4.4.

Although the data set is small, the linear fit is very good. The coefficient of correlation is .92. A bleaching

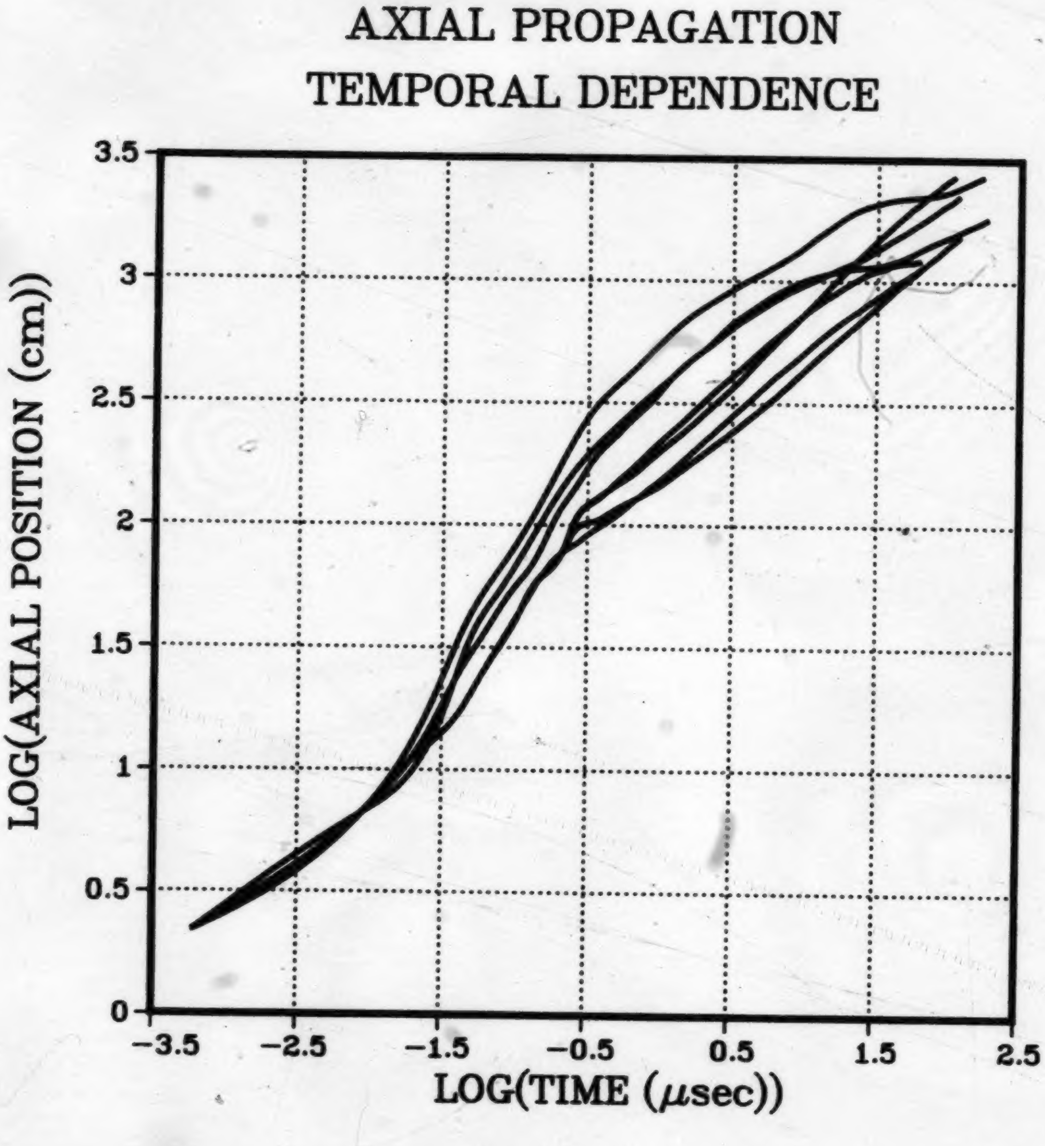

Figure 4.3 Temporal Dependence of the Axial Propagation of the Plasma Front:
Experimental Parameters as in Figure 4.2

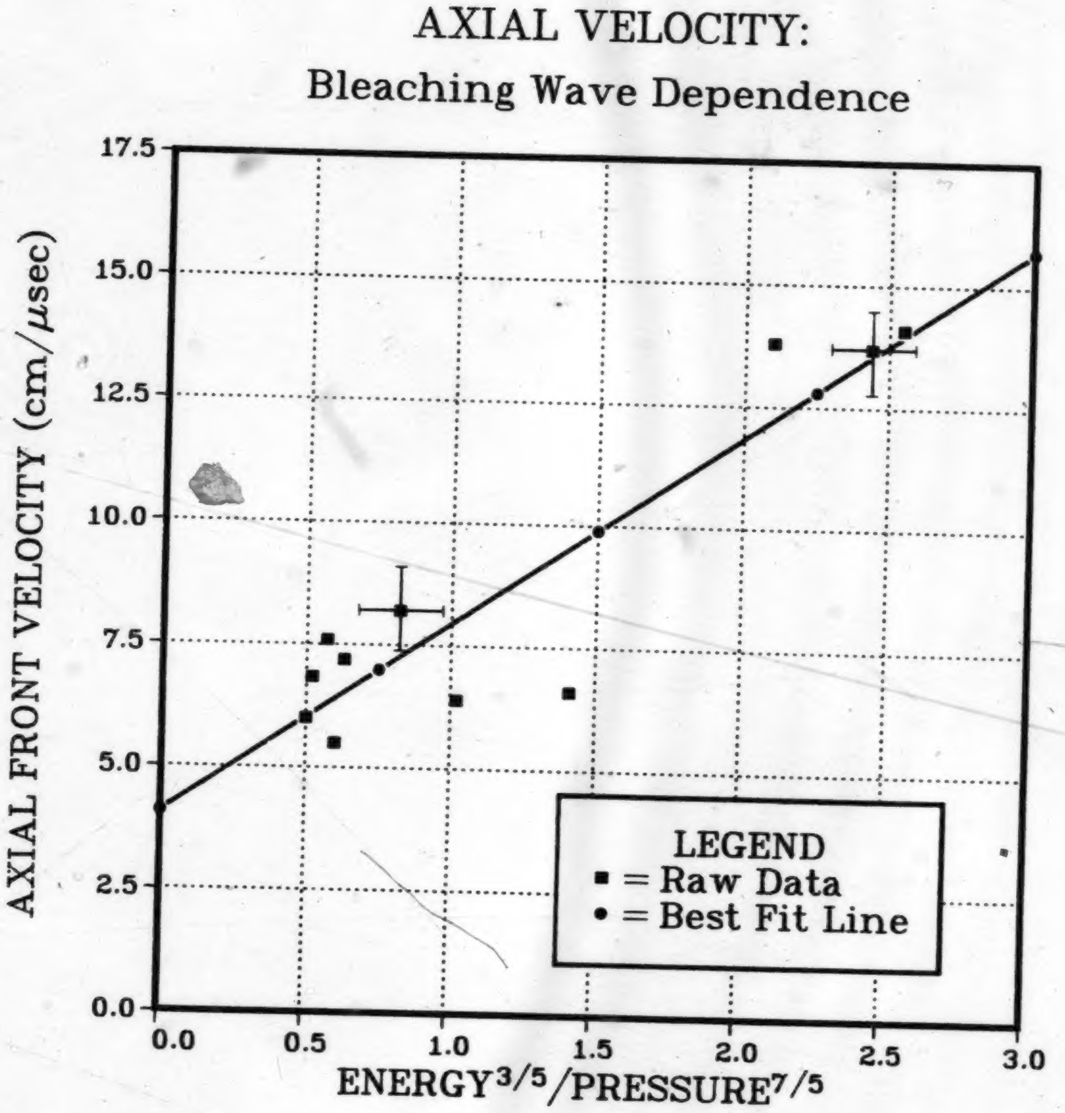

Figure 4.4 Axial Velocity of Plasma Front vs Laser Intensity and Hydrogen Fill Pressure

wave model would appear, then, to be well supported.

As derived in Chapter 3, the position of the bleaching front is given by,

$$L = K \cdot I^{(3/5)} t^{(3/5)} / n^{(7/5)}$$

where for,

$$\alpha >> 1, \ K = 9.2 \cdot 10^{24} \qquad \text{(Rehm, 1971)}$$

and for,

$$\alpha \simeq 1, \ K = 3.8 \cdot 10^{24} \qquad \text{(Burnett and Offenberger, 1975)}$$

An estimate of the constant K in the above expression can be determined from the streak data if estimates of the laser intensity and the plasma density are made from the known laser input power and the hydrogen fill pressure.

Assuming that the hydrogen is fully ionized and taking the ratio of the fill density to the on-axis density to be $n_0/n=2$, then the plasma density on axis is given by,

$$n = (6.6 \cdot 10^{16} \cdot p)/2 \ \text{cm}^{-3} \qquad |p| = |\text{torr}|$$

The laser intensity may be estimated from the equation,

$$I = (P/\pi R^2) \cdot [1 - \exp(-kL)]$$

where P=laser power

and $kL \simeq .6$

giving,

$$I \simeq P/2\pi R^2$$

The plasma radius, R, used in this expression was obtained from radial density profiles taken under similar experimental conditions.

Using these expressions, the constant K was determined from the axial streak data. Averaging over the data set a value of $K = (4.74 \pm 2.40) \cdot 10^{24}$ was obtained.

Although there is a large error associated with this value, it is in very good agreement with that predicted by Burnett and Offenberger(1975).

4.3 Radial Behaviour

The radial behaviour of the plasma was determined through the analysis of radial streak photographs and radial density profiles.

4.3.1 Radial Streak Photography

Examples of radial streak photographs taken from the single-coil solenoid are given in Figure 4.5.

Some observations can be made directly from these photographs. The initial breakdown is apparent. During this initial phase the illumination is fairly uniform. The expansion following breakdown is rapid and symmetric. While the edges remain luminous, the core often stops radiating or else radiates in a non-uniform manner. The temperature and density of the plasma are difficult to determine from its luminescence but something may be said about its uniformity. With time, the plasma column expands out to a reasonably constant radius.

The radial streak photographs were spatially calibrated by photographing a resolution screen placed along the axis of the solenoid. The temporal calibration was the same as for the axial streak photographs.

RADIAL STREAK PHOTOGRAPHS

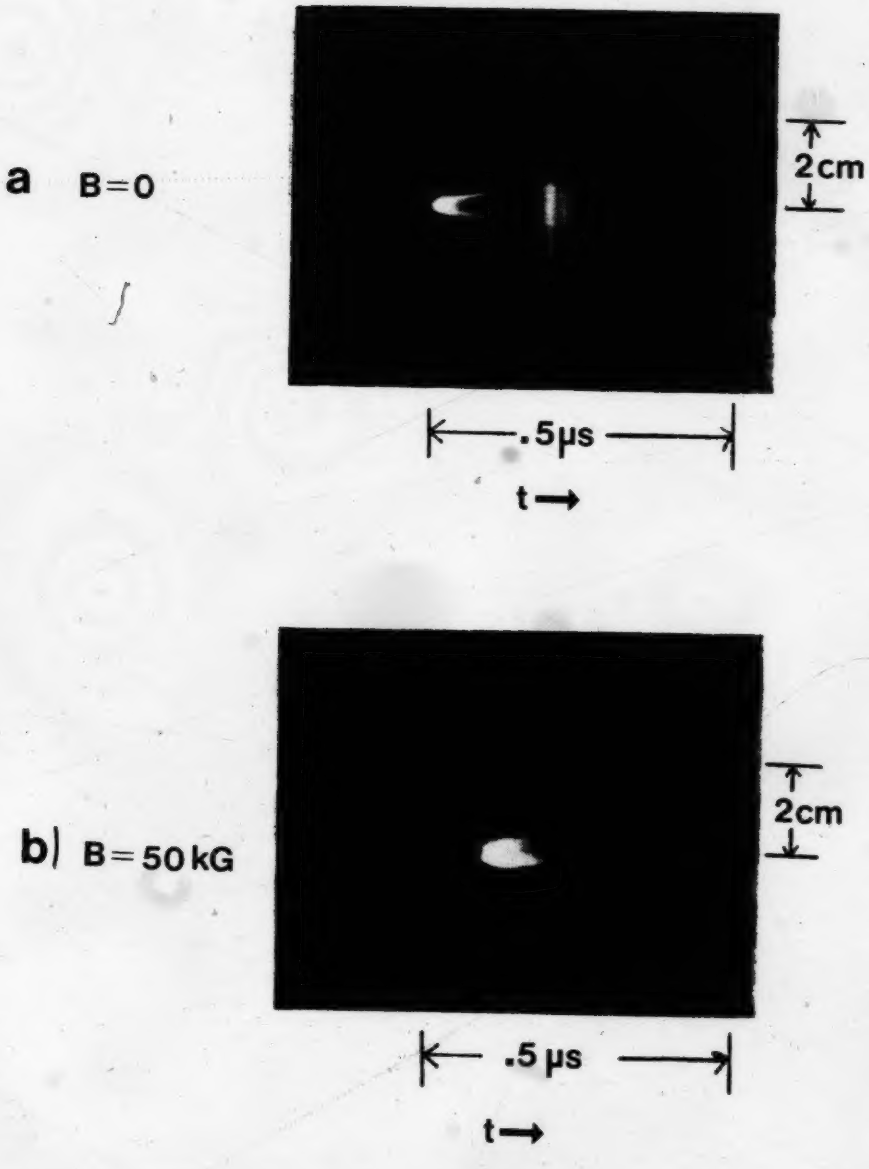
a B=0
2cm
.5µs
t→
b) B=50kG
2cm
.5µs
t→

Figure 4.5 Radial Streak Photographs
(Single Solenoid-f/15 focus)

4.3.1.1 Results and Analysis

The radial expansion of the plasma column will be affected by the magnitude of the confining magnetic field, the plasma density and the plasma temperature. Using the ion transport model presented in Chapter 3, the effects of these parameters can be anticipated. Increased magnetic field, increased density and decreased temperature should all result in reduced expansion.

Other experimental variables may also alter the radial behaviour. In or near the focal region, the focal spot size and the f/ratio may well affect the radial expansion rates. As mentioned in Chapter 2, two different focussing systems were used in this study. The f/5, off-axis parabola system resulted in a ~385 μm spot size while the f/15 Cassegrain focussing system resulted in a ~300 μm spot size.

A final consideration in the analysis of the radial streak photographs is the film exposure. Unlike axial streaks where the spatial location is well defined, the location on a radial streak photograph may be misinterpreted due to variations in the exposure of the film.

The data set used in the analysis of the radial behaviour consisted of 16 radial streaks. These were taken from a much larger set and selected according to the availability of supporting data and the quality of the exposure. The photographs were digitized, cubic spline interpolating polynomials generated and the results plotted.

All data were taken with the single-coil solenoid. Eleven shots were taken using the f/15 focussing system and the remainder with the f/5 system. All data from the f/15 system were taken at axial locations which were 4.5 cm from the focus. The data from the f/5 system were taken either 1.0 or 3.0 cm from the focus.

Within each of these data sets, shots were taken with and without an applied magnetic field. Although shot-to-shot variations in hydrogen fill pressure and laser energy occurred, the data were insufficient to draw any conclusions with respect to the dependence of the radial dynamics on these parameters.

Figure 4.6 gives examples of the radial position in time with and without magnetic field for both the f/5 and f/15 focussing systems.

Though not particularly dramatic, the confining effect of the magnetic field is demonstrated. The ion transport model, discussed in Chapter 3, showed that for densities typical of those used in this study the effect of the magnetic field is not particularly strong.

Included in Figure 4.6 are curves generated from the ion transport model. While it must be noted that this a very simple model and does not account for any effects of the laser beam propagation, the general behaviour, particularly for data taken with f/15 focussing, is reasonably well described. In fact, the data given in Figure 4.6 demonstrate that there is a very significant change in the radial

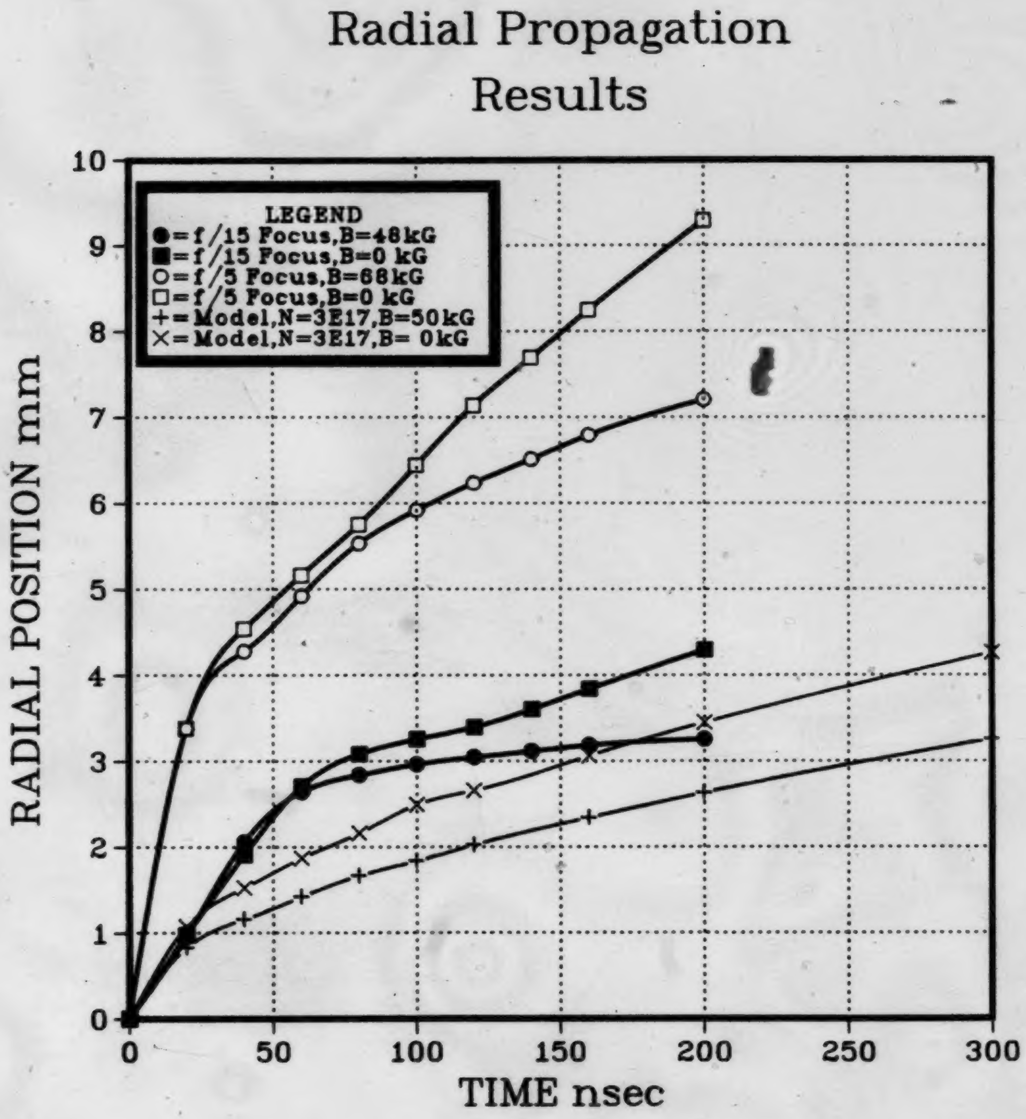

Figure 4.6 Radial Propagation of the Plasma Column

expansion from one laser focussing system to the other.

Taken over the first 50 nsec, the average velocity for data taken with the f/15 focussing system is 4.5 ± 1.2 cm/μsec. For data taken with the f/5 focussing system, the average radial velocity was 9.0 ± 1.5 cm/μsec, twice the value obtained from the other system.

The expansion rate (taken with full B-field) at later times (100 - 200 nsec) showed a less significant dependence on the focussing system. With f/15 focussing, the measured velocity was .82 ± .3 cm/μsec while with f/5 focussing it was 1.2 ± .4 cm/μsec.

The results of these expansion rate measurements indicates a strong influence of the laser focussing system during the initial phase of the radial expansion of the plasma column. It should be noted that the data were only taken at axial locations within 4.5 cm of the laser focus and the discussion must be restricted to this region.

The faster focussing-defocussing of the f/5 system may be expected to result in an initially larger breakdown region and subsequent stronger heating in outer regions of the plasma column. This would then result in more rapid radial expansion. The reduced laser intensity and subsequent reduction of the overall plasma temperature would complicate this argument. Incorporation of the laser effects in the simple ion transport model would be difficult, however, the results of the 2-D simulation, which includes laser propagation effects supports these observations extremely well.

Further discussion of this effect and comparisons with the 2-D simulation will be given in the following chapter.

4.3.2 Radial Density Profiles

The shifting of fringes in an interferogram identifies the location of the plasma column. The use of interferometric methods was described in Chapter 2.

Examples of interferograms are given in Figure 4.7. A few observations may be made directly from these raw data. Figure 4.7-a shows an interferogram taken without a plasma column present. The fringes are straight and uniformly spaced.

Figure 4.7-b shows an interferogram taken near the breakdown front. The expansion of the plasma column behind the front is clearly visible.

Figure 4.7-c shows an interferogram taken well after the passage of the front. A wider, slowly expanding, plasma column is now apparent.

A radial density profile is obtained from the interferogram by performing an Abel inversion on the fringe shift data. This procedure assumes cylindrical symmetry which is generally expected and, indeed, observed. If the symmetry is not present then, by assuming the asymmetry to be entirely along the axis of the probing radiation, an asymmetric Abel inversion can be performed and the density profile can be generated.

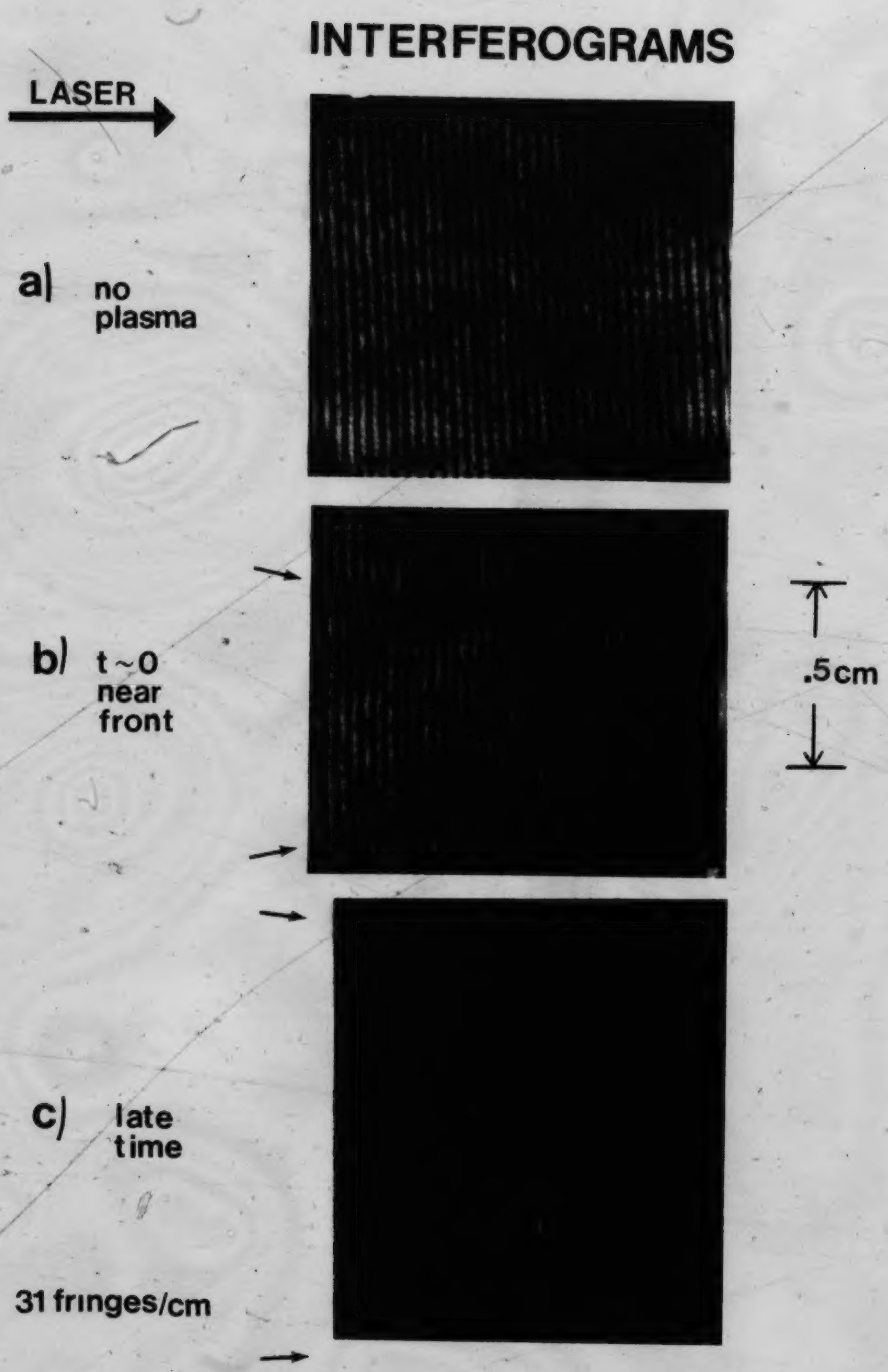
INTERFEROGRAMS
LASER
a) no plasma
b) t~0 near front
.5cm
c) late time
31 fringes/cm

Figure 4.7 Interferograms (Single Solenoid-f/5 focus):
a) no plasma, b) plasma front, c) plasma column
(arrows indicate location of fringe shifts)

If perturbations are observed on an already shifted fringe then the fringe may be inverted differentially. This is done by separately inverting the background fringe (ignoring the perturbed region) and the perturbed region of the fringe (using the shifted fringe as a baseline). The two inversions are then added together to give the complete density profile.

The spatial calibration of the interferograms was obtained by photographing a resolution screen placed along the axis of the solenoid. Axially the interferogram extends over ~1 cm of the column length. Each individual fringe, then, represents a different axial location. By estimating a propagation velocity for the front, axial variations may be treated as temporal effects.

The timing between the ruby pulse, used in taking the interferogram, and the breakdown front of the plasma column was determined by feeding a small amount of the ruby light through an optical fibre into the radial streak camera. The streak camera then recorded the relative positions of the ruby light and the breakdown front. In cases where this method failed, the timing was determined from the signals used to monitor the ruby and the CO_2 lasers.

Interferometry was used with both f/5 and f/15 focussing systems. Shots taken with the f/15 system were all taken at an axial location which was 4.5 cm from the focal region. With f/5 focussing, shots were taken at axial positions 1.0, 3.0, and 10.0 cm from the focal region.

In total, 19 interferograms were analyzed. These were taken from a much larger data set. The selection was based on the quality of the interferogram, the timing with respect to the breakdown front, and the quality of the supporting data. Of the 19 interferograms, 8 were taken with the f/15 focussing system and the rest with f/5.

In each interferogram a number of fringes were inverted. Fringes to be inverted were first digitized. A smoothing cubic spline was then generated. The smoothing factor was carefully chosen to reflect the error in the digitization process. The smoothed fringe was then inverted by an appropriate Abel inversion method.

Density profiles are very useful in characterizing several features of the plasma column. These include the formation of a density minimum on axis, the ratio of the density maximum to minimum, the uniformity and symmetry of the column, and a precise measure of the radial extent of the plasma. Figure 4.8 shows an example of an interferometric fringe and the associated density profile. The symmetry of the fringe, the density minimum on axis, and the radial extent of the plasma column are all clearly displayed.

Density profiles are also useful in showing the temporal development of the plasma column near the breakdown front. Of the 19 interferograms analyzed, 12 were taken very near the breakdown front. Five cases actually included the front. Of these five, 2 were taken with f/15 focussing and 3

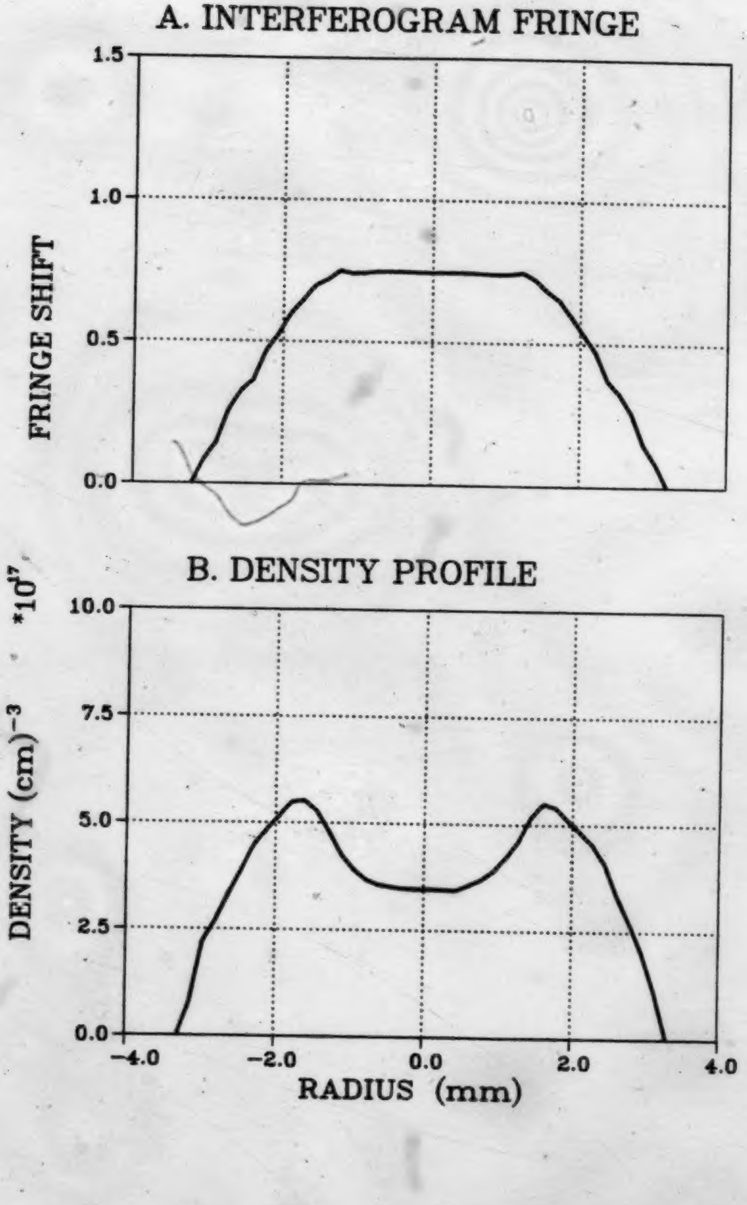

Figure 4.8 Late-time Interferogram Fringe and Density Profile, 4.5 cm from the focal region using f/15 focussing

with f/5 focussing. Examples of density profiles taken just behind the breakdown front are given in Figures 4.9 and 4.10.

Figure 4.9 shows data from an interferogram taken 4.5 cm from the focal region, using the f/15 focussing system. The position of the profile in Figure 4.9-a is nearest the front while the one in Figure 4.9-c is furthest from it. The axial distance between profiles is ~840 μm and the profile in Figure 4.9-a is ~840μm behind the front.

From Figure 4.9-a it is clear that a density minimum on axis is rapidly established. By estimating the axial propagation velocity as 7 cm/μsec, the time, t_m, required to form this density minimum can be estimated. A value of $t_m \simeq 12$ nsec is obtained. The formation of the density minimum on axis is important in order that the laser energy be trapped in the plasma.

The hydrogen fill pressure for the data given in Figure 4.9 was 20 torr. If fully ionized, this corresponds to an electron density of $1.3 \cdot 10^{18} \mathrm{cm}^{-3}$. From Figure 4.9, density values corresponding to full ionization were not reached until ~24 nsec following the initial breakdown. In Chapter 3 calculations were made showing that the time required for full ionization would be expected to lie in the range of 5-35 nsec. The measured value of 24 nsec is in good agreement with these calculations.

A shot (not shown), taken under similar conditions, produced the same results with regards to the ionization

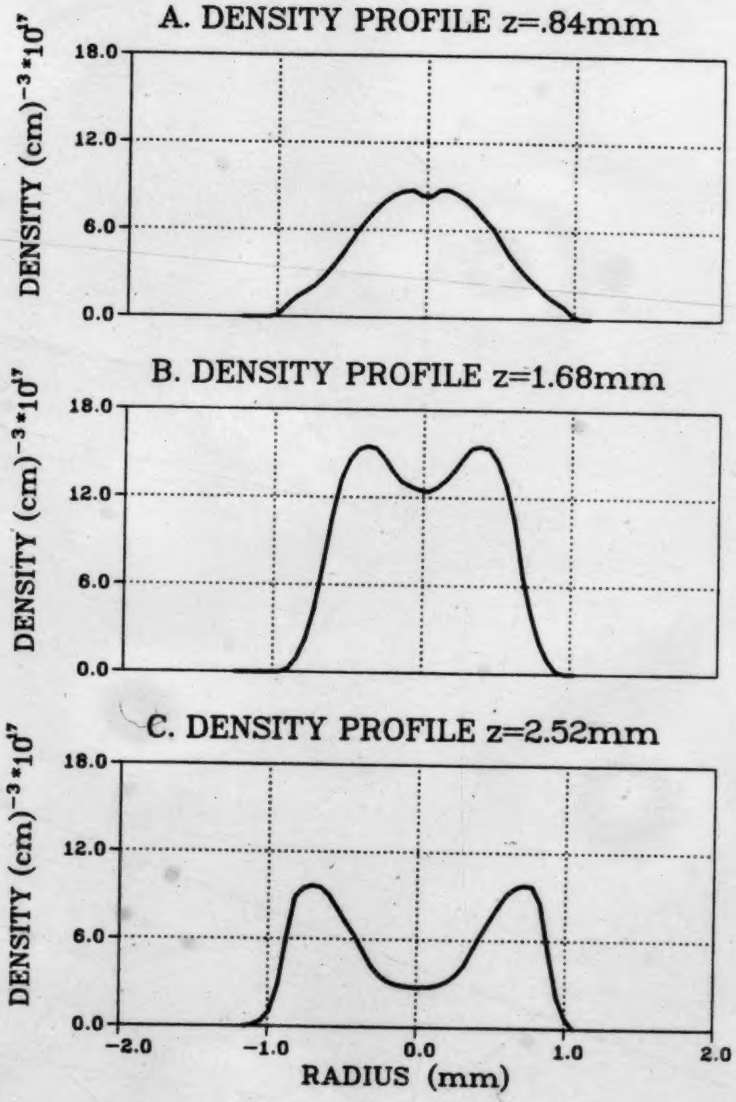

Figure 4.9 Density Profile Sequence at the Breakdown Front, 4.5 cm from the focal region, using f/15 focussing: z=the distance from the front

time and the time required to produce a density minimum on axis.

The radial expansion rate for early times can also be obtained from the interferogram. From the interferogram used to produce the density profiles given in Figure 4.9, the radial expansion rate over the first ~40 nsec was determined to be 4.2 cm/μsec. This value is consistent with the average radial velocity of 4.5 ± 1.2 cm/μsec obtained by radial streak analysis of data taken under the same conditions.

Figure 4.10 shows a sequence of density profiles similar to that of Figure 4.9 but for data taken with the f/5 focussing system. The interferogram was taken 1 cm from the focal region. The axial distance between profiles is 3.5 mm and the first profile (Figure 4.20-a) is 1.4 mm from the breakdown front.

Again it is clear that a density minimum on axis is rapidly formed. The interferometrically measured formation time is $t_m \simeq 15$ nsec.

The fill pressure in this case was 17 torr corresponding, with full ionization, to an electron density of $1.1 \cdot 10^{18}$ cm^{-3}. Interferometrically, the density 15 nsec after breakdown is below this value and continues to drop as the plasma expands. If full ionization was achieved then it possibly occurred in a time <15 nsec. Other shots taken under similar conditions also indicate that either full ionization is not achieved or else the ionization time is <15 nsec. Blurring of fringes near the breakdown front makes

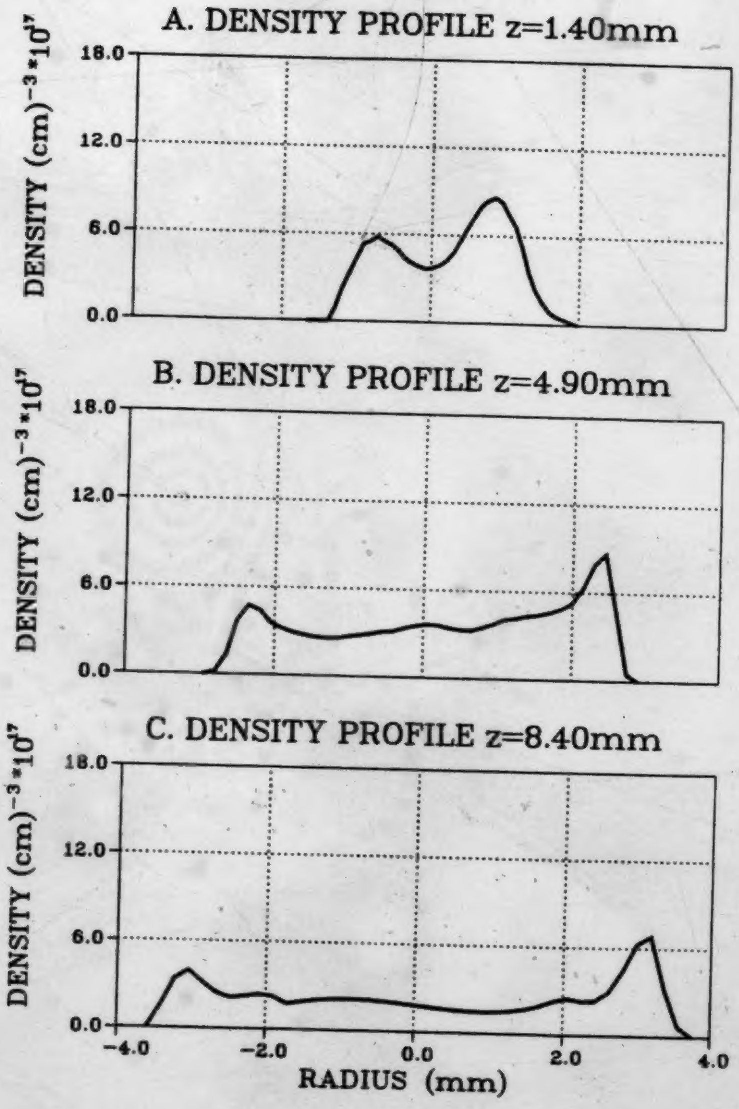

Figure 4.10 Density Profile Sequence at the Breakdown Front, 1.0 cm from the focal region, using f/5 focussing: z=the distance from the front

analysis, at times less than 15 nsec, uncertain.

From the interferogram used to produce the density profiles in Figure 4.10, the radial expansion rate during the first 50 nsec was determined to be 7.1 cm/μsec. While slightly lower than the average value of 9.1 ± 1.5 cm/μsec obtained from radial streak analysis, it is consistent with the observation that the early-time expansion rate with the f/5 focussing system is considerably greater than that with the f/15 focussing system.

For data taken with f/5 focussing and at axial positions near the focal region, perturbations frequently developed in the central regions of the fringes. An example of a fringe for which this occurs is given in Figure 4.11. In these cases the fringe is inverted differentially. The associated density profile for the fringe in Figure 4.11-a is given in Figure 4.11-b.

On the interferogram, these disturbances would initially appear on fringes a short distance (<.5 cm) behind the breakdown front. They were observed to grow over 2 or 3 fringes, remain constant over several fringes and finally vanish over a single fringe spacing. Assuming these effects to be related to the propagation of the front and assigning a propagation velocity of 7 cm/μsec then these disturbances can be characterized by a growth period of 20-30 nsec, a stable period of ~50 nsec, and very rapid decay <10 nsec. Spatially, scale sizes ranged from .1-.4 mm and densities were observed to reach 2 or 3 times the fill density.

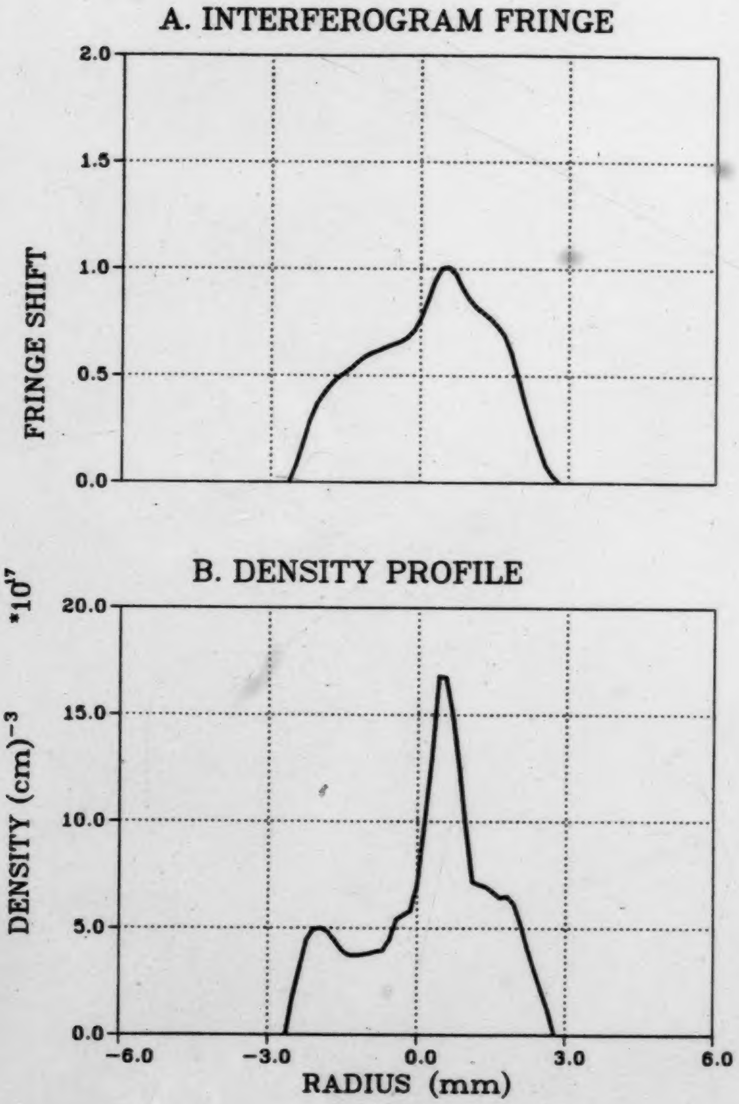

Figure 4.11 Perturbed Interferogram Fringe and Differentially Inverted Density Profile

These disturbances may reflect a density enhancement due to self-focussing effects or a type of density instability. It is important, however, to note that the Abel inversion of interferometric data is non-unique and other interpretations may be possible. Scudder(1979) showed that a fluted plasma column would produce fringes which are similar to that given in Figure 4.11-a.

Prior to discussing the late-time behaviour of the plasma column, data taken near the breakdown front but at a greater axial distance (10 cm) along the solenoid will be considered. Of the 3 shots analyzed at this location, 2 included the breakdown front.

Figure 4.12 shows density profiles for one such case. The time after breakdown for the profile given in Figure 4.12-a is estimated to be 16 nsec. The profile in Figure 4.12-b follows the first profile by ~32 nsec.

The fill pressure for this shot was 12 torr and full ionization ($8\cdot 10^{17}$cm^{-3}) has been achieved in a time, T_i<16 nsec. A density minimum on axis is observed to develop but not until a time ~48 nsec following the initial breakdown. Even then, the density minimum is very weak.

In the other case, shown in Figure 4.13, the fill pressure was 10 torr ($6.6\cdot 10^{17}$cm^{-3}). The first profile (Figure 4.13-a) is estimated to occur ~8 nsec after the initial breakdown. In this case, the density corresponding to full ionization has been exceeded indicating some density compression near the front. This is the only observation of

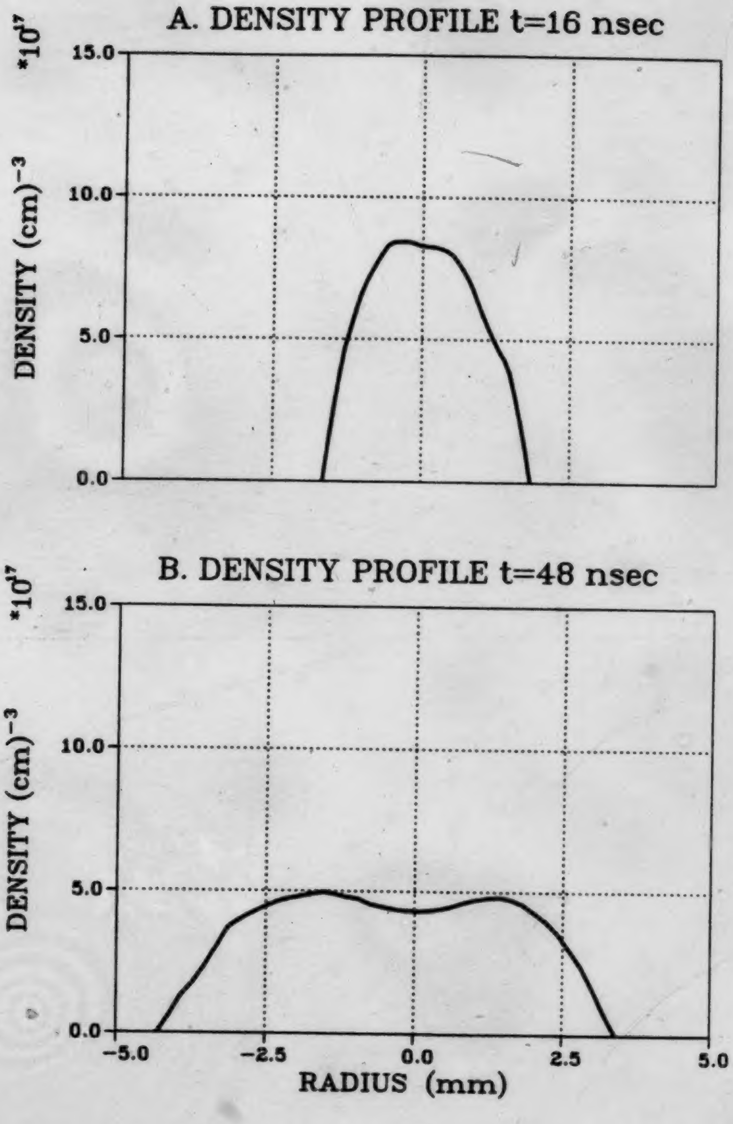

Figure 4.12 Density Profile Sequence at the Breakdown Front, 10.0 cm from the focal region, using f/5 focussing

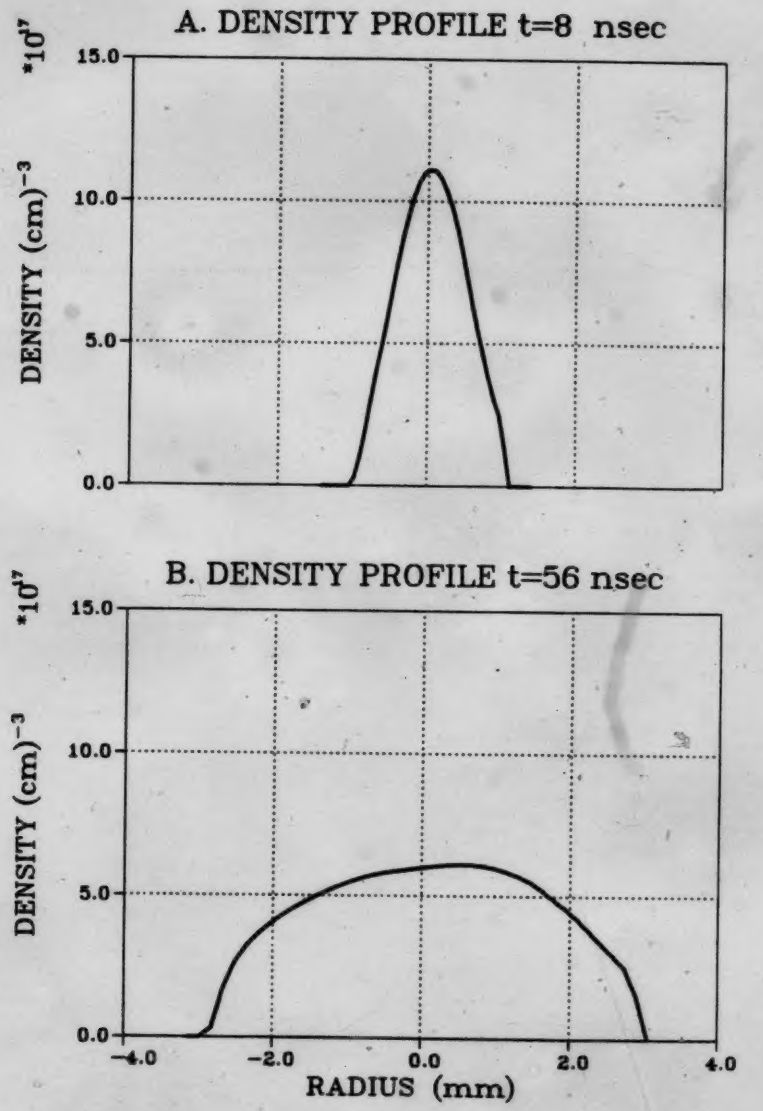

A. DENSITY PROFILE t=8 nsec

B. DENSITY PROFILE t=56 nsec

Figure 4.13 Density Profile Sequence at the Breakdown Front, 10.0 cm from the focal region, using f/5 focussing

such a compression and represents a 50% increase over the fill pressure.

Similar to the previous case, a density minimum on axis is not rapidly formed at this axial location. Indeed, no minimum is observed at times up to 56 nsec after the initial breakdown (Figure 4.13-b).

The formation of a density minimum on axis requires strong heating of the central region of the plasma column. From computer simulations, the laser beam is expected to become highly aberrated at axial locations several centimeters from the initial focal region. It is also clear that at positions farther along the axis the laser intensity will decrease due to absorption and other beam losses. For these reasons, the laser may not provide adequate heating of the core at this axial location and this may inhibit the formation of the density minimum.

An example of a late-time density profile was given in Figure 4.8. This profile was taken ~180 nsec following breakdown at an axial location 4.5 cm from the focal region. It was taken with an applied B-field of 42 kG and with the f/15 focussing system. The interferometrically measured plasma column radius is 2.8 ± .3 mm. This is just slightly less than the value of 3.2 mm obtained from radial streak analysis of data taken under similar conditions. This is expected since the radial streak shows the light emitting regions and depends on the exposure of the film which could result in radial values exceeding the plasma boundary.

For comparison, Figure 4.14 shows 2 density profiles from an interferogram taken with the f/5 focussing system. The shot was taken at an axial location 10 cm from the focal region, ~190 nsec following breakdown and with an applied B-field of 68 kG.

The interferometrically measured radius of the plasma column is 4.6 ± .3 mm. Again this is in good agreement with the value obtained from radial streak analysis. Furthermore, this result supports the observation that the f/5 focussing system yields a significantly larger plasma column.

While each interferogram shows only a limited axial region of the plasma column, the confining effect of the magnetic field can be seen. For a shot taken without an applied B-field (not shown), the column expands radially by ~.9 mm over an axial distance of .63 cm. With an applied field of 68 kG (Figure 4.14) the radial expansion was much reduced. The interferometrically measured value was ~.15 mm over an axial distance of .53 cm.

The presence of a density minimum on axis is again clearly demonstrated in the profiles shown in Figure 4.14. This effect was observed in virtually every interferogram analyzed.

In Chapter 3, the ratio of the peak density to the density minimum was calculated to be $n/n_0 \simeq 2.0$, based on frozen-field and pressure balance conditions. By considering the Nernst-Wienecke effects, the ratio was determined to be $n/n_0 \simeq 2.3$. Averaging over all fringes analyzed in which a

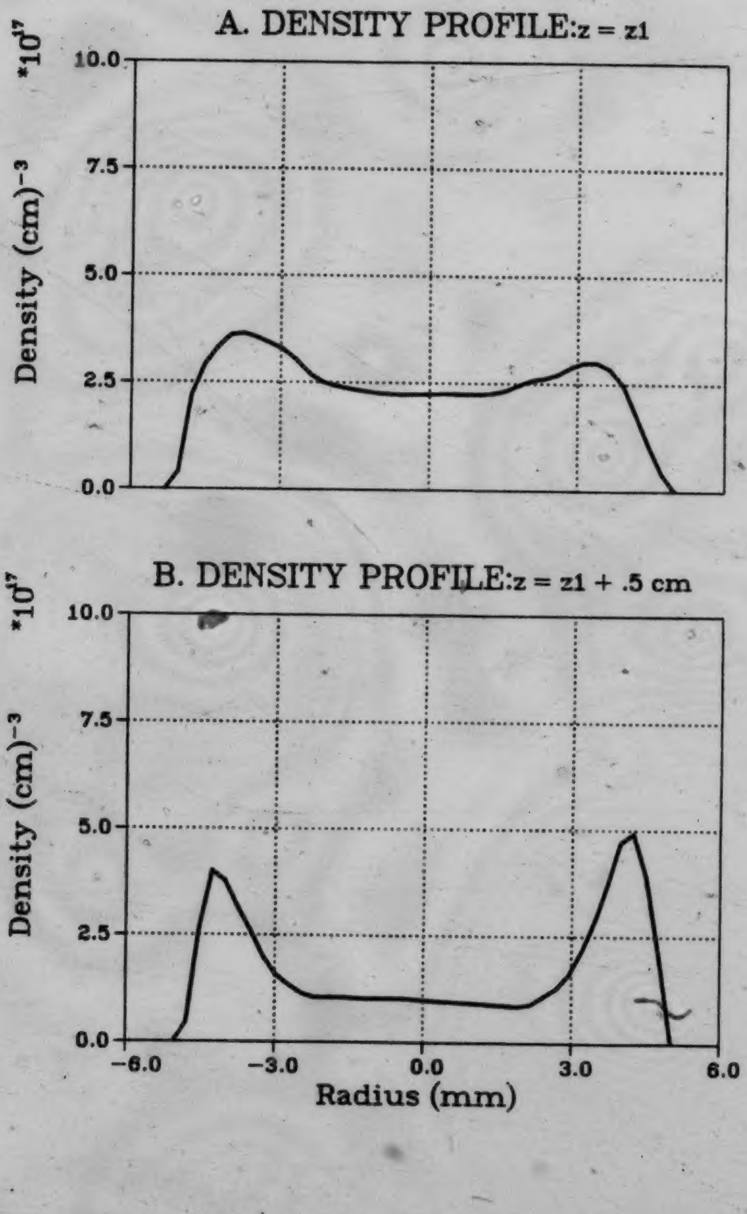

Figure 4.14 Late-time Interferogram Fringe and Density Profile, 10.0 cm from the focal region using f/5 focussing

density minimum was clearly established, the ratio of peak density to the density minimum was measured as 2.01 ± .56. This average included data from both early and late times and both f/5 and f/15 focussing systems.

The theoretical values are both dependent on the plasma temperature. In both cases, the value used in the calculation was 50 eV. Since the experimental value agrees very well with either calculation, this temperature should represent a good estimate of the average plasma temperature.

4.4 Stimulated Scattering

The results presented in this section were entirely obtained using the single-coil solenoid and the f/15 focussing system. Using f/5 input optics generated little or no scattering while with f/15 optics SBS was observed on virtually every shot. In fact, the focussing optics were deliberately distorted so as to degrade the focus, reduce the laser intensity and reduce the scattering level.

Details concerning the experimental methods used to collect these data have been given in Chapter 2.

4.4.1 Stimulated Brillouin Scattering, SBS

Figure 4.15 shows oscilloscope traces for 3 separate laser shots in which SBS was observed. In each case, the lower trace shows the SBS signal and the upper trace shows the corresponding input laser signal. For comparison, Figure 2.1 shows the laser signal without SBS present.

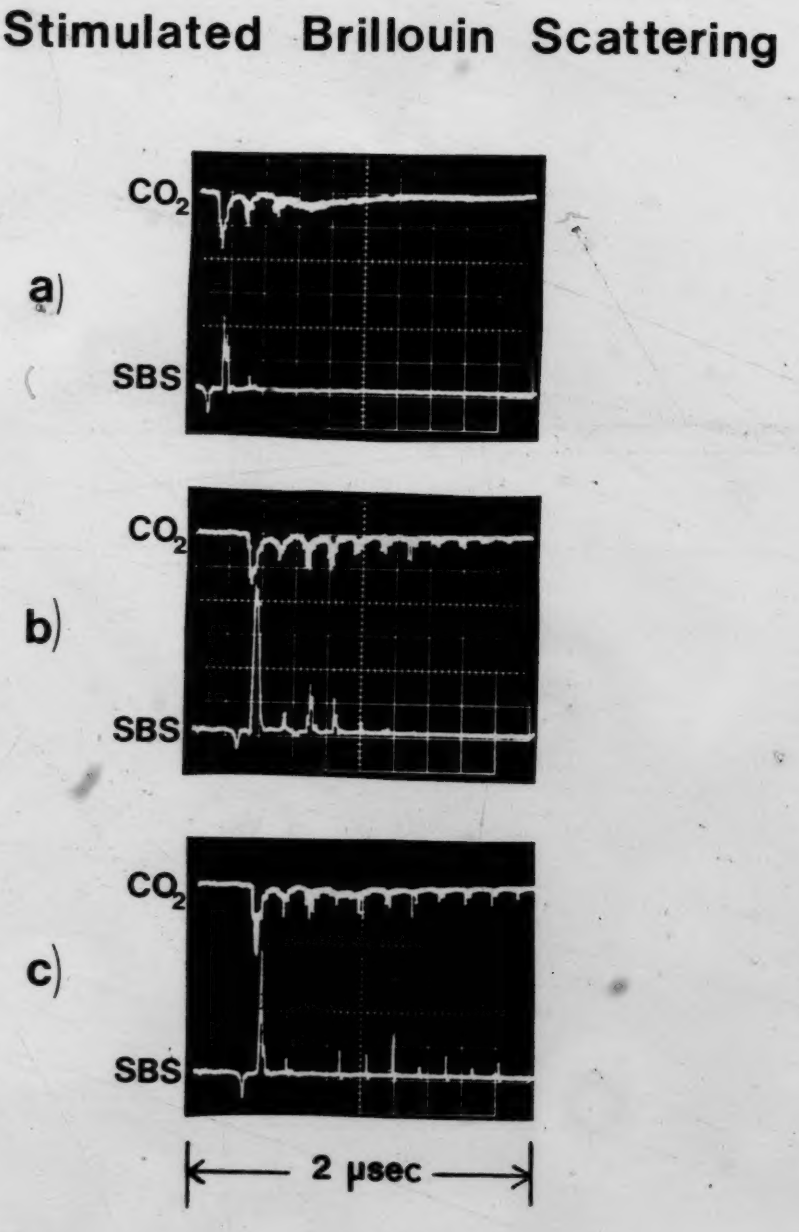

Figure 4.15 CO_2 (upper beam) and SBS signal (lower beam) Oscilloscope Traces for varying Experimental Conditions

Spikes observed in the laser signal were clearly related to the occurrence of SBS (identified by the frequency shift of the backscatter). The SBS signal returns along the input laser path and feeds back into the laser cavity. Once amplified, this signal produced the high intensity spikes seen in the input laser pulse. With proper plasma conditions these spikes would produce further SBS which in turn would feed back into the cavity and produce further modulation of the input signal. The time between bursts (~160 nsec) in the input signal corresponds to the round-trip time between the plasma and the laser (including the cavity transit time).

A further consequence of this feedback was to significantly damage an inter-cavity mirror which required replacement every 60-80 shots.

As can be seen in Figure 4.15, the temporal characteristics of the SBS signal varied from prompt scattering, occurring during the initial gain-switched spike of the input laser, to a combination of prompt scattering and SBS pulse trains, occurring during the tail of the laser pulse.

The degree of backscatter depended on the initial fill pressure (and thereby, the electron density) and on the incident laser power. Figure 4.16 shows the SBS reflectivity plotted against the product of the laser power and the fill pressure.

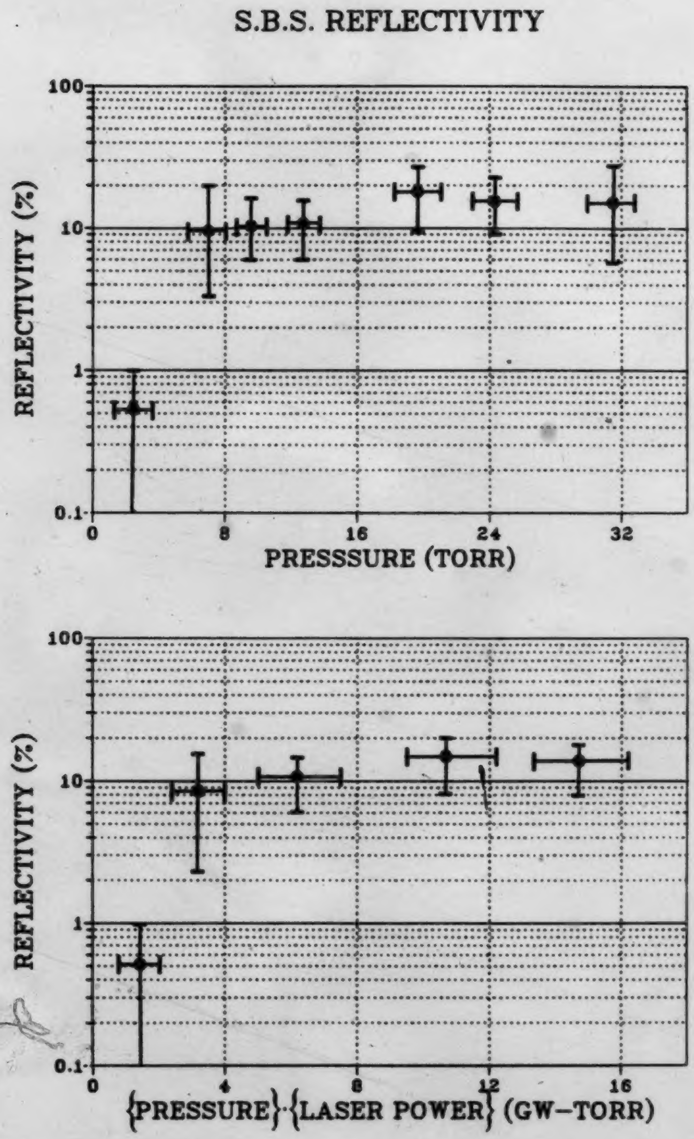

Figure 4.16 SBS Results: Reflectivity versus Laser Intensity

The SBS reflectivity R, is given by (Offenberger,1981),

$$R(1-R) = \epsilon[\exp\{G(1-R)\}-R] \qquad (4.1)$$

where,

ϵ=the initial noise level

G=the SBS gain

With R<<1, then,

$$\mathrm{Log}(R) \propto G \ .$$

The gain, from equation (3.65), can be expressed as,

$$G = K_0 \cdot (I \cdot N_e / T_e) \cdot (k_1 \cdot L) \cdot \tau_3 \qquad (4.2)$$

where,

K_0=.537
I =laser intensity , with I in units of 10^{12}watts/cm^2
N_e=electron density, with N in units of 10^{18}cm^{-3}
T_e =electron temperature, with $|T|$=ev
k_1=the incident wavenumber
and L =the interaction length.

The reflectivity, then, would be expected to be a function of $(I \cdot N_e)$. From Figure 4.16, the signal is seen to rise rapidly with this product. It also clearly saturates rapidly. The saturation mechanism will be discussed shortly.

The interaction length, L, in the above equation is taken to be the smaller of the focal depth of the input laser (~1.7 cm) or the distance over which the focal intensity variations lead to a factor of 2 decrease in the reflectivity. This latter distance was found to be ~1.2 cm and was therefore defined as the interaction length, L. The interaction length is set, therefore, to L=1.2 cm.

Taking typical conditions of $I=.1$, $N_e=.5$ and $T_e=50$ eV, equation (4.2) becomes,

$$G=3.68\cdot\tau_3 \tag{4.3}$$

The parameter τ_3 is a measure of ion acoustic wave damping and was defined in equation (3.61). It has a strong dependence on the electron-ion temperature ratio. At early times the electrons are expected to be considerably hotter than the ions. From simulation results, reasonable values for these temperatures are, $T_e=75$ eV and $T_e/T_i=5$. The value of τ_3 was determined numerically.

For these values, the maximum gain is calculated to be $G=19.5$. To produce a reflectivity of 10% a noise level of $\epsilon=3\cdot10^{-9}$ would be required. Offenberger(1982) has shown that in laser produced plasmas, noise levels of this order and larger are to be expected.

It has been shown that under the conditions of this experiment, electron-ion equilibration is very rapid. As T_i approaches T_e, the ion-wave damping is greatly enhanced. This leads to a significant reduction in the SBS gain. Taking $T_e=T_i=45$ eV and keeping all other parameters the same, the calculated gain decreases to a value of $G=4.9$. This reduction in the gain, as a result of rapid electron-ion equilibration, is the most likely reason for saturation.

Spectral features of the SBS signal are shown in Figure 4.17. The input CO_2 spectrum, the experimental SBS spectrum, and a theoretically determined spectrum are

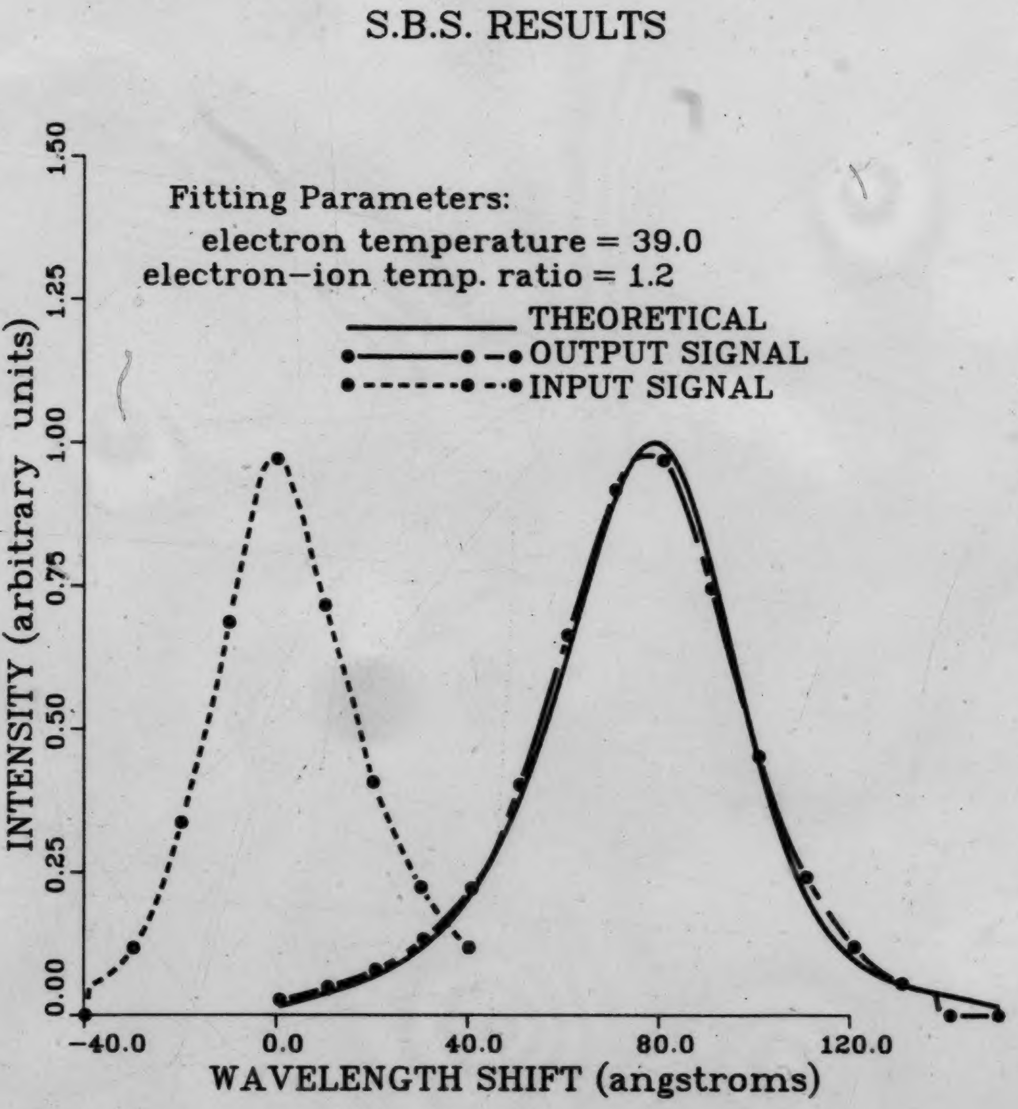

Figure 4.17 SBS Results: Input, Output and Theoretically Fitted Spectra

included in this figure.

The theoretical line shape was determined by first evaluating the gain for specified plasma conditions. The input spectrum was then taken and multiplied by $\exp[G(1-R)]$ to give the theoretical output spectrum. This was compared with the experimental profile and a total squared deviation was calculated. The plasma conditions were then adjusted until the deviation was minimized.

As indicated in Figure 4.17, the conditions giving rise to the best fit were T_e=39.0 ± 2.ev., T_e/T_i=1.2 ± .1, and N_e=4.5 ± .5·10^{17}cm^{-3}. The range assigned to the values of these parameters is based on a visual inspection of the fitted profile. This corresponded to an increase of ~50% in the total measured deviation. The sensitivity of the theoretical profile to the electron and ion temperatures makes this a particularly useful diagnostic for the determination of the plasma temperature.

Figure 4.18-a shows the SBS spectrum taken for a case where the reflected signal was entirely prompt. Figure 4.18-b shows the spectrum for a case where the signal is a combination of prompt and late-time scattering. In the case of prompt scattering, the spectrum shows only the red-shift expected for the SBS signal. The late-time scattered spectrum also shows an additional shift back toward the incident wavelength. It is important to note here, as was discussed in Chapter 2, that for low fill pressures no back reflection was observed, indicating that

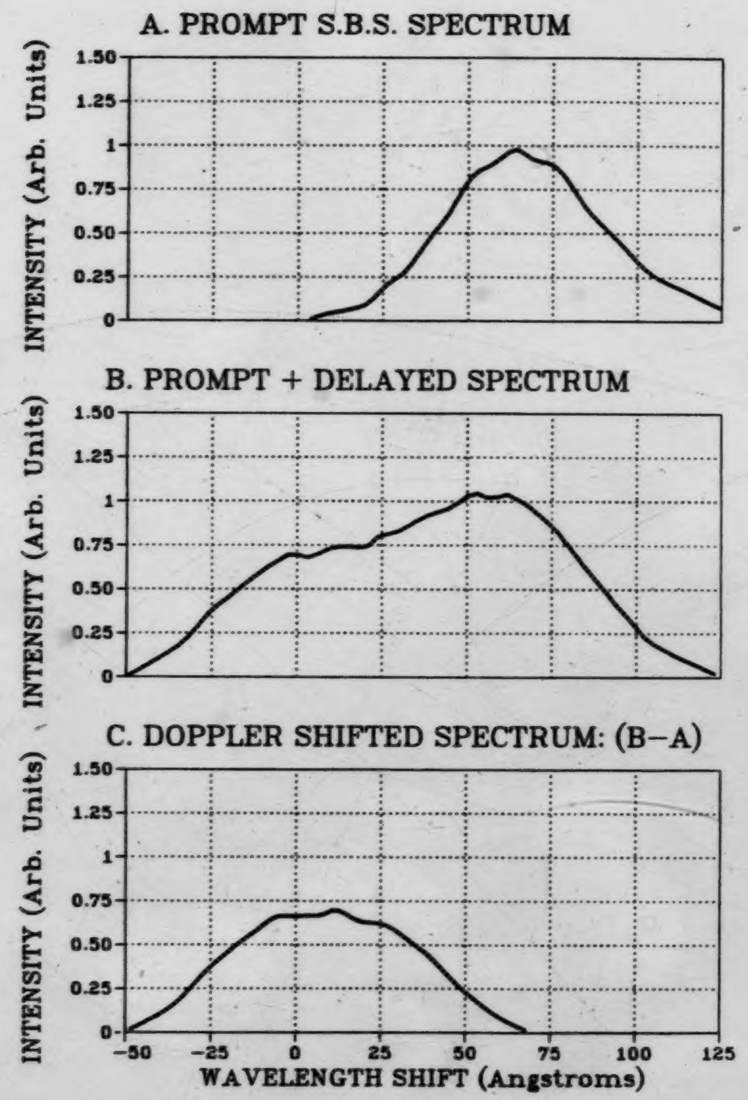

Figure 4.18 SBS Results: Prompt and Delayed Spectra

the reflection of the incident light from the orifice and other surrounding structures was negligible.

By subtracting the prompt spectrum from the late-time spectrum, the shifted SBS spectrum (indicated by the dotted line in Figure 4.18-c) is left.

This shift of the SBS signal is due to the flow of the plasma out of the orifice region. This doppler shift of the spectrum allows the flow velocity to be calculated and from this an estimate of the plasma temperature can be made. With $T_e=T_i=T$, the flow pressure is given by,

$$p \propto kT=(1/2)\cdot mv^2 \qquad (4.4)$$

The flow velocity is therefore given by,

$$v=(2kT/m)^{(1/2)} \qquad (4.5)$$

The doppler shift, $\Delta\lambda$, is given by,

$$\Delta\lambda/\lambda_0=2v/c$$

so, for a measured shift of $\Delta\lambda=62$ A,

$$v\simeq1.85\cdot10^7 \text{ cm/sec}$$

from which is obtained,

$$kT=40 \text{ eV} \qquad (4.6)$$

This agrees very well with the previously determined value for the plasma temperature.

4.4.2 Stimulated Raman Scattering, SRS

As with the SBS, SRS was observed only when using the f/15 focussing optics.

Figure 4.19 shows oscilloscope traces of the CO_2 input signal and the associated Raman backscatter. Temporally, the

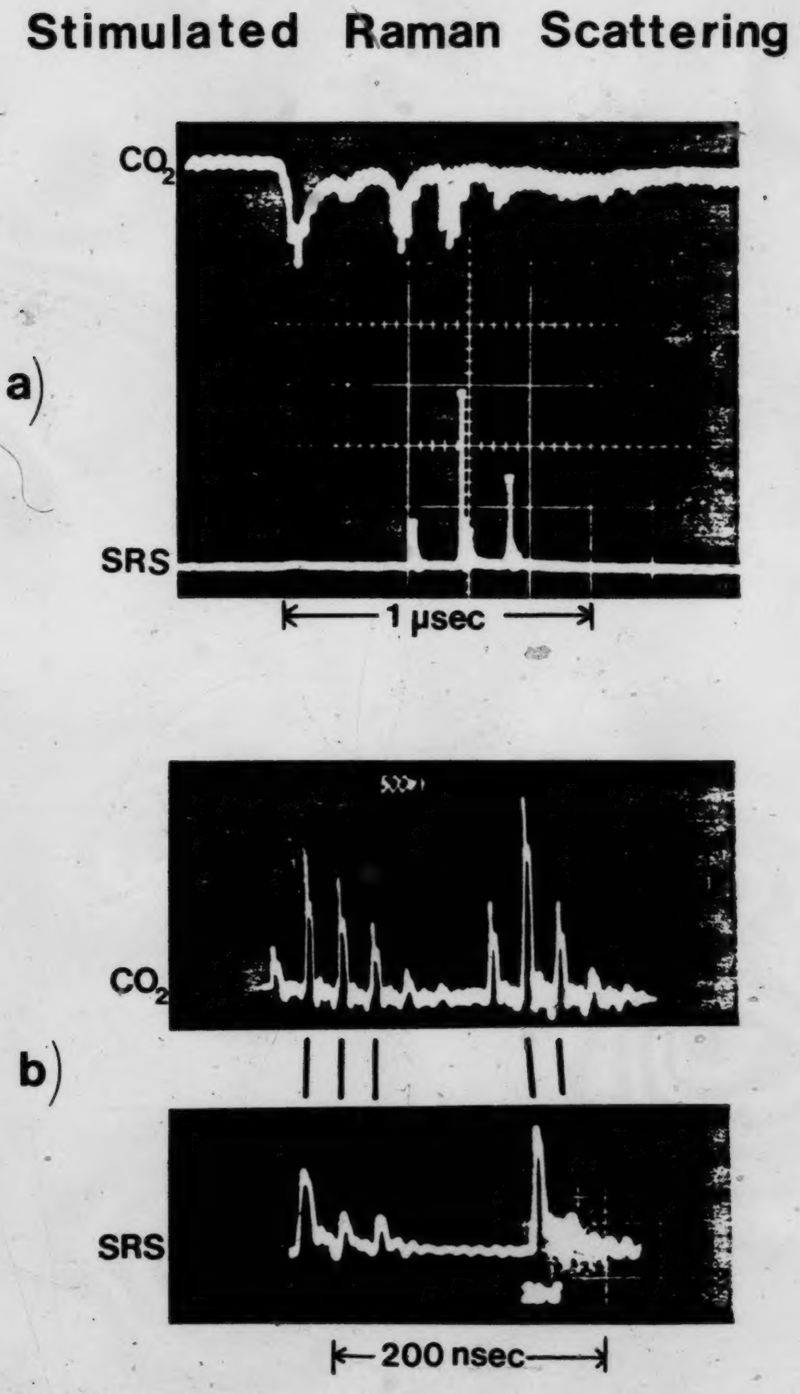

Figure 4.19 CO$_2$ (upper beam) and SRS signal (lower beam) Oscilloscope Traces.
a) and b) from different laser shots but similar experimental conditions

SRS signal is characterized by ~5 nsec spikes.

The SRS signal was only observed at late times and coincided with high-intensity spikes in the input signal occurring at times >400 nsec after the initial breakdown.

The magnitude of the SRS reflectivity was highly variable. In Figure 4.20, the average reflectivity is plotted as a function of input intensity. Below the observed threshold value of $4\cdot10^{10}$ W/cm^2 the reflectivity was $<10^{-4}$. From this figure it is apparent that for higher intensities the reflectivity saturates at a level of ~.7%.

Threshold intensity levels for SRS were calculated in Chapter 3. These calculations were based on both inhomgeneity and damping criteria.

With a density scale length of 20 cm, the inhomgeneity condition yielded a threshold intensity of $\sim5\cdot10^{10}$ W/cm^2. The intensity value agrees very well with that observed experimentally. The delay in the onset of the SRS signal is explained in part by the time required for the plasma column to develop the long density scale length needed to satisfy the inhomgeneity condition.

From the damping criteria, the threshold intensity was determined to be $4.4\cdot10^{10}$ W/cm^2. This is also in very good agreement with the observed value.

Spectral measurements of the SRS signal are presented in Figure 4.21. In Figure 4.21-a the SRS signal consisted primarily of a single spike. In such cases a single spectral peak was observed. The more structured spectra of

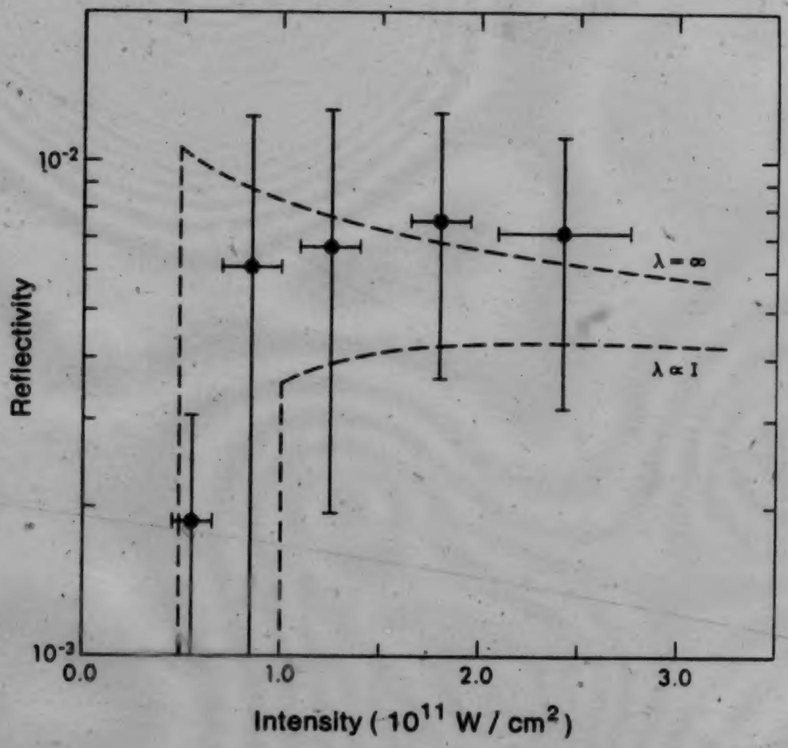

Figure 4.20 SRS Results: Reflectivity versus Laser Intensity

S.R.S. EXPERIMENTAL RESULTS

A. SINGLE SPIKE SPECTRA

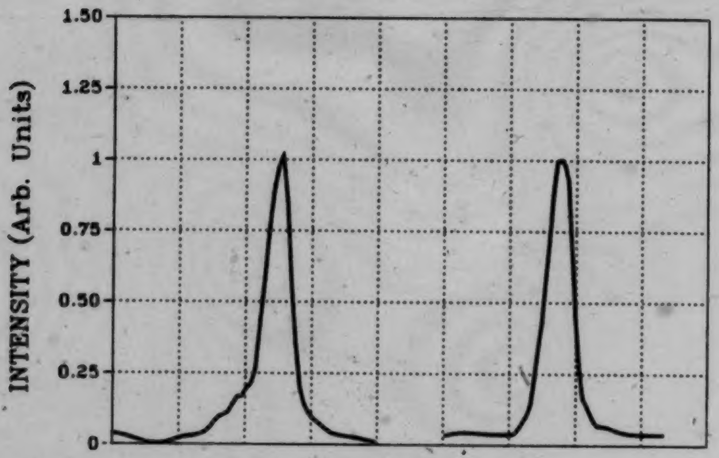

B. MULTIPLE SPIKE SPECTRA

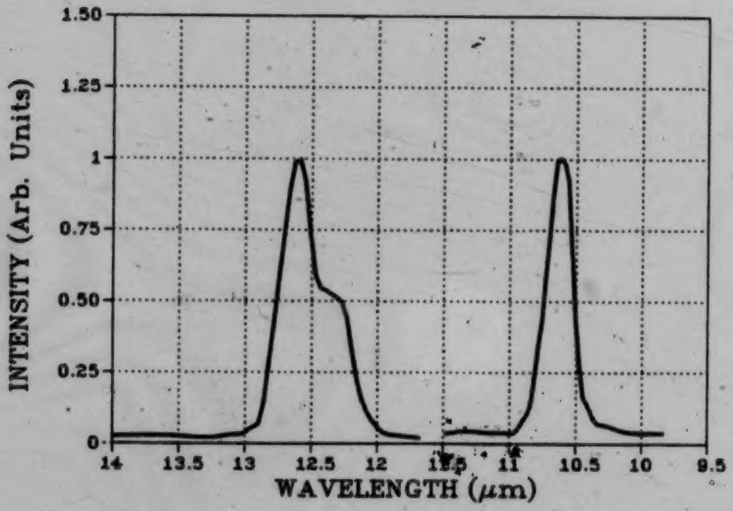

Figure 4.21 SRS Results: Spectral Characteristics

Figure 4.21-b arises from a backscattered signal consisting of a sequence of spikes.

The spectral shift of the scattered signal is directly related to the plasma frequency which, in turn, is related to the plasma density. The density will fluctuate in time and space throughout the development of the plasma column. The structured spectra reflects these variations in density.

The average scattered wavelength was at 12.7 μm which corresponds to an electron density of $N_e = 2.7 \cdot 10^{17}$ cm^{-3}. However, over the entire data set, the scattered wavelength varied over a range of 12.0 - 13.5 μm corresponding to a density range of 1.5 - $4.5 \cdot 10^{17}$ cm^{-3}. These density values are in very good agreement with the interferometrically measured values previously discussed.

As mentioned, Figure 4.20 shows the rapid saturation of the SRS instability. The growth of the SRS signal will be limited by the damping of the electron-plasma wave. Landau damping from the general population of 45 eV electrons is insignificant. This is because the thermal velocity is well below the velocity of the plasma wave and there can be only limited interaction between the wave and the particles. The simulation studies of Estabrook et al(1980) showed that there will be a population of hot electrons associated with the SRS process. For the conditions of this experiment the temperature of the hot electrons is expected to be ~2.1 keV.

Offenberger et al(1982) proposed that the SRS instability, observed in this experiment, would saturate due to the enhanced Landau damping from these hot electrons. Taking limiting cases for λ, the phase-mismatch gradient, a self-consistent saturation reflectivity was determined by calculating the fraction of hot electrons and accounting for the additional hot-electron Landau damping. The theoretical curves, also shown in Figure 4.20, agree remarkably well with the experimental results.

From the hot-electron, Landau damping model a hot-electron density of $\sim 3 \cdot 10^{14} \mathrm{cm}^{-3}$ is predicted. Experimental evidence to support this prediction was inconclusive. The expected level of x-ray emission from the electrons was found to be approximately at the detection limit. Attempts to detect the particles directly with probes were also unsuccessful due to excessive electrical problems.

4.4.3 Thomson Scattering Results

Thomson scattering of ruby laser light was used to try to determine the plasma temperature. The experimental methods used were outlined in Chapter 2. These experiments were performed only with f/5 focussing of the input CO_2 laser.

All scattering data was obtained from a position $\sim$1.5 cm away from the input end of the solenoid. Attempts to obtain data further along the plasma column were unsuccessful. All data were obtained without any aperturing of the collection optics and without an input slit on the monochromator. The input slit is normally used to define the scattering region within the plasma, however significant signal levels were only obtained by maximizing the region probed and operating without an input slit. These conditions, however, inherently limit the utility of the data.

Effectively, then, the scattering region was defined by the focal depth of the input ruby laser. The focussing system for the ruby laser resulted in a focal spot size of ~200μm and a focal depth (defined by the half-intensity points) of ~4 mm.

Scattered spectra were obtained at various times during the plasma development. Examples of the observed spectra at early times (t≈60 nsec) and at late time (t≈250 nsec) are presented in Figures 4.22 and 4.23 respectively. Both the raw data and an interpolated cubic spline curve (with very slight smoothing) are given in these figures.

The analysis of the spectra consisted of first generating a theoretical scattered spectrum based on specified plasma parameters of electron temperature, ion temperature, and electron density. The theoretical profile was compared with the experimental and a total squared deviation was determined. The plasma parameters were then adjusted until the deviation was minimized.

Results of this fitting process for the data given in Figures 4.22 and 4.23 are given in Figures 4.24 and 4.25, respectively. In these figures, the experimental and theoretical spectra and the fitting parameters used to

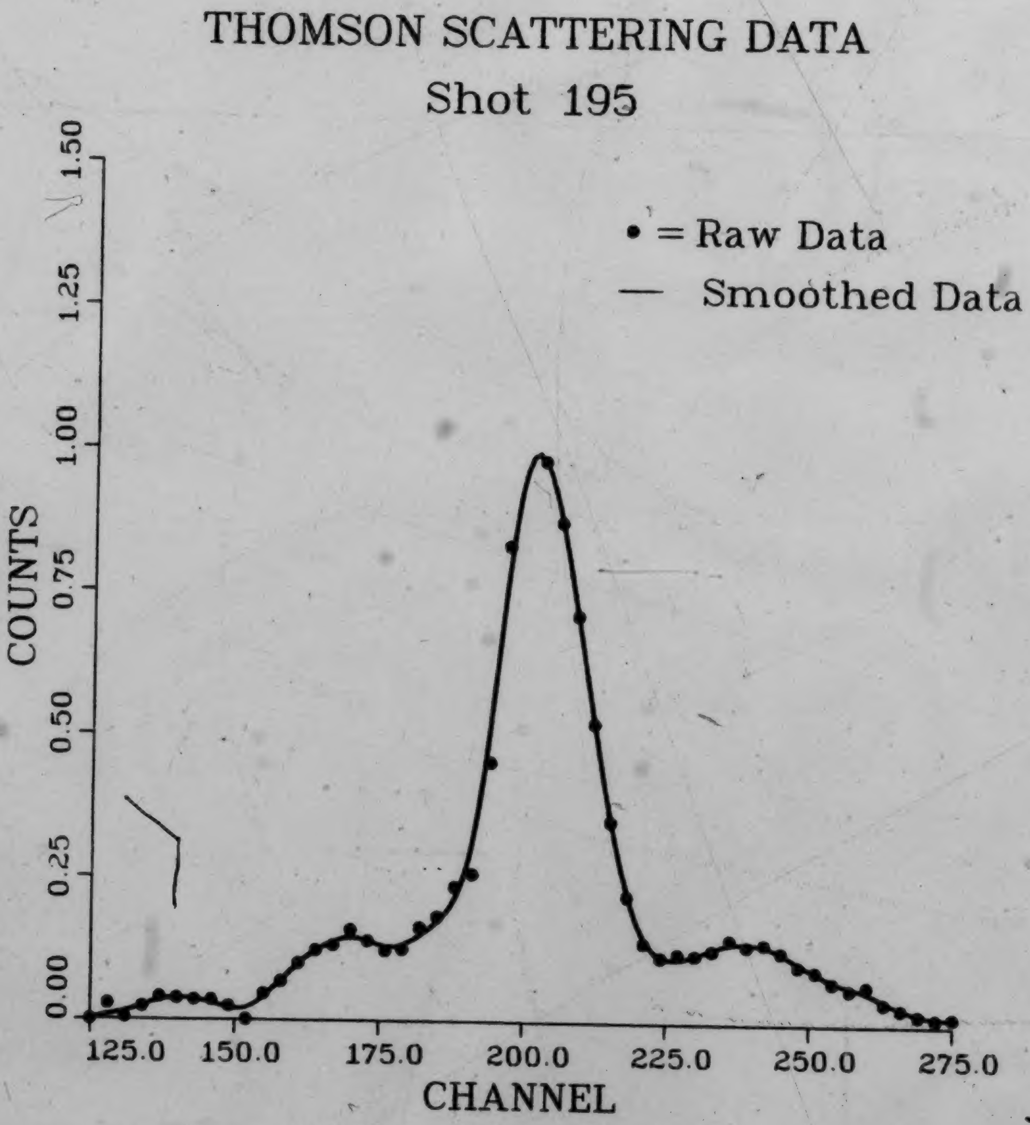

Figure 4.22 Thomson Scattering Data (Raw and Smoothed): T=60 nsec (3.17 A/Channel)

1

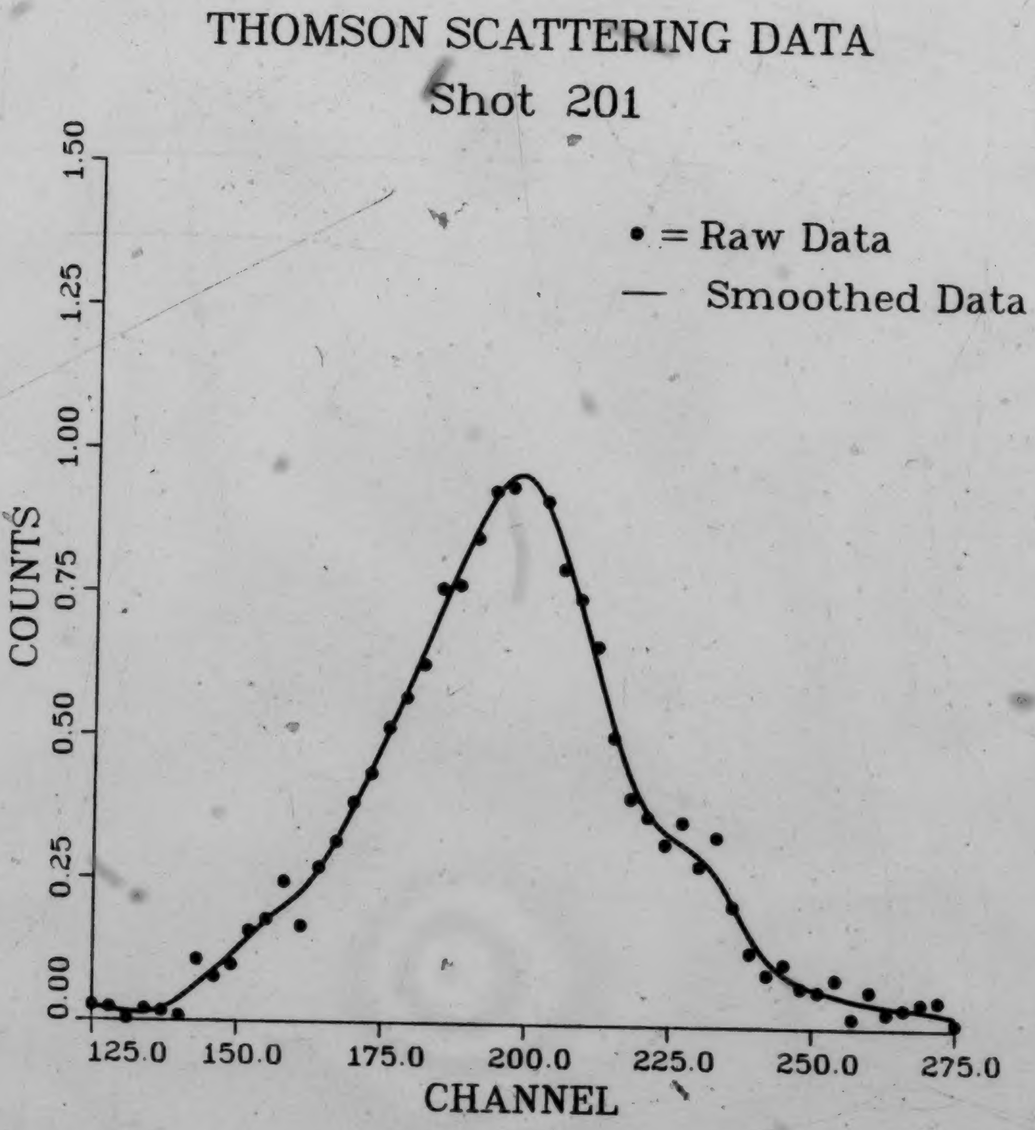

Figure 4.23 Thomson Scattering Data (Raw and Smoothed):
T=250 nsec (3.17 A/Channel)

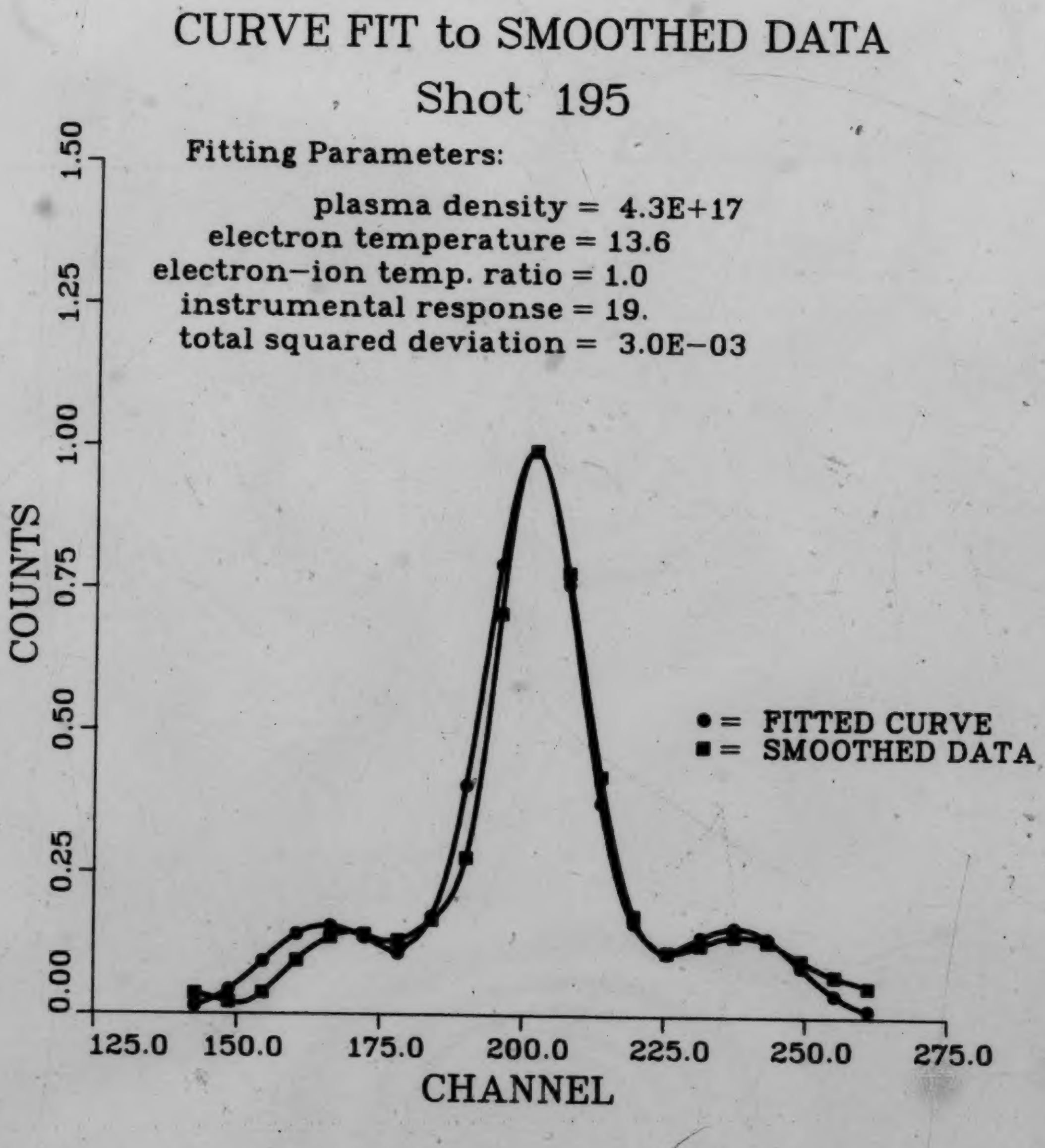

Figure 4.24 Thomson Scattered Experimental and Theoretical Profile:
T=60 nsec (3.17 A/Channel)

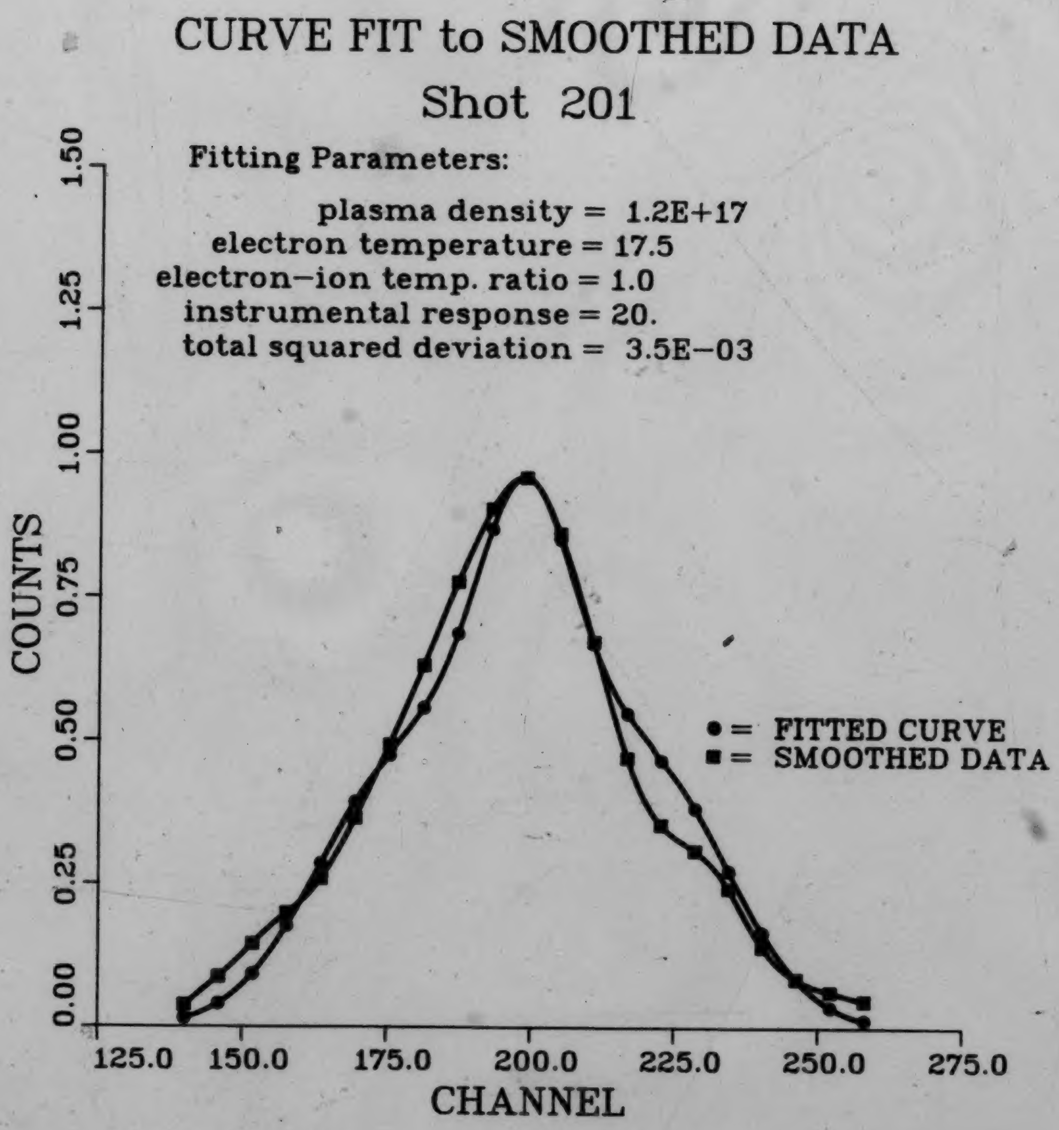

Figure 4.25 Thomson Scattered Experimental and Theoretical Profile:
T=250 nsec (3.17 A/Channel)

generate the theoretical spectra are given.

These results are typical of a number of spectra used in the analysis. At early times (<100 nsec, 3 shots analyzed) the electron temperature was found to be in the range 10 - 15 eV and the density in the range $4 - 5\cdot 10^{17}$cm^{-3}. At late times (>150 nsec, 4 shots analyzed) the electron temperature was found to be in the range of 20 - 30 eV and the density in the range $.6 - 1.2\cdot 10^{17}$cm^{-3}.

The density values are in good agreement with those obtained interferometrically. The overall behaviour of the density is also consistent insofar as it decreases with time, as the plasma column expands.

The temperature values at late time are in reasonable agreement with estimates of the plasma temperature from energy balance. They are also in reasonable agreement with the results of the SBS spectral analysis considering the larger plasma radius associated with f/5 focussing and the averaging of the Thomson scattered signal over the focal volume. As will be shown in the next chapter, the agreement with the 2-D simulation is also quite good.

The temperature determined at early times is inconsistent with what is expected. At early times the electrons are strongly heated and the temperatures should be considerably higher than those found at later times.

A possible explanation for this anomalous result involves the radial integration of the Thomson scattered signal. At ~60 nsec the radial extent is (from radial streak data) only 3-4 mm. Of this only the central core will be heated to the very high temperatures expected. If the region over which the Thomson scattered signal is integrated (to a radius of ~2.0 mm) contains a significant percentage of unheated plasma then the determined temperature would be certainly reduced. The precise effect is complicated by the fact that the regions of higher temperatures will also be regions of lower density and the scattered signal will be less heavily weighted than it is for the colder, denser regions.

Further discussion of this situation will be given in Chapter 5 where the simulation code results are presented and temperature and density distributions are examined.

CHAPTER V

Simulation Results

5.1 Preliminary Remarks

The model used to simulate the laser-heated solenoid experiment was described in Chapter 3. Some key features are reproduced below.

The code uses an initially fully ionized plasma. In these simulations a hydrogen plasma, at a initial temperature of 1 eV, is used. The plasma motion is determined from the set of MHD equations (including laser-induced ponderomotive terms) using a co-ordinate system fixed to the magnetic field lines. Spatial variations of the laser (refraction, diffraction and absorption) are included. The electric field of the laser is determined by a direct solution to the Helmholtz equation.

The array size of the MHD calculation mesh was variable but in the results presented here the mesh was fixed as a 30 X 60 array; 30 points radially and 60 points axially. This matched the size originally used by McMullin et al.(1979) and provided good resolution and reasonable computer costs.

The laser effects were determined on a separate grid and then transformed to the MHD mesh. Radially, the size of the laser grid spacing was initially fixed to 1/5 of the minimum beam width. This resulted in a typical laser grid spacing of ~1/17 of the MHD grid spacing. It was found that limiting the laser grid size to 1/7 of the MHD spacing resulted in only minor changes in the output but a significant reduction in computer costs. This limitation was in effect for all the results presented in this chapter.

During any program timestep, the laser grid adjusted according to the maximum beam width. In order to reduce the effects of reflections of the laser, it was necessary to set the laser grid size to a value 5 times the maximum beam width. In cases where this extended beyond the radial extent of the MHD grid, the MHD parameters used in the laser calculation were taken from the outermost point available.

Single precision was used for all MHD calculations. Because of several large summations over the laser grid, it was necessary to use double precision in the laser code.

Depending on the parameter settings, the simulation runs presented here required from 10 to 20 minutes of C.P.U. time on an Amdahl-7 computer.

5.2 Simulation Runs

A study was undertaken in which plasma and laser parameters were systematically varied. In each case the code was run to a simulation time of ~300 nsec. At specified time steps (typically every 20 nsec) the data were stored on magnetic tape. These data were then accessed by other routines in order to provide 3-dimensional plots and 2-dimensional profiles (axial and radial) of the laser and plasma parameters.

The main parameters varied during the study were; the laser focussing ratio (f/5 and f/15), the laser energy, the initial plasma density ($5\cdot10^{17} - 1\cdot10^{18}\,\mathrm{cm}^{-3}$), and the magnetic field strength (40 - 75 kG). Table 5.1 gives a list of the parameters used in 16 simulation runs.

Other parameters were held constant throughout these runs. These included the solenoid radius (1 cm), the solenoid length (10 cm), the initial electron temperature (1 eV), the unfocussed laser beam size (10 cm), the laser focal spot size ($400\mu\mathrm{m}$), and the shape of the laser pulse. The laser profile is shown in Figure 5.1.

The laser pulse shape was chosen to closely resemble the experimental pulse shape. The input energy was set to 120 joules for most simulations. This is lower than the average energy used in the experiments (~200 joules) since, depending on the hydrogen fill pressure, 30-80 joules are required to ionize the gas. This energy was assumed to come entirely from the initial spike of the laser pulse.

5.3 Simulation Results, 3-D Representations

Figures 5.2 - 5.11 give 3-D representations of the electron temperature, the ion temperature, the plasma density and the laser absorption for several simulation runs. Note that in the case of the density plots the central axis is opposite to the others and is presented nearest the viewer. This provides a better view of the density structure but makes a visual correlation between the density and the

Table 5.1 Run Parameters used in Simulation Study

RUN	DENSITY (x 10^{18})cm^{-3}	B–FIELD (kG)	f/RATIO	LASER ENERGY (Joules)
1	0.75	50	f/5	120
2	0.50	50	f/5	120
3	1.00	50	f/5	120
4	0.75	30	f/5	120
5	0.75	75	f/5	120
6	0.75	40	f/5	120
7	0.75	60	f/5	120
8	0.50	75	f/5	120
9	0.75	100	f/5	120
10	0.75	60	f/5	60
11	0.75	60	f/15	120
12	0.50	60	f/15	120
13	1.00	60	f/15	120
14	0.75	100	f/15	120
15	0.75	80	f/15	120
16	0.75	60	f/15	60

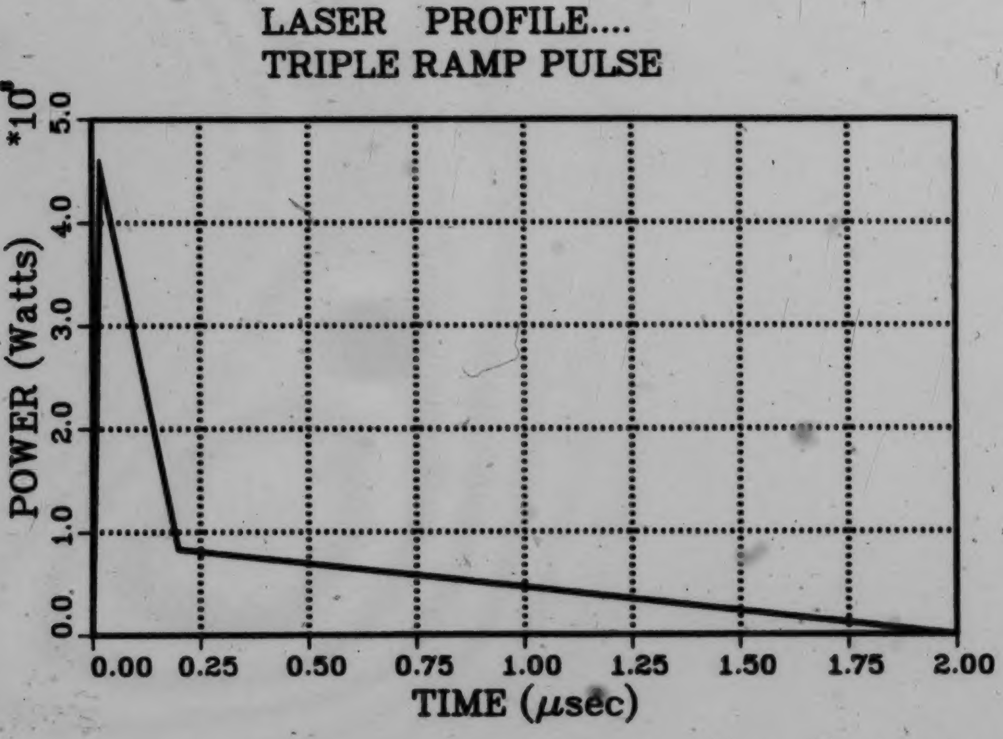

Figure 5.1 Laser Profile used in Simulation Study

other parameters more difficult.

Figures 5.2 and 5.3 correspond to an intermediate time in simulation Run 7. In general terms this run is very typical of all runs using f/5 focussing.

From Figure 5.3 it is clear that the electrons are hottest in a relatively small region in the vicinity of the laser focus. Moving radially and axially from this region the temperature drops off very rapidly. Along the central axis the temperature then becomes fairly uniform decreasing slowly until reaching the leading edge of the plasma column. The electron temperature distribution is not entirely uniform and shows some structural development. These structures are consistent for all parameters and will be discussed shortly.

The ion temperature distribution (Figure 5.2) is more uniform than that of the electron temperature. It is not characterized by strong heating in the focal region and, in fact, shows a slight rise just outside this area. In the focal region the high laser intensity preferentially heats the electrons. The ions are heated through collisions with the electrons. The high electron temperature results in axial movement of the plasma. This results in an increase in density outside this region and subsequently, an enhanced electron-ion collision rate and higher ion temperatures. Outside the focal region, the electron and ion temperatures are virtually identical (qualitatively and quantitatively), indicative of very rapid equilibration.

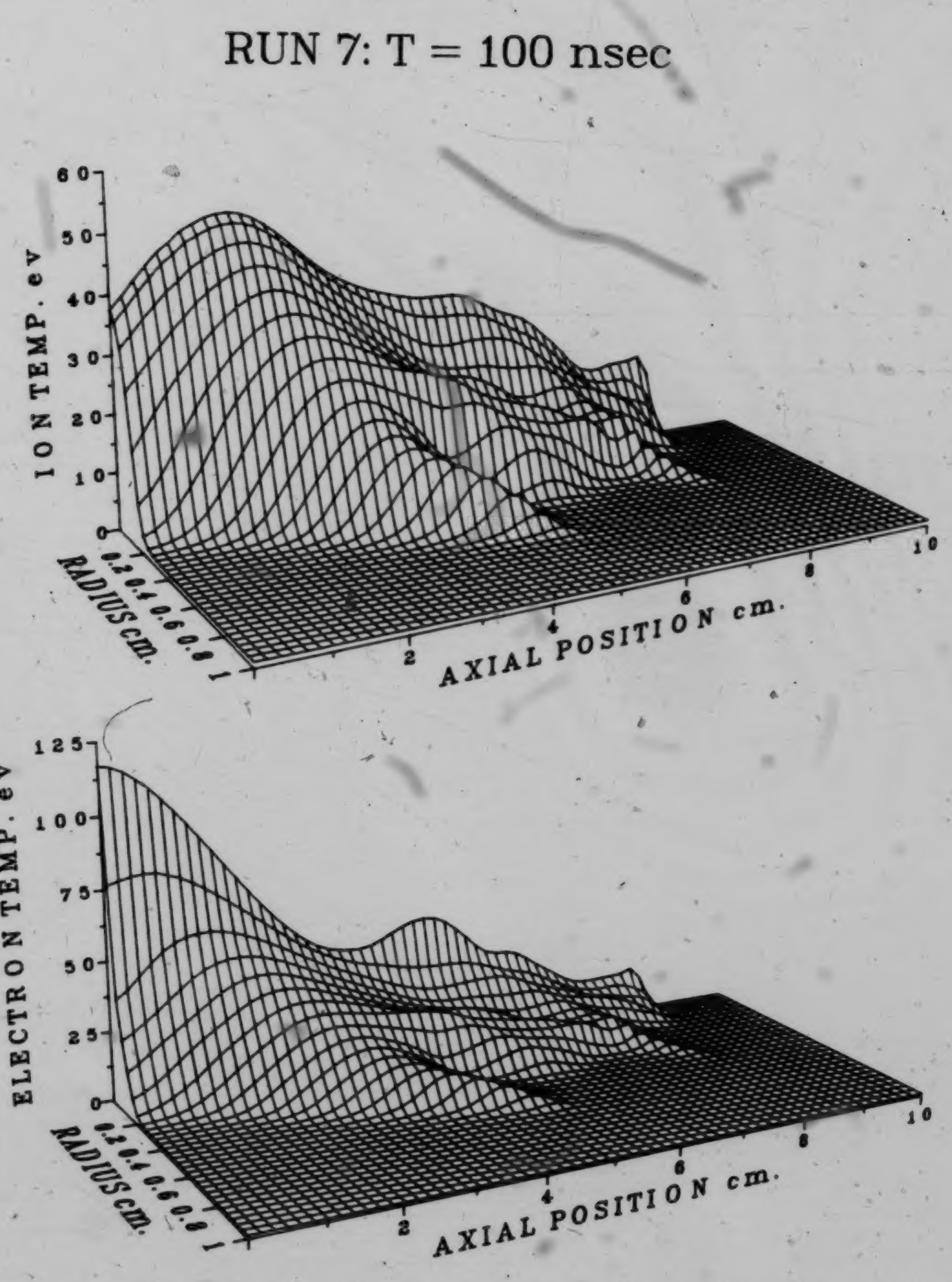

Figure 5.2 Electron and Ion Temperature Distributions: Simulation Run 7 at T=100 nsec

RUN 7: T = 100 nsec

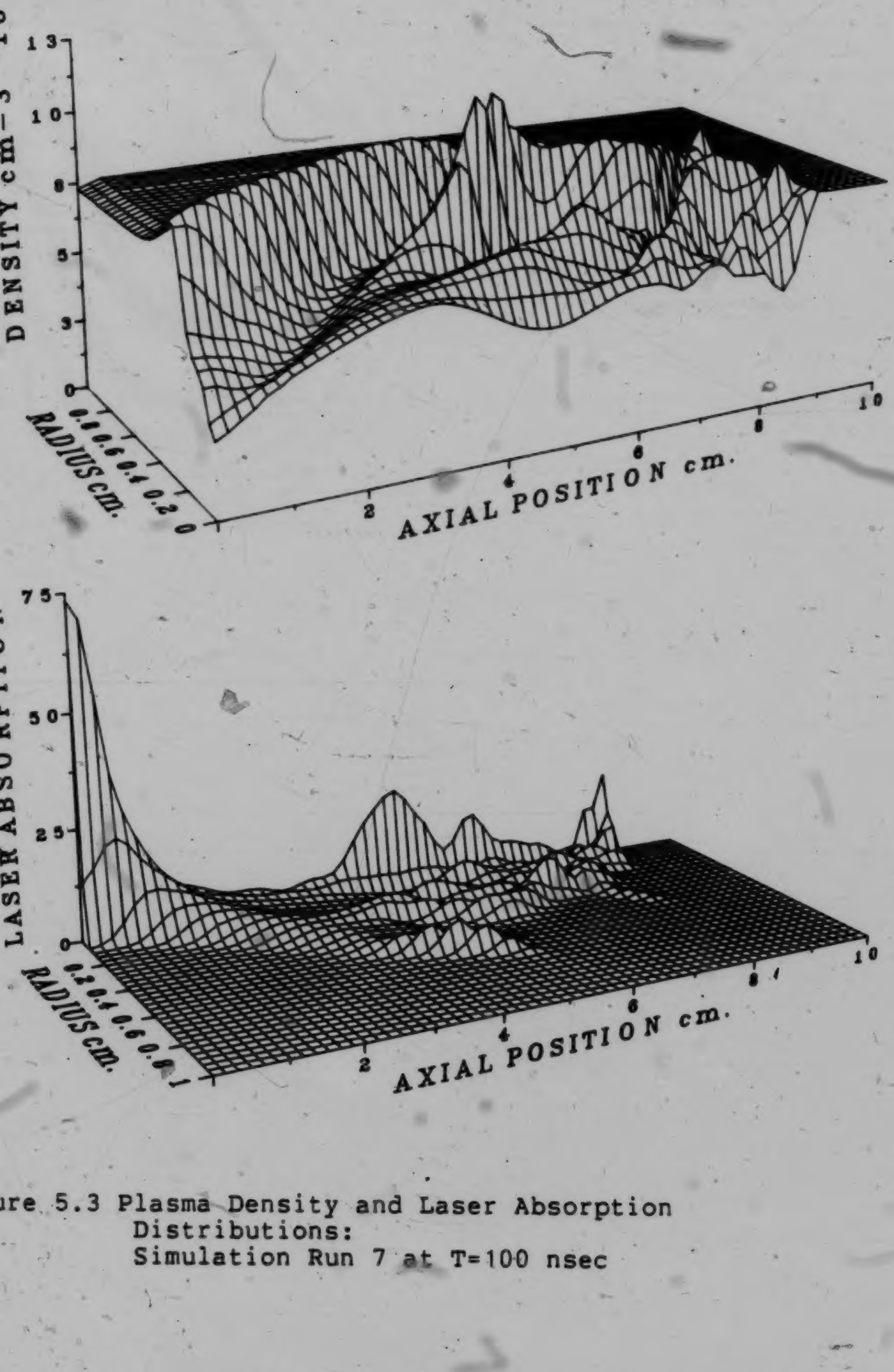

Figure 5.3 Plasma Density and Laser Absorption Distributions:
Simulation Run 7 at T=100 nsec

It will be shown that a density minimum on axis is formed very rapidly. By the 100 nsec point of Figure 5.3, a density minimum along the axis is clearly established. Also indicated in the density distribution is the effect of the defocussing of the laser from the focal region. In fact, all parameters show the radial expansion associated with this effect.

The effective f/ratio of the radial expansion of these parameters from the focal region is determined to be f/3.6, faster than the f/5 ratio of the input laser. This is due to both the expected plasma expansion by ion transport and to the increased laser absorption in the outer regions. The laser absorption is enhanced in these outer locations because the plasma density is higher and the electron temperature is lower than the inner core. The increased laser absorption leads to higher plasma temperatures and more rapid radial expansion.

There are further complication due to laser effects. Figure 5.4 shows the laser flux distribution for this run. In this figure the regions near the focus and away from it have been scaled independently. The scale factor in the focal region was $2.07 \cdot 10^{16}$W/m^3 while outside it the scale factor was $1.16 \cdot 10^{15}$W/m^3. The location of the change in scale is clearly indicated by the step in the distribution. This procedure was necessary to allow details of the flux distribution outside the focal region to be apparent. The laser is seen to be clearly trapped within the plasma. The

RUN 7: T = 100 nsec

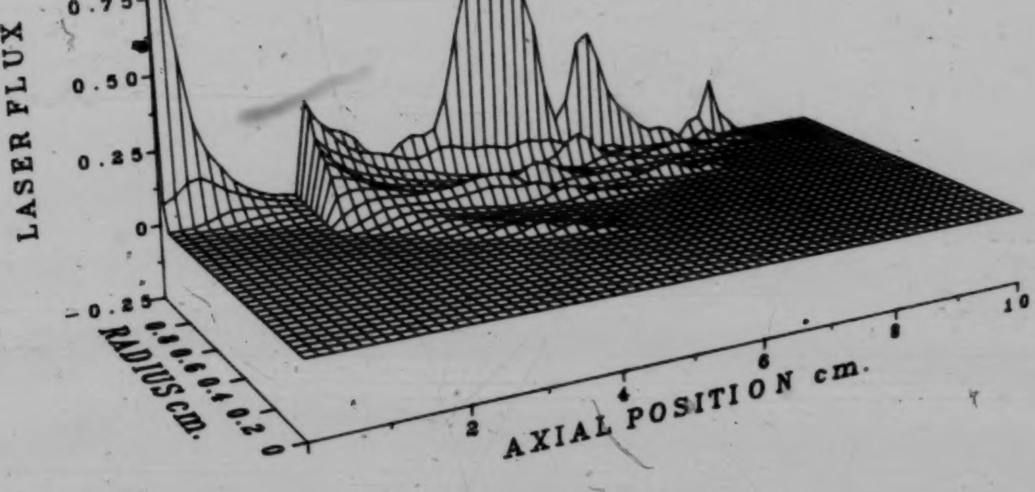

Figure 5.4 Laser Flux Distribution:
Simulation Run 7 at T=100 nsec

flux is, however, rather erratic and shows only weak signs of re-focussing. This is partly due to the lack of a parabolic density profile which has been shown to be necessary for smooth re-focussing of the beam. There is also a disruption of the beam caused by the density structures seen in Figure 5.3.

There is an interaction between the laser and plasma through the ponderomotive forces. The axial and radial ponderomotive forces are shown in Figure 5.5.

Here, again, the regions near and away from the focal area have been scaled independently. In the case of the radial component of the ponderomotive force, the normalization factor (in units of newtons/m^3) near the focus was $1.3 \cdot 10^8$ while outside it was $1.3 \cdot 10^7$. For the axial component, the normalization factor near the focus was $1.6 \cdot 10^7$ and outside it was $1.0 \cdot 10^6$. The radial component is then approximately a factor of ten larger than the axial component. Nevertheless, these forces are very weak and simulation runs in which the ponderomotive force terms were not included showed no noticeable changes in the density distribution.

Before discussing the possible cause of the observed density structures, it should first be noted that they do not strongly influence the analysis of the simulation results. The structures are fairly localized and do not interfere with the determination of the plasma fronts (axially or radially).

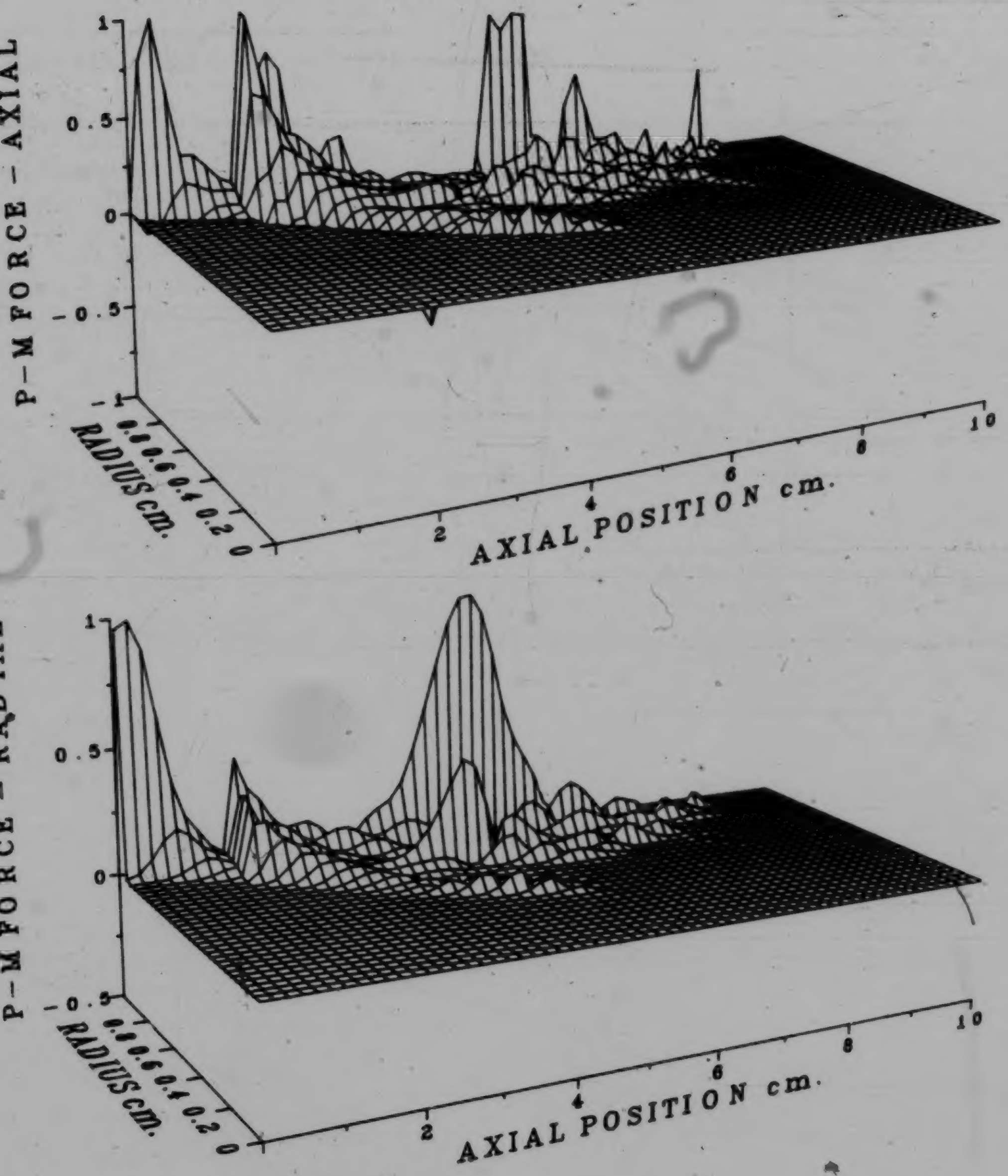

RUN 7: T = 100 nsec

Figure 5.5 Axial and Radial Ponderomotive Forces:
Simulation Run 7 at T=100 nsec

An initial region of high density may result from non-uniform heating due to diffraction of the laser beam. Once a region of higher density develops there will be a natural tendency for it to grow since the laser may be reflected out of this region and preferentially heat the neighbouring plasma. The heated plasma will expand into, and thus enhance, the regions of higher density. For this reason the structures, reflected in all parameters, would be expected to grow.

Finally, in discussing the distribution of the laser absorption, it is interesting that neither situation described in Chapter 3 is entirely applicable. In Chapter 3 the value of the parameter a, the ratio of the absorption length to the plasma length, was assumed to be either $a \ll 1$ or $a \simeq 1$.

In Figure 5.3 it is clear that there are two regions of high absorption. Near the focal region the laser flux is very large, resulting directly in high absorption. At the front of the plasma column there is a very narrow region of high absorption due to the presence of lower plasma temperatures and higher densities. Between these two regions the level of absorption is relatively uniform although the distribution has some structure associated with the laser flux and the plasma density. The fraction of the total energy in each of these regions was determined. In the focal region 20-25% is absorbed, at the plasma front 10-15% is absorbed and the remaining ~65% is absorbed in the region in between.

With most of the energy absorbed in a fairly uniform manner in a region approximately equal to the plasma length the assumption of $a \simeq 1$ would seem to be reasonable. The presence of these high absorption regions, particularly in the critical region of the plasma front, would be expected to alter the 1-D axial propagation models presented in Chapter 3.

Figures 5.6 and 5.7 show the distributions of the laser and plasma parameters for the same run, but at a later time. Compared with the earlier time, the plasma column has expanded both axially and radially. The laser power level is past the high intensity spike and into the lower levels in the tail of the pulse. Consequently, the heating in the focal region is considerably reduced. Furthermore, the expansion of the column has resulted in a cooling of the plasma. The net result is more uniform and somewhat reduced temperature distributions.

The density structures observed earlier are still present and somewhat enhanced. There is some axial propagation of these forms.

The laser absorption is still quite high in the focal region, but because the column has extended beyond the solenoid length of 10 cm, the strong absorption near the front is no longer visible.

The temperature and density distributions for lower initial density conditions are given in Figure 5.8. The general behaviour is very similar to the previous run except

RUN 7: T = 300 nsec

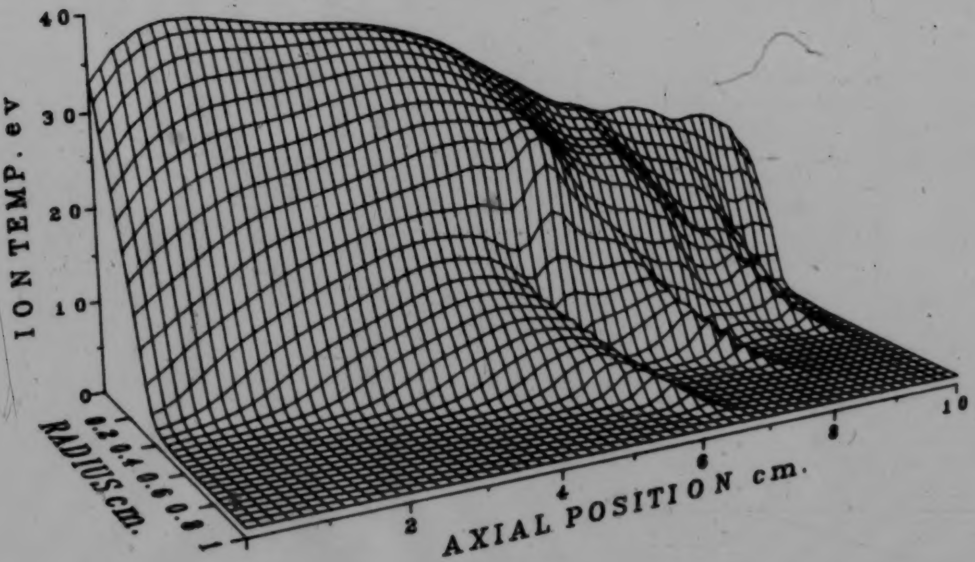

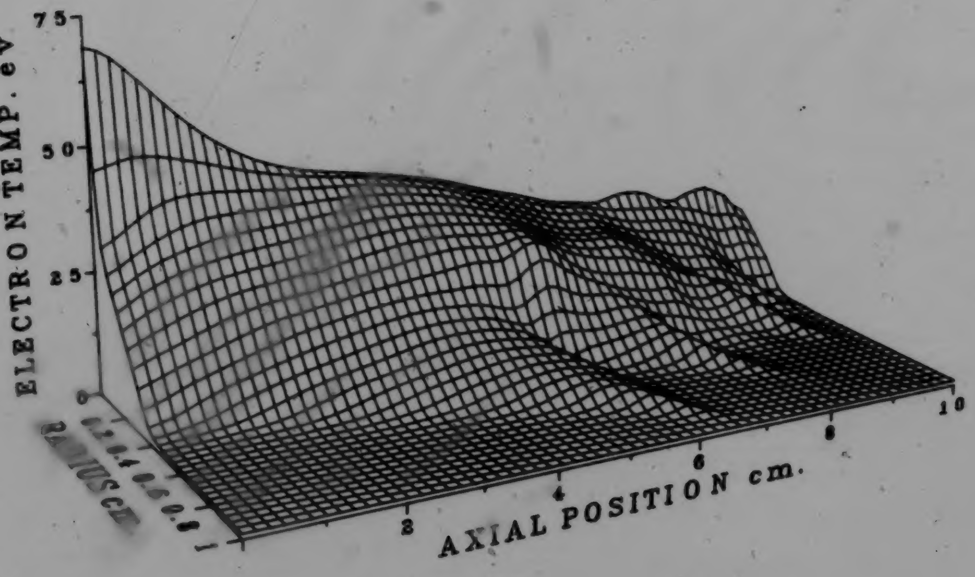

Figure 5.6 Electron and Ion Temperature Distributions: Simulation Run 7 at T=300 nsec

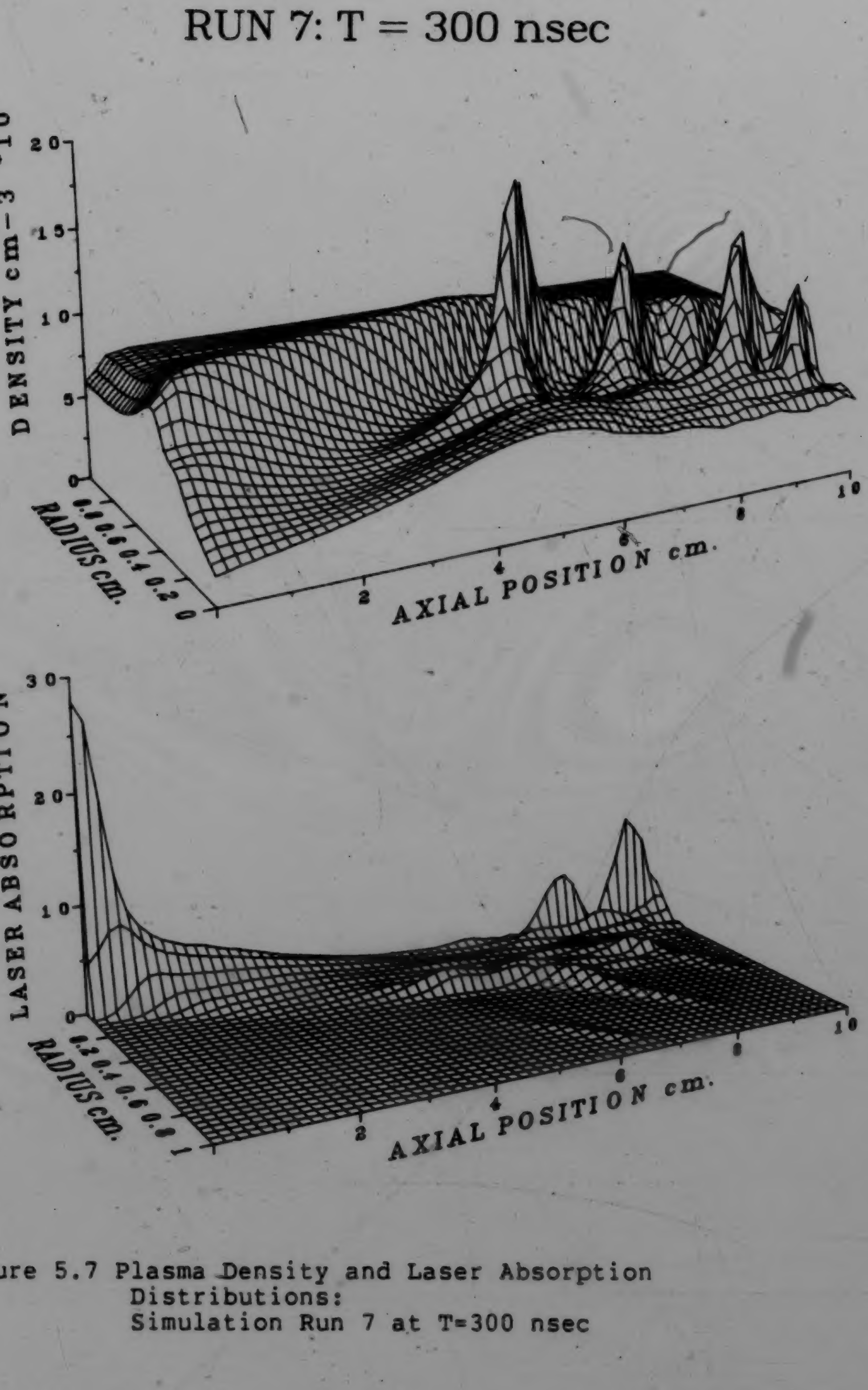

Figure 5.7 Plasma Density and Laser Absorption Distributions: Simulation Run 7 at T=300 nsec

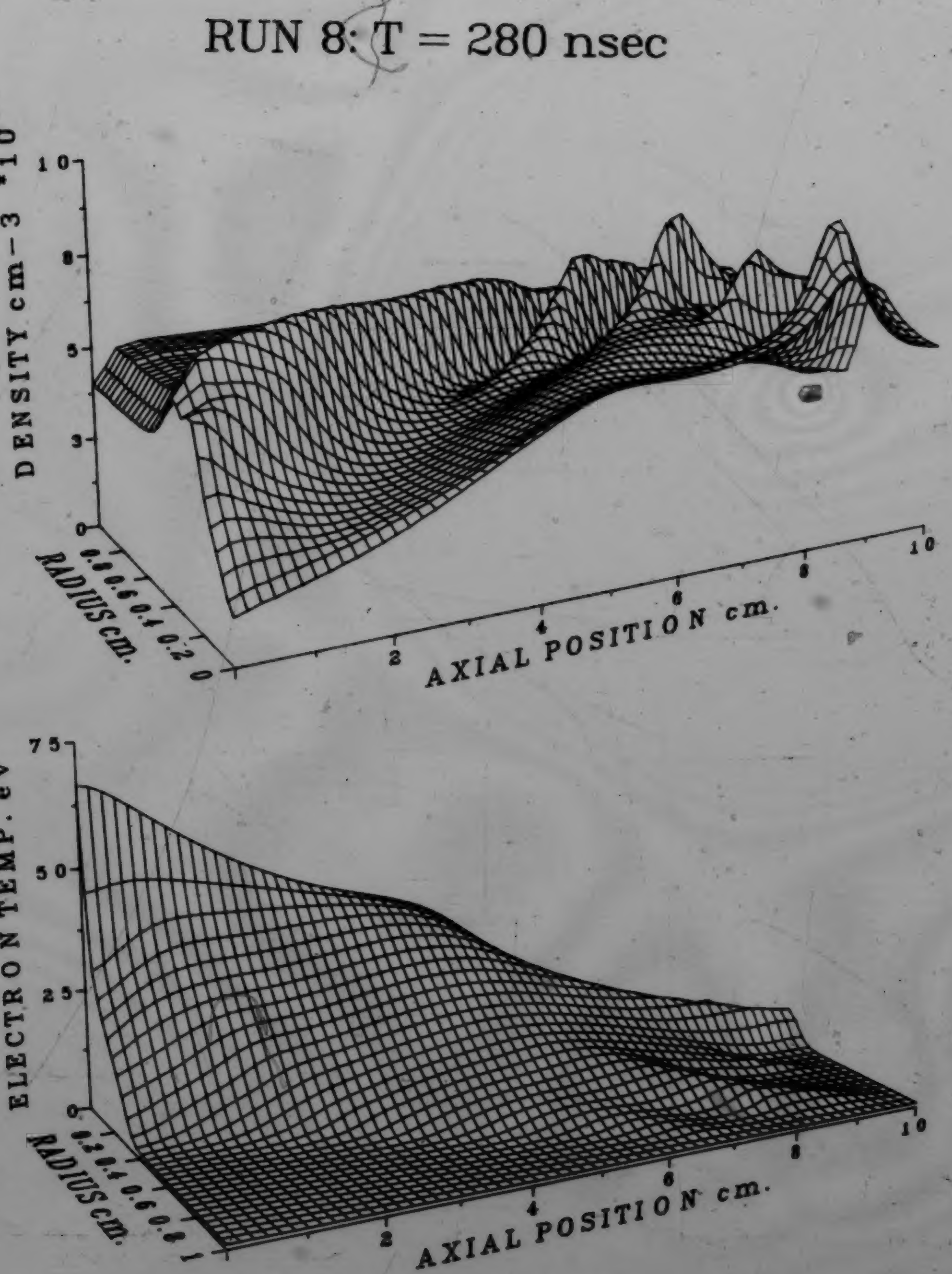

Figure 5.8 Electron Temperature and Density Distributions: Simulation Run 8 (lower initial density)

for a slight increase in the radial extent of the column and slight decrease in the plasma temperature.

Figure 5.9 shows the temperature and density distributions for higher initial density conditions. The effect of the increased collisionality is clear. The radial expansion has been significantly inhibited and the temperature has consequently risen. The higher initial density has resulted in a smoother density distribution.

Finally, Figure 5.10 and Figure 5.11 display the electron and ion temperature distributions and the electron density and the laser absorption distributions under the conditions of f/15 focussing.

These plots are very typical of all runs using f/15 focussing. They are characterized by a narrow, very uniform plasma column. At early times, the temperatures are significantly higher than those found with f/5 focussing, particularly near the central axis. This is due to the decreased expansion of the column and strong confinement of the laser near the axis.

5.4 Simulation Results, 2-D Profiles

The temporal variations of the plasma parameters are not easily discerned from the 3-D plots. These are most clearly seen through 2-D axial and radial profiles.

In each graph presented in this section, several profiles of the particular parameter, taken at different times in the simulation, are displayed. The time of each

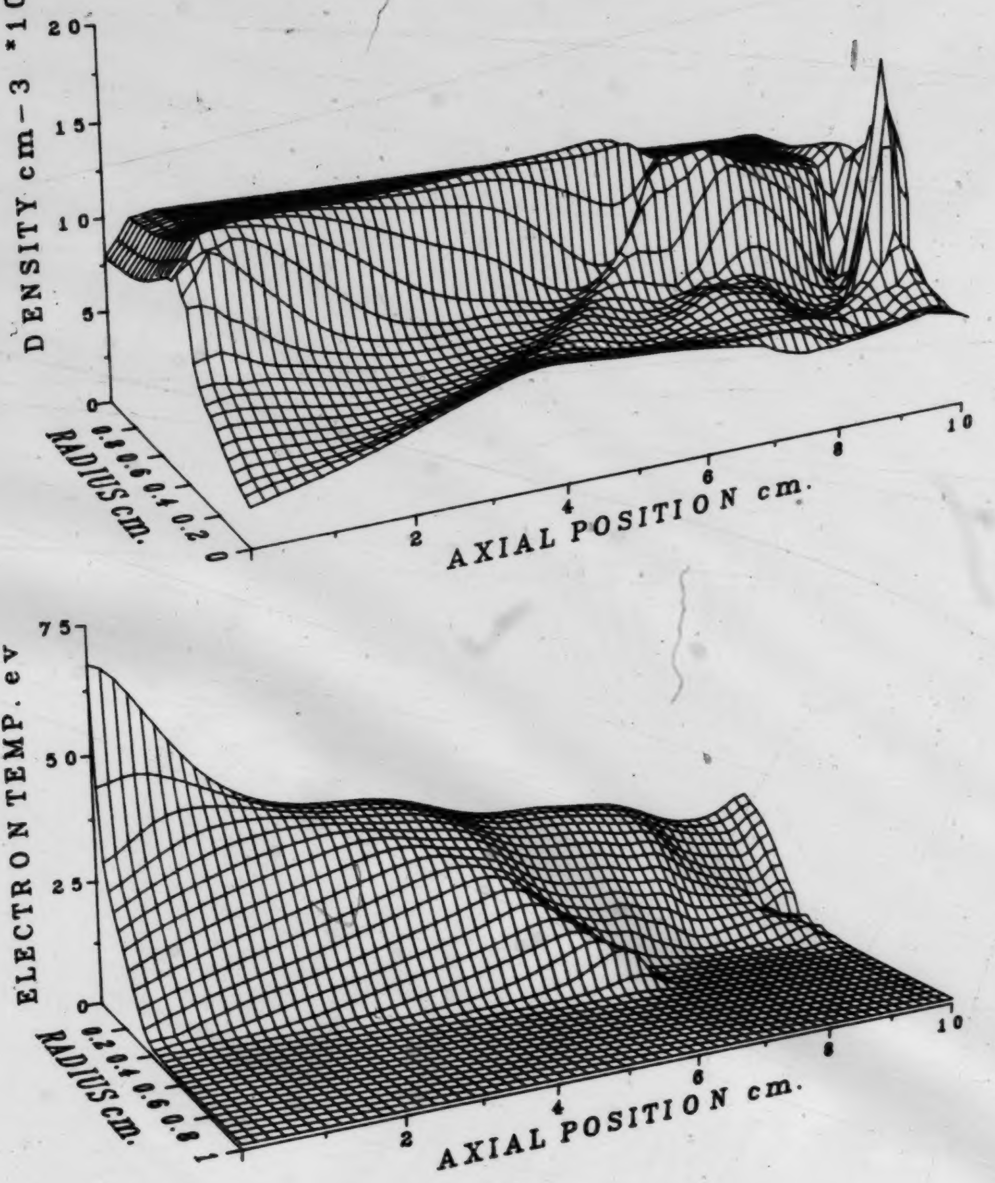

RUN 3: T = 290 nsec

Figure 5.9 Electron Temperature and Density Distributions: Simulation Run 3 (higher initial density)

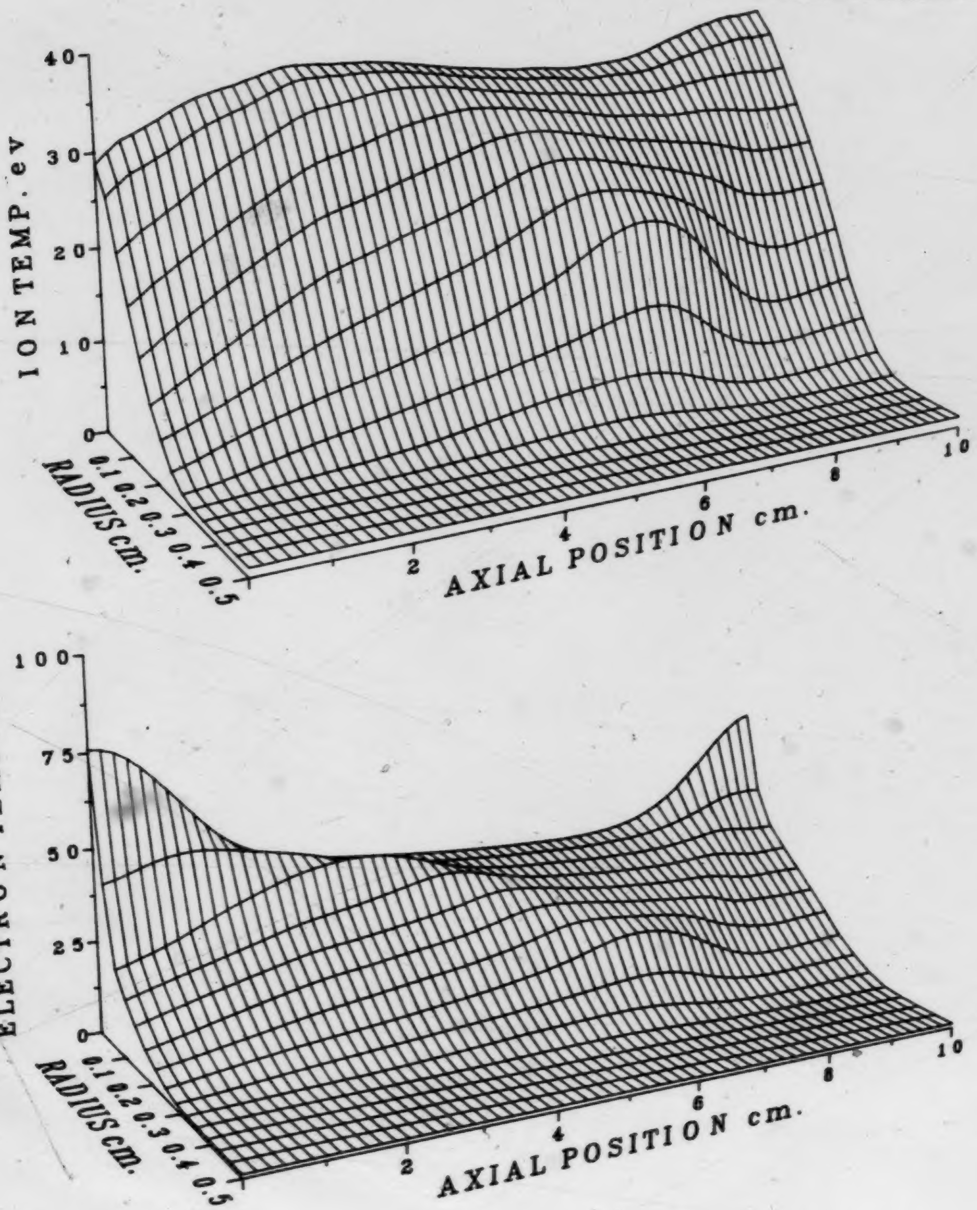

RUN 11: T = 300 nsec

Figure 5.10 Electron and Ion Temperature Distributions: Simulation Run 11 at T=300 nsec

RUN 11: T = 300 nsec

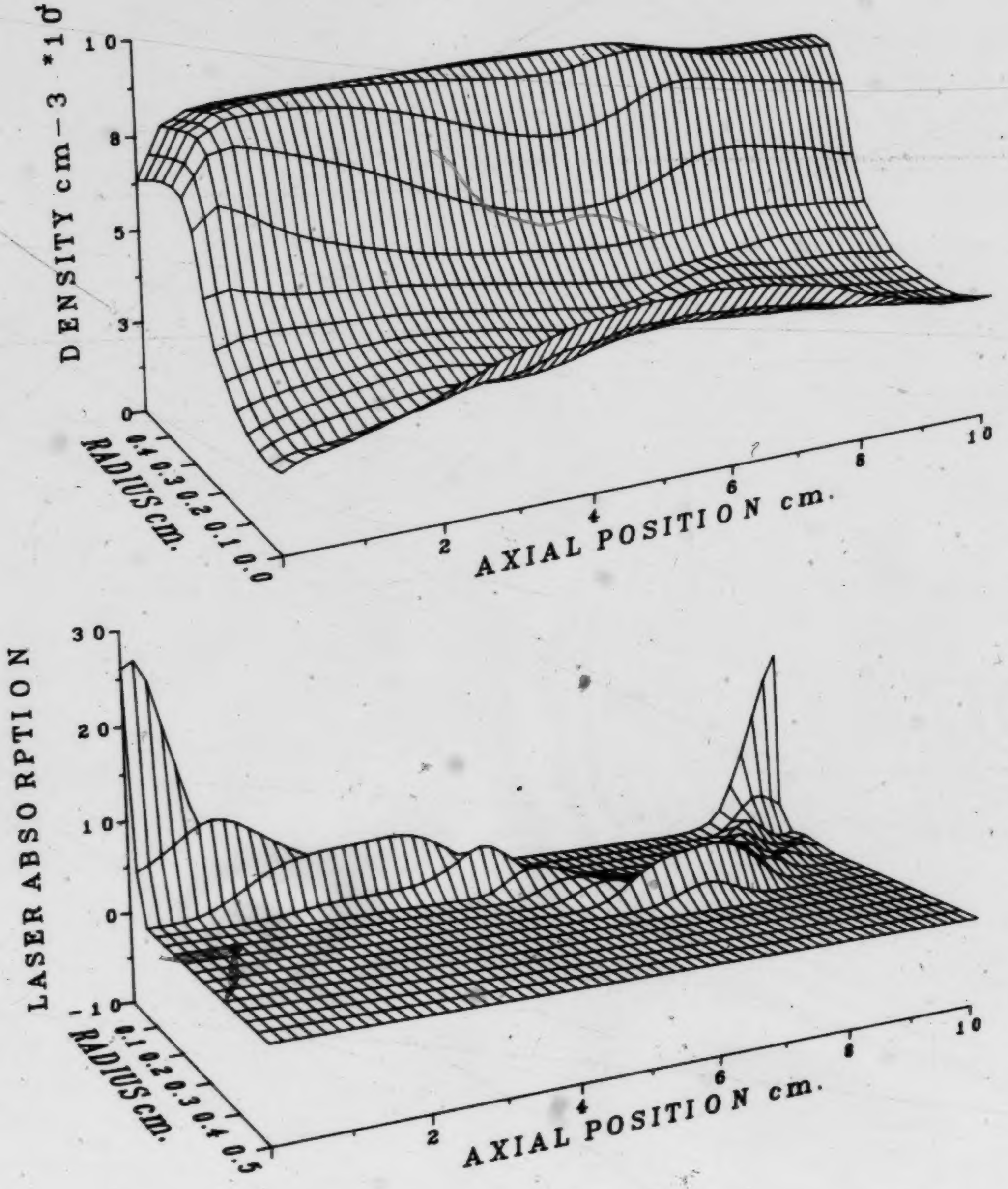

Figure 5.11 Plasma Density and Laser Absorption Distributions:
Simulation Run 11 at T=300 nsec

profile is specified in the legend.

In the case of the axial profiles, the data are averaged over 4 radial grid positions corresponding to a distance of ~.20 cm. While some details of the physics may be lost by taking this average, it was performed in order that comparisons made with the experimental data would be more consistent. Most of the axial information obtained from the experiments involved radial integration to some degree. In particular the Thomson scattered data was averaged over a radial distance of ~.20 cm and the axial streak data over virtually the entire column radius.

5.4.1 Axial Effects

Figure 5.12 shows axial profiles of the electron temperature and density for Run 5.

One effect of the axial average is immediately apparent. From the 3-D plot, it was clear that the electron temperature was maximum at the laser focus, at z=0. The radial drop-off is, however, so rapid that, on averaging, the peak shifts to an axial position of z≃2.5 cm.

Both the temperature and density profiles show the propagation of the plasma front. The temperature profiles demonstrate the process particularly clearly and velocity values are taken from these curves.

The temperature profiles also show the relaxation of the plasma temperature behind the front. By the 300 nsec point the temperature is very uniform and at a level of

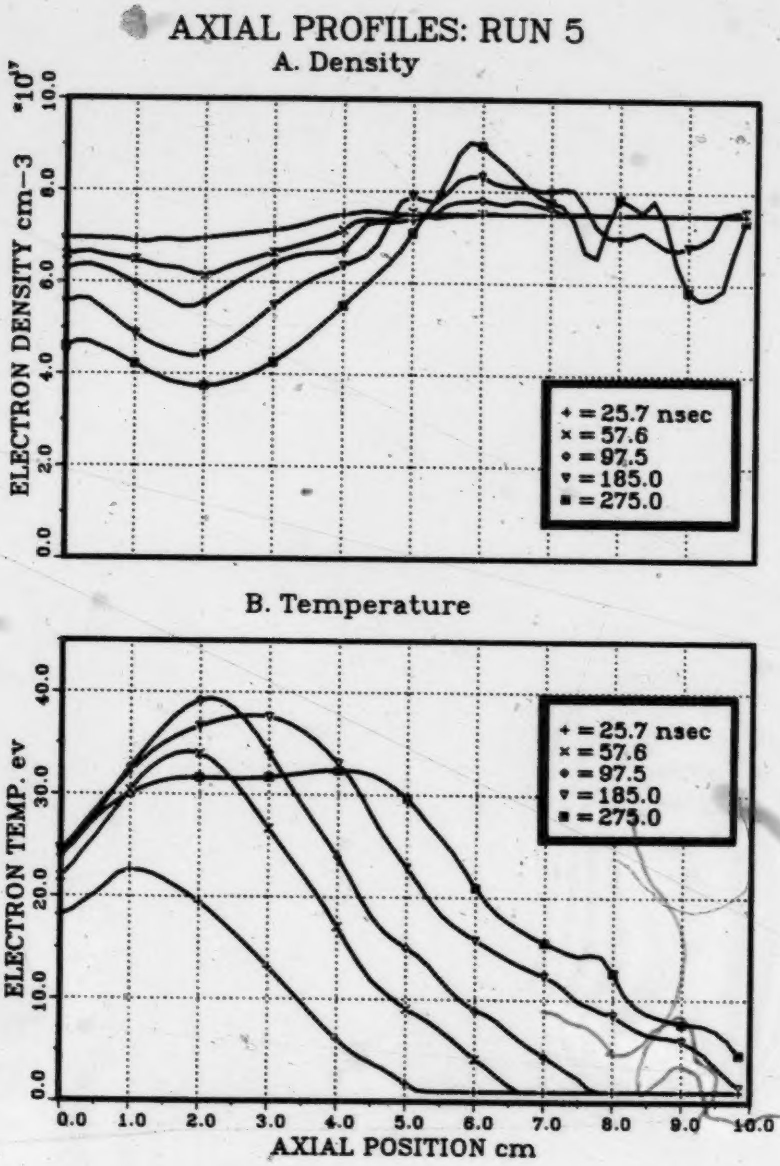

Figure 5.12 Axial Profiles of Temperature and Density for Simulation Run 5

30 eV. This is in very good agreement with the late time Thomson scattering result of 25 eV.

It is of interest to compare the axial behaviour of Run 5 and Run 2, displayed in Figure 5.12 and Figure 5.13 respectively. The major difference between Run 5 and Run 2 is the initial plasma density. There is, however, very little change in the axial behaviour. This is shown clearly in Figure 5.14 where the position of the plasma front is plotted versus time for each case. The location of the front was defined as the 20 eV level on the temperature profile.

Before comparing these two cases more closely, the temporal dependence of the front propagation will be examined. A log-log analysis of the curves yields a temporal power dependence of .58 ± .02 for Runs 5 and 8, and .57 ± .02 for Run 2. This is in good agreement with the .6 value associated with the 1-D bleaching wave and the experimental value of .66 ± .15.

The velocity of the plasma front taken from 150 to 300 nsec, where it has become fairly uniform, for Run 5 and Run 2 are 8.55 cm/μsec and 8.45 cm/μsec respectively. This is also reasonably consistent with the typical value of 6.9 ± .3 cm/μsec observed in the experiment.

There is an interesting effect on the propagation velocity with the magnitude of the applied field. Run 2 has an applied field of 75 kG while Run 8 has an applied field of 40 kG. All other parameters are the same. The axial

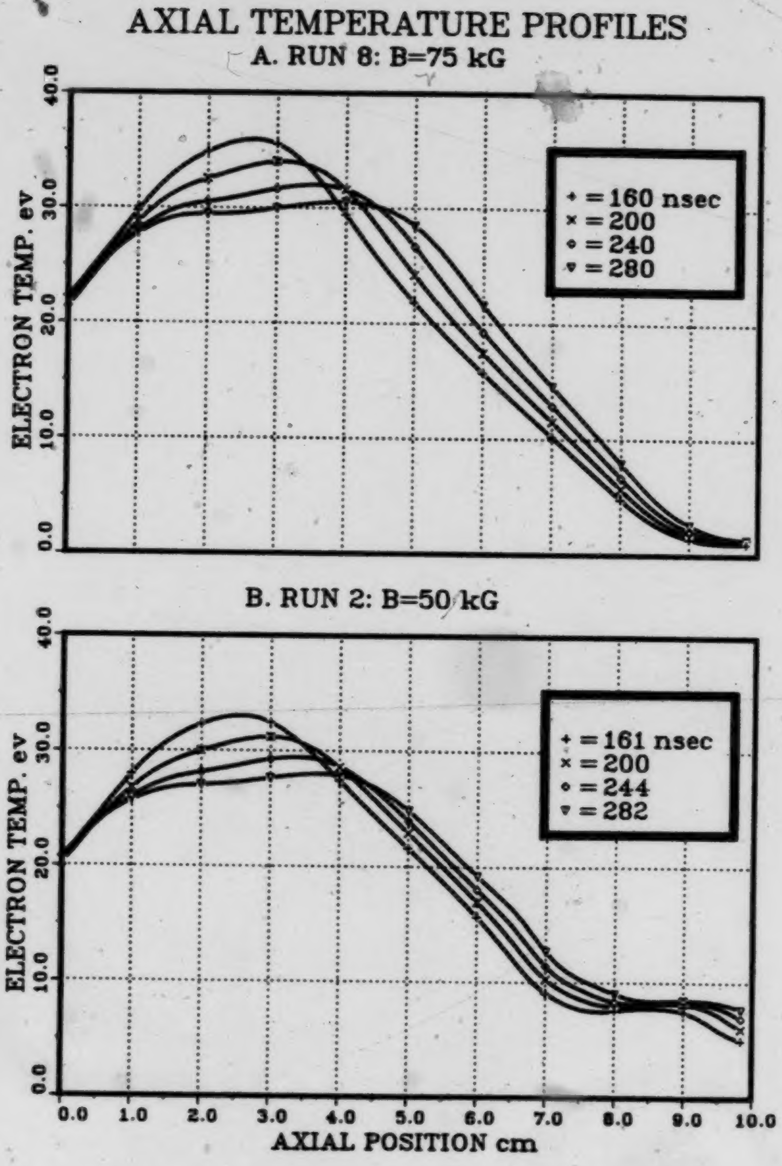

Figure 5.13 Axial Profiles of Temperature for Simulation Runs 2 and 8

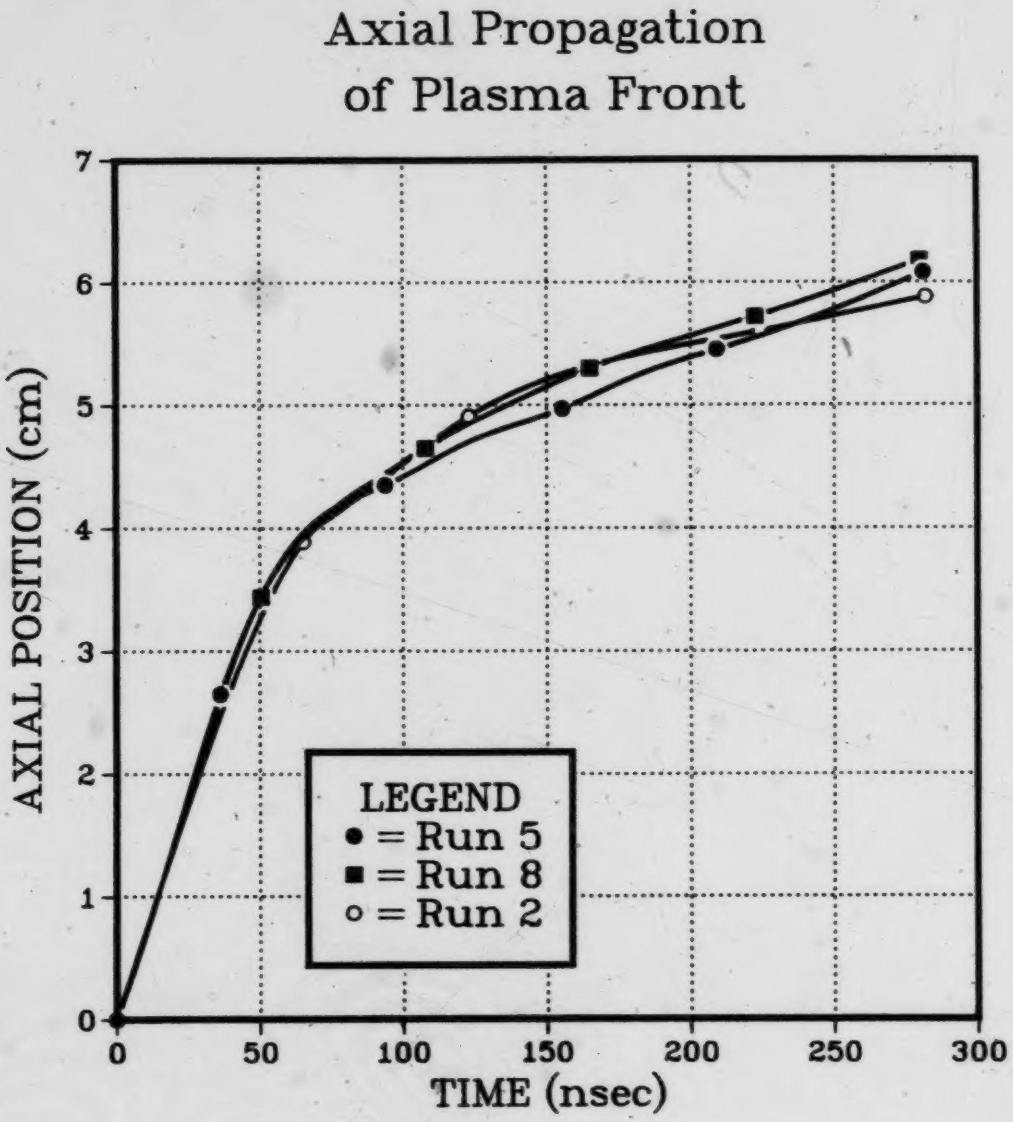

Figure 5.14 Axial Propagation of Plasma Front: Simulation Runs 5, 2 and 8

profiles for these runs are shown in Figure 5.13. With the reduction in field strength there is a reduction in temperature and a very significant reduction in propagation velocity. These effects are presumably attributable to the increased plasma expansion and subsequent reductions in laser intensity and plasma temperature.

Aside from the temporal dependence, the velocity should, from the bleaching wave model, have a dependence on density and intensity. From the 1-D model, the dependence is such that the ratio of velocities for 2 runs should be given by,

$$V_1/V_2 = (I_1/I_2)^{(3/5)} \cdot (N_2/N_1)^{(7/5)} \qquad (5.1)$$

The densities and intensities used in this expression are not the initial values but rather values averaged behind the front. These values were determined for Runs 5, 2 and 8. They are presented in Table 5.2. Using these values in equation (5.1), a comparison between a calculated velocity ratio and a measured velocity ratio can be made.

In the case of Runs 2 and 5, the measured ratio is $V_2/V_5=.66$ while the calculated ratio is $<V_2/V_5>=.73$. For Runs 2 and 8, the measured ratio is $V_2/V_8=.69$ while the calculated ratio is $<V_2/V_8>=.74$. Finally, for Runs 8 and 5, the measured ratio is $V_8/V_5=.97$ while the calculated ratio is $<V_8/V_5>=.97$. In all cases the agreement is very good.

In terms of the actual position of the front, the agreement with experiment is not quite as good. At the 300 nsec point, experiment shows the front to be at an axial

Table 5.2 Average Parameters behind Axially Propagating Front

RUN	AVG. DENSITY (units	AVG. ENERGY are	AVG. RADIUS arbitrary)	AVG INTENSITY	VELOCITY
5	7.2	1.5	.53	5.36	8.41
8	4.8	1.0	.71	2.00	8.16
2	4.3	.50	.73	0.94	5.59

position of $z \simeq 3.5$ cm. The simulation shows the front to be considerably further along at a position of $z \simeq 5.0$ cm. This variation may be due to the fact that in the simulation the plasma is initially fully ionized and at a temperature of 1 eV while no direct pre-ionization was provided in the experiment. The actual definition of the plasma front is also somewhat arbitrary. In experiment, the leading edge is defined by a position of strong light emission. In the code, the leading edge was defined as the 20 eV level on the temperature profile. This may also account for the discrepancy.

Finally, the effect of changing the focussing ratio on the axial behaviour is examined. In Figure 5.15, the axial profiles for Run 15 are presented. While the only parameter change between this run and Run 5 is the f/ratio of the incoming laser, there is a very significant change in the form of the axial profiles.

The temperature profiles of Figure 5.15 are fairly uniform along the axis and, unlike the previous results, do not display the propagation of a front. The temperature values in the first 200 nsec are considerably higher than those found experimentally. Beyond this point the plasma cools to levels of 40-60 eV which are in better agreement with the measured values.

The density profiles show that the density along the axis drops very rapidly and uniformly from the initial value of $7.5 \cdot 10^{17} cm^{-3}$ to a level near $4.0 \cdot 10^{17} cm^{-3}$. The density

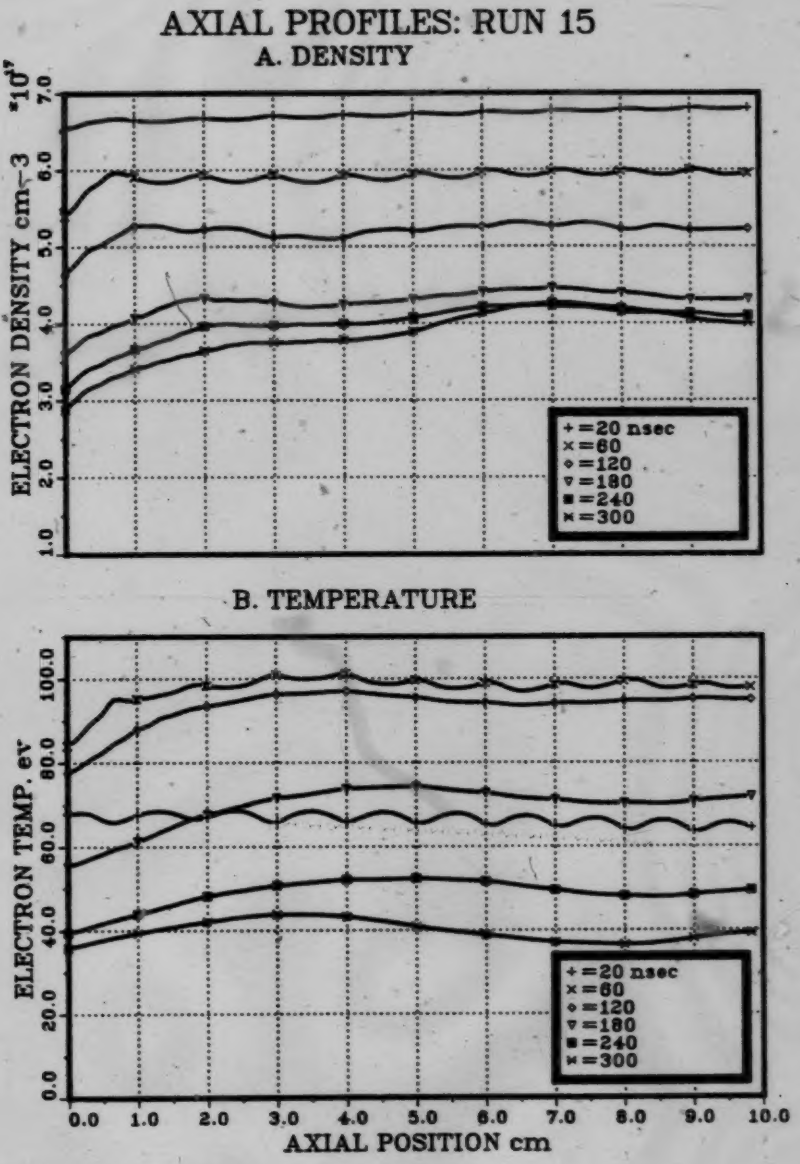

Figure 5.15 Axial Profiles of Temperature and Density for Simulation Run 15

scale lengths are easily long enough to satisfy the inhomogeneity criterion of the SRS instability. There is, however, no indication of a delay in the formation of these long scale lengths unlike that seen in the experimental data. This suggests that with a suitably intense incident wave, SRS may be generated prior to the long delay time found in the experiment. However, as is discussed below, ionization effects may be important in establishing the time scales required for the plasma development.

At later times (>180 nsec) the profiles show the propagation of a density structure along the axis. The velocity (measured from the $3.5 \cdot 10^{17} cm^{-3}$ level) is determined to be ~20 cm/μsec. This rather high velocity does not entirely remove the possibility of a heating wave mechanism, however, a matching structure propagating in the temperature profiles would be expected but is not seen.

When comparing the simulation results with the experimental results under conditions of f/15 focussing, there are some inconsistencies. Notably, the core temperatures found in the simulation are considerably higher than those measured experimentally. These temperatures arise from very strong trapping of the laser along the central axis. The use of a more precise calculation grid for the laser did not significantly alter this effect.

Another difference between the code and experiment is the lack, in the code, of an axially propagating heating front. The use of a longer column in the simulation might identify such a front located beyond the 10 cm point. Nevertheless, even over distances of 10 cm the experimental data showed the clear temporal development of the plasma column.

Ionization effects were ignored in the code and these may affect the modelling. Scudder (1979) suggested that the thermal conduction of electrons from the plasma into the un-ionized gas was the most likely mechanism to provide ionization ahead of the front. It was further noted that this process would decrease the propagation velocity of the plasma front. A more consistent model of the axial behaviour of the plasma column may require the inclusion of these ionization processes.

5.4.2 Radial Effects

Radial profiles, taken at particular axial locations, were generated from the simulation runs in order to examine the radial behaviour of the plasma column.

Figure 5.16 shows the radial profiles for Run 5. In this case the initial density was $7.5 \cdot 10^{17} \mathrm{cm}^{-3}$, the field strength was 75 kG and the laser focal ratio was f/5. To match the experimental conditions, the profiles were taken at an axial location of $z \simeq 3.0$ cm.

The formation of a density minimum on axis is seen immediately. With time the column expands radially and the magnitude of the density on the outer edge of the column increases. At t=275 nsec the ratio of the maximum to minimum

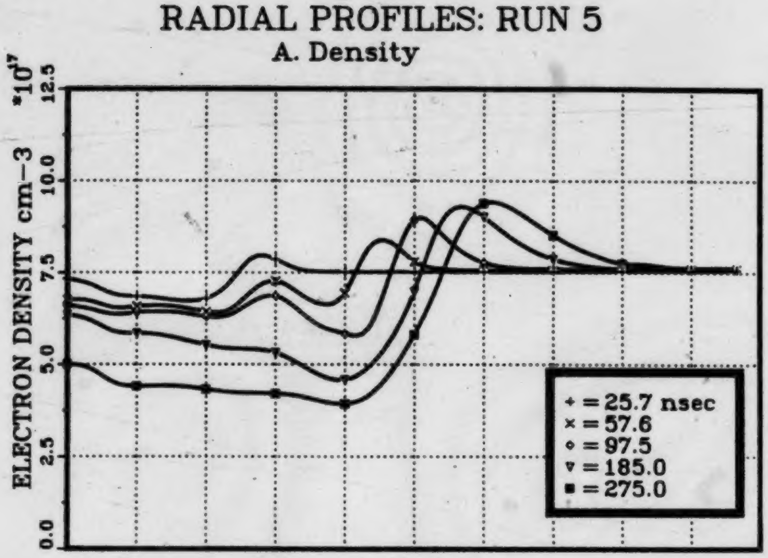

RADIAL PROFILES: RUN 5

A. Density

B. Temperature

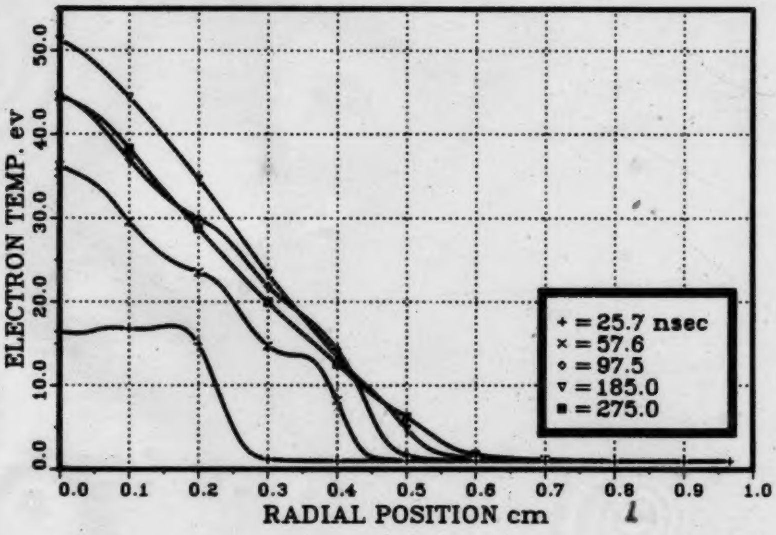

Figure 5.16 Radial Profiles of Temperature and Density for Simulation Run 5

density has reached a value of 1.8 which agrees well with the average value of 2.0 ± .6 obtained from experiment.

The temperature profiles also show the expansion of the column. Initially the plasma is quite uniformly heated to ~17 eV. The temperature then rises rapidly, particularly on the central axis. At t=185 nsec a maximum of ~50 eV has been reached. From this point the plasma slowly cools.

In Figure 5.17, the radial profiles for Run 15 are given. Note that the x-axis has been expanded in this graph. This run differs from Run 5 only in the value of the f/ratio which in this case is f/15. To match experimental conditions, the profiles were taken at an axial position of $z \simeq 4.5$ cm.

As before, the density minimum forms immediately. The plasma, again, expands radially although the radial extent achieved is significantly less than that reached in Run 5. The density ratio is relatively uniform at a value of ~2.5 which is higher than the previous value but is still in fairly good agreement with experiment.

With t<200 nsec the temperatures along the central axis were found to be in the range 200-250 eV. Even when averaged over several radial positions these temperatures are far higher than those observed experimentally. As discussed earlier, this is due to the strong confinement of the laser on the central axis.

A plot of the radial position in time for the two cases discussed is given in Figure 5.18. This plot can be compared

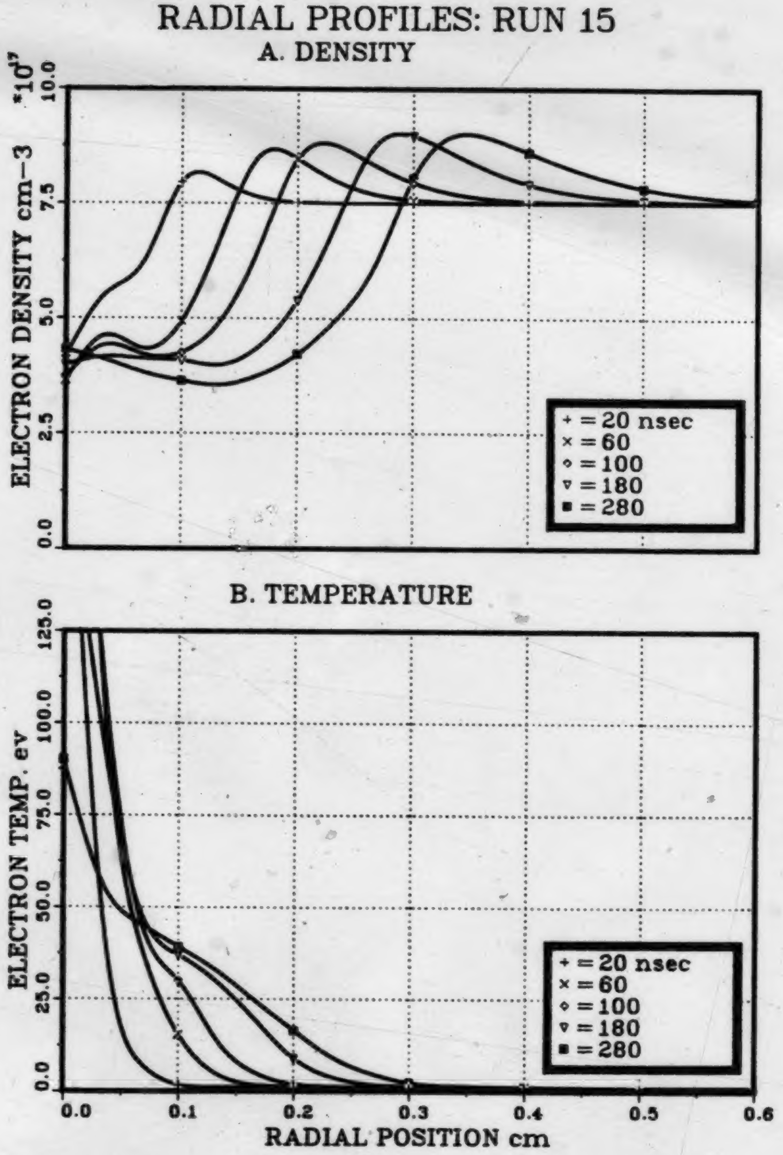

Figure 5.17 Radial Profiles of Temperature and Density for Simulation Run 15

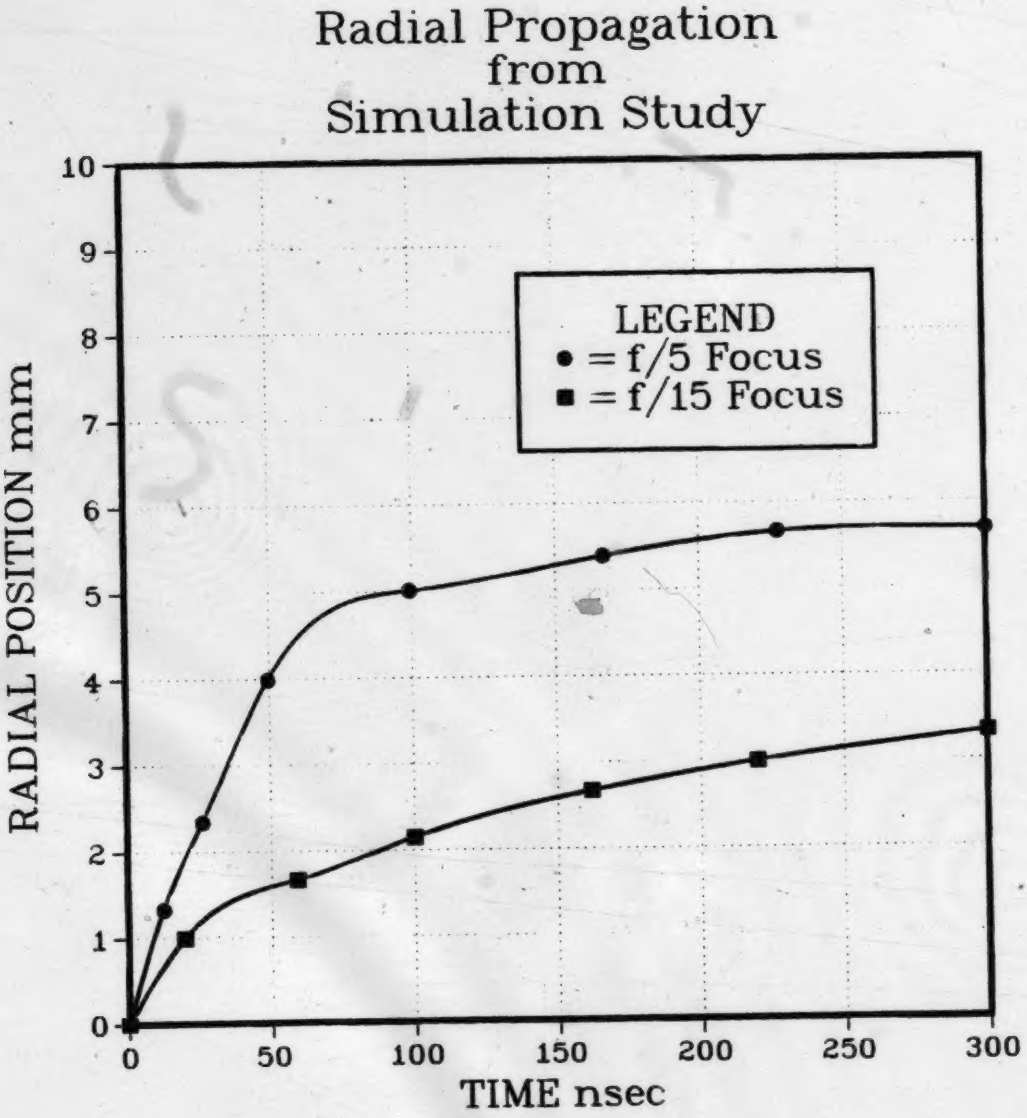

Figure 5.18 Radial Propagation of Plasma Column: Simulation Runs 5 and 15

directly with the experimental results given in Figure 4.6. The agreement both qualitatively and quantitatively is excellent. The effect of the f/ratio on the radial expansion rates and overall radial extent of the plasma column is very well supported by the simulation.

The effect of the magnetic field on the radial behaviour is shown in Figure 5.19. There are some small changes in the shape of the density profile, however, the major effect of increasing the magnetic field is to reduce the radial extent and the radial expansion rate of the plasma column. With a change in field strength of 50%, the effects are not overly dramatic.

Simulations were attempted in which no magnetic field was applied in order that comparisons could be made with the experimental data. The simulation, however, proved unstable when the magnetic field strength was reduced below ~40 kG.

Finally, the simulation results can be used to support the discussion of the anomalously low temperature measured at early time by Thomson scattering.

Figure 5.20 shows the simulated plasma temperature and density at an axial position of ~1.5 cm at times of t=60 nsec and t=300 nsec. This matches the conditions of the Thomson scattering experiment. The radial extent shown here is only .30 cm; the experimental data was averaged over ~.20 cm.

For t≈300 nsec the density and temperature over the probed region is fairly uniform and is in good agreement

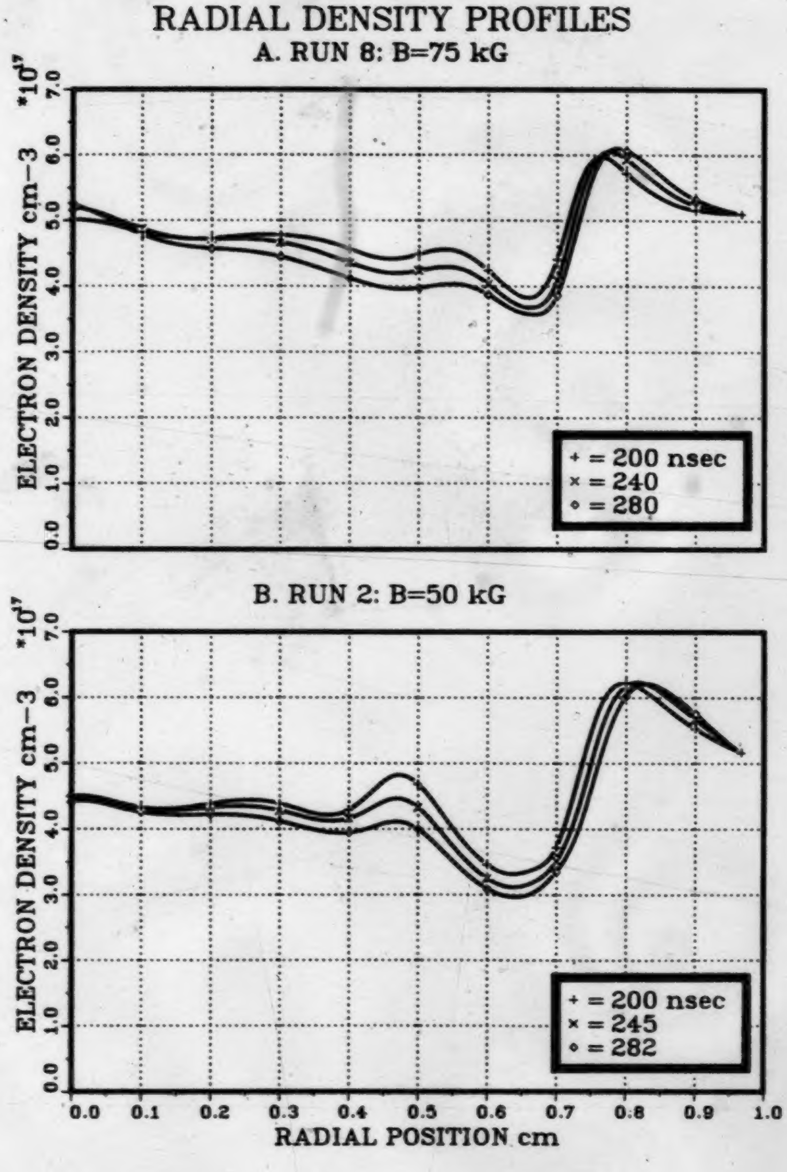

Figure 5.19 Radial Profiles of Density for Simulation Runs 8 and 2

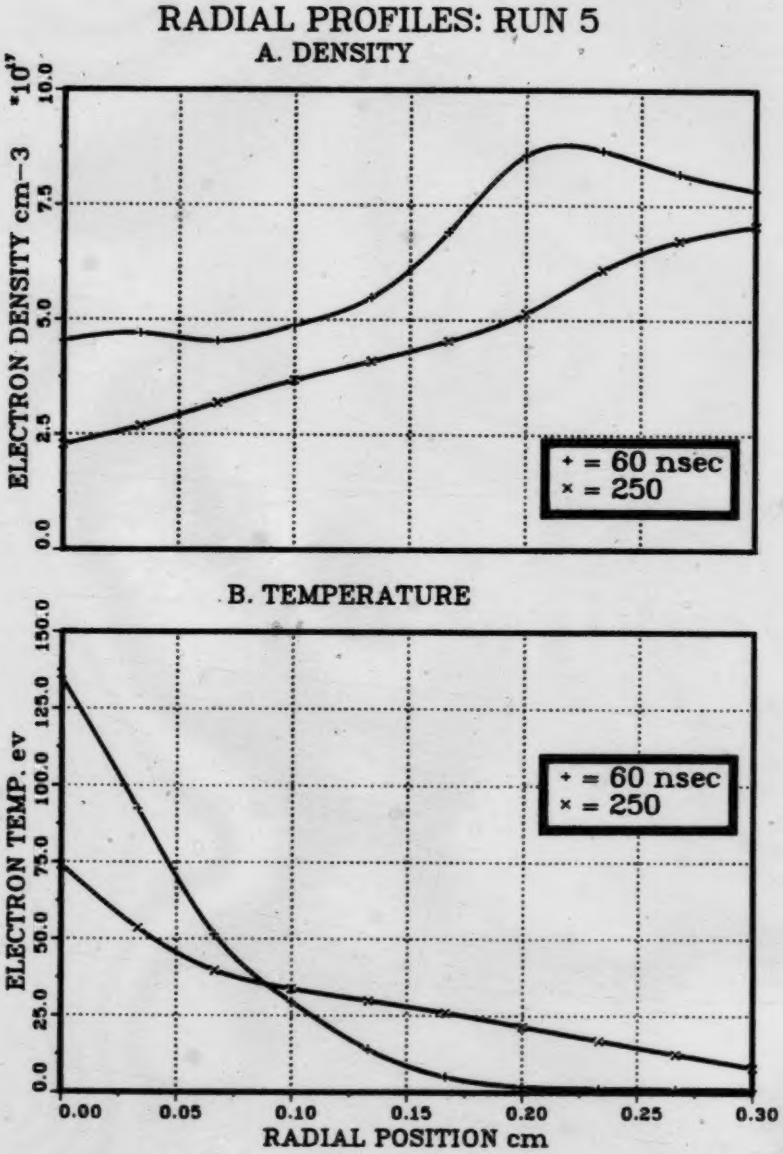

Figure 5.20 Radial Profiles indicating Thomson Scattering Experimental Conditions from Simulation Run 5

with the experimental data.

For t≃60 nsec, it is clear that the high temperature region is extremely limited radially. Within the region probed, approximately half the plasma is very cold and has a correspondingly higher density. This would certainly result in a measured temperature lower than the core temperature and may explain the anomalously low value obtained.

5.5 Concluding Remarks

The radial plasma behaviour and, in particular, the dependence of this behaviour on the focal ratio of the incoming laser beam were very well supported by the simulation results. The bleaching nature of the axial propagation was also well supported however, some aspects of the axial behaviour were not totally consistent. This may have been due to the lack of ionization effects in the code. In both the general form of the density profile and the maximum to minimum density ratio, the experimental and the simulation results were found to be in good agreement. The simulation temperatures are typically higher than the values measured experimentally but integration effects involved in the measurements are not precisely known, making detailed comparisons difficult.

CHAPTER VI

Summary and Conclusions

6.1 Preliminary Remarks

In this chapter the main results of the experiments and the numerical simulation will be summarized and conclusions will be drawn. Suggestions for further research will be given.

6.2 Summary of Results

Figures 6.1 and 6.2 present some typical results from the experiments, simulations, and theoretical models. In general, simulation parameters closely match the experimental conditions. There are, in some cases, significant variations in the magnetic field strength, however, it has been seen that for early times ($t<300$ nsec) this is not a dominant factor in describing the plasma behaviour.

6.2.1 Axial Propagation

Over a wide range of experimental conditions, plasma column lengths from 10 - 30 cm were observed. The column was found to develop axially in time with a dependence of $\sim t^{.66}$, which agreed well with the expected power dependence for a bleaching wave.

A typical value for the axial propagation velocity of the plasma front over the first microsecond was found to be

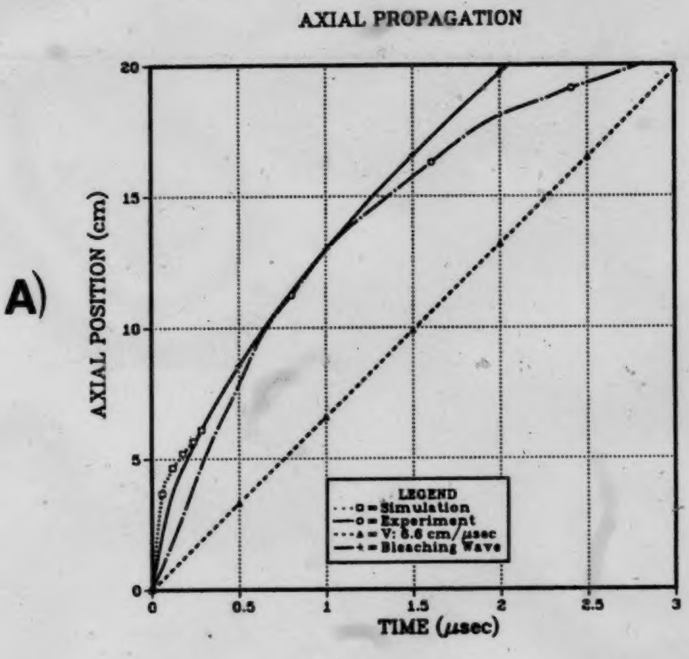

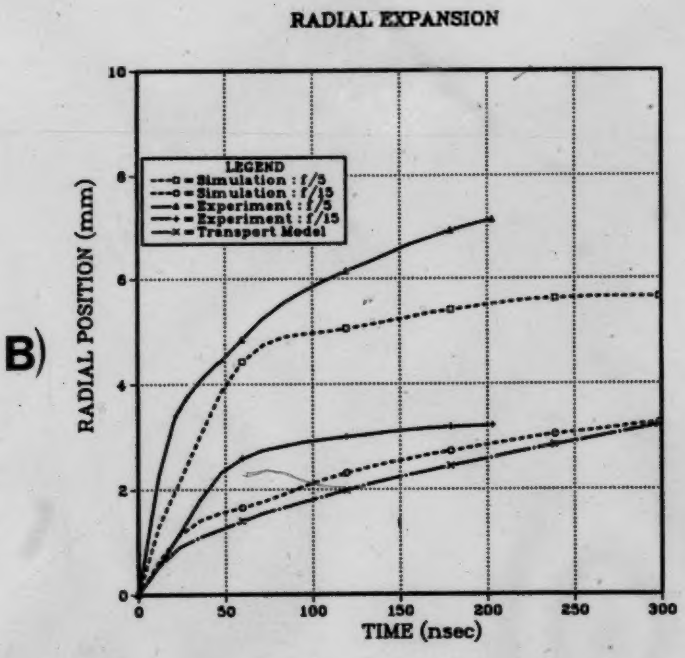

Figure 6.1 Summary of a) Axial and b) Radial Plasma Dynamics.
Experimental, Modelling, and Theoretical Conditions are Described in the Text.

A)

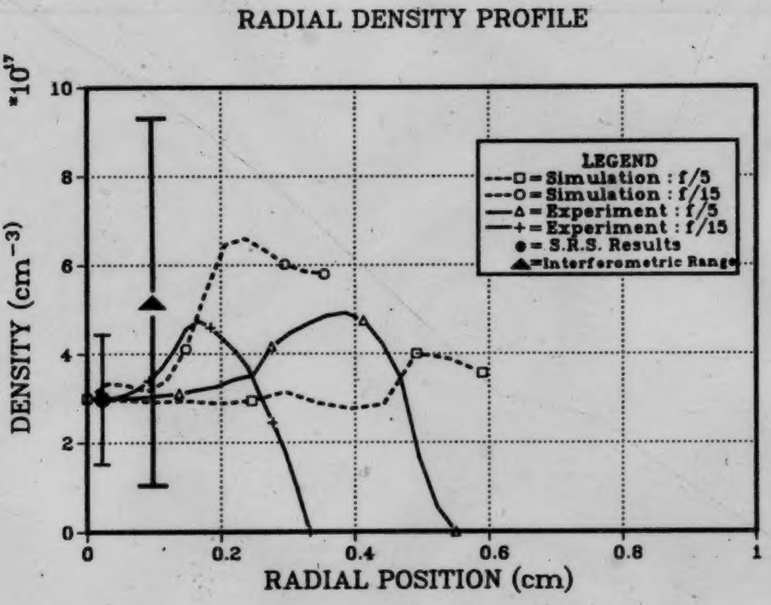

B)

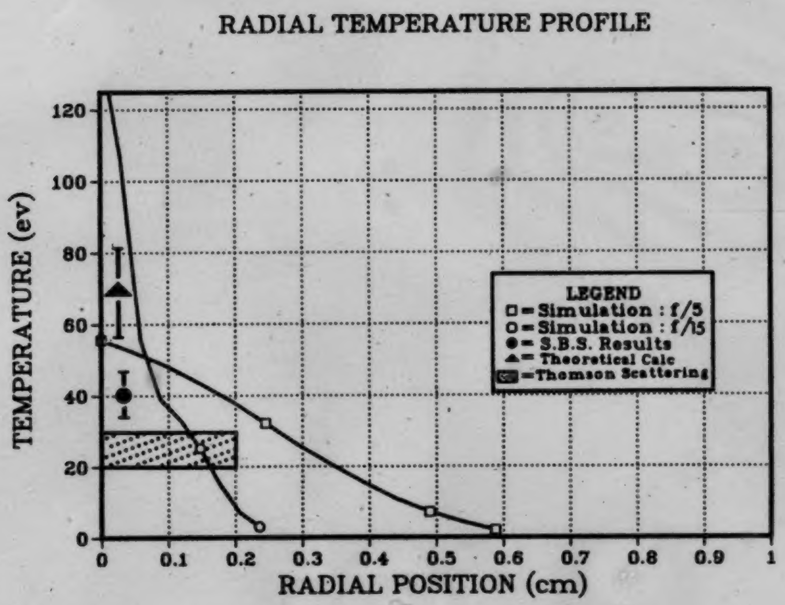

Figure 6.2 Summary of a) Density and b) Temperature Characteristics of the Plasma Column. Experimental, Modelling, and Theoretical Conditions are Described in the Text.

6.9 ± .3 cm/μsec. The dependence of the velocity on plasma density and laser intensity was shown to follow the expected dependence of a bleaching wave.

With parameters closely matching the experimental conditions, the simulation results provided very consistent results. A heated plasma column was found to propagate axially with a temporal dependence of $t^{.55}$. The velocity became quite uniform during the period 150<t<300 nsec, yielding a value of ~8.5 cm/μsec. Both of these results are in good agreement with the experimental results.

Even though 2-dimensional effects were expected to significantly alter the axial propagation, the density and laser intensity dependence was found to be consistent with the 1-D bleaching model.

In Figure 6.1-a, these aspects of the axial propagation of the plasma column are summarized. The experimental curve was obtained from data from the split-solenoid, with f/5 focussing, a fill pressure of ~20 torr and a laser energy of ~400 joules. The bleaching-wave curve was generated from the Burnett and Offenberger(1975) self-regulating model. A density of $8.\cdot 10^{17}$ cm^{-3} and an intensity of $5\cdot 10^{8}$ W/cm^{2} (appropriate to the above experimental conditions) were used in generating this curve. The simulation result was taken from Run 5 (f/5 focus, initial density of $7.5\cdot 10^{17}$ cm^{-3}, magnetic field strength of 75 kG, and laser energy of 120 J). The constant velocity curve represents the minimum velocity expected from the optical detonation model of

Ahlborn et al(1982).

In the simulation study, an increase in the magnetic field strength resulted in an increase in the axial velocity. Although there was no direct attempt to examine this effect in these experiments, Offenberger and Burnett(1975) did find such a correlation.

In using a large focal ratio (f/15) for the input laser, the code did not indicate any propagation since the plasma front very rapidly extended beyond the 10 cm simulation length. The lack of ionization effects in the code is presumably responsible for this disagreement with the experimental observations.

Nevertheless, from the above evidence it seems reasonable to conclude that during the early time period ($t<1\mu$sec) the axial propagation of the plasma column may be characterized as a bleaching wave. Beyond this period the temporal dependence remains much the same even though the laser energy is no longer available. It seems likely that the axial wave has been transformed into a blast wave, which has the same temporal dependence as the bleaching wave. Verification of this transformation would require more detailed experiments, simulations and theoretical analysis.

6.2.2 Radial Behaviour

The most significant result in the analysis of the radial behaviour of the plasma column was the dependence of the radial expansion rate and extent of the column on the focussing ratio of the incoming laser.

With f/15 focussing, the column was observed to expand initially at rates of ~4.5 ± 1.2, cm/μsec. This decreased to ~.82 ± .30 cm/μsec by the 300 nsec point where the radial extent was ~2.5 mm.

With f/5 focussing, the column was observed to expand at rates of initially ~9.0 ± 1.5 cm/μsec, decreasing to ~1.2 ± .4 cm/μsec, out to a radial extent of ~5.0 mm.

The simulation study strongly supported the f/ratio effect on the radial behaviour. Both qualitative and quantitative agreement was excellent.

With faster laser focussing-defocussing, laser energy absorption is quite high in the outer regions of the column. This results in faster heating in these regions which in turn leads to greater radial expansion of the column. With longer focal lengths the heating is restricted to the core and expansion is due primarily to radial ion transport.

These aspects of the radial behaviour are summarized in Figure 6.1-b. The results from the experiment (f/5 and f/15 focussing), the simulation (f/5 and f/15 focussing) and the ion transport model are shown. All results included a confining magnetic field (50-70 kG for the experimental curves, 75-80 kG for the simulation curves and 50 kG for the theoretical curve). The experimental curves were obtained with fill densities of 10-15 torr and laser energies of ~200 joules. The simulation results were obtained with an initial density of $7.5 \cdot 10^{17}$ cm^{-3} and a laser energy of 120 joules. A density of $3 \cdot 10^{17}$ cm^{-3} was used in the ion transport model.

Experimentally, increasing the magnetic field strength was seen to reduce the radial expansion, as expected. The effect was not seen to be too dramatic over the initial 300 nsec. For the plasma densities of the experiment, the ion collision rate strongly affects the radial expansion and reduces the confining effect of the magnetic field.

6.2.3 Plasma Density and Temperature

6.2.3.1 Density

Radial density profiles were used in analyzing the radial behaviour of the plasma column but, of course, also provided detailed information concerning the plasma density behaviour.

In many cases it was possible to determine a finite time over which full ionization was achieved. Ionization times were observed in the range of $t_i<10$ nsec to $t_i \sim 25$ nsec. These are in good agreement with a calculated range of $5<t_i<35$ nsec which was based on the Raizer(1977) description of laser-induced gas breakdown.

In virtually all cases, a density minimum on axis was clearly established. Data near the front showed that the density minimum is normally formed very rapidly in times $\lesssim 10$ nsec. On average, a value of ~2. ± .6 was found for the ratio of the maximum to minimum density.

The simulation code did not include the Nernst-Wienecke effect which alters the core density. Nevertheless, the simulation yields density profiles which are in very good agreement with the data. Note, however, that in the experimental situation the outer regions of the column consist of un-ionized hydrogen ($n_e=0$) unlike the code which assumes a fully ionized 1 eV hydrogen plasma.

The results of the code indicate that the density minimum is established instantly. Density ratios from ~2 to ~2.5 were seen to develop.

Figure 6.2-a shows typical radial density profiles from both experiment and simulation for both f/5 and f/15 focussing. The experimental profiles were taken at axial locations of 1 cm for f/5 focussing (~190 nsec after the initial breakdown) and 4.5 cm for f/15 focussing (~180 nsec after the initial breakdown). In the f/5 case the confining field was 68 kG while for the f/15 case it was 42 kG. The simulation results were taken at times of ~100 nsec and at axial locations of 3 cm for f/5 focussing and 4.5 cm for f/15 focussing. In both cases the confining field was 75 kG. Included in this figure is the range of density values obtained from the interferometric measurements and also the range of values obtained from the analysis of the SRS spectra.

Density perturbations were observed both experimentally and in the simulations. The characteristics were, however, very different.

Near the center of the interference fringes, which are inverted to give the density profiles, short-lived disturbances were occasionally seen to develop. These were observed only with f/5 focussing and only near the focal region. Typically, scale lengths of ~.1 -.4 mm and lifetimes of ~50 nsec were observed.

From the simulation study, a number of high density regions were seen to develop, generally off the central axis and several cm from the focal region. These were also restricted to cases involving f/5 ratios. Scale lengths of ~.17 cm were observed and the structures were stable over the duration of the simulation (300 nsec).

Because of the large differences in the characteristics of these phenomena it is difficult to conclude that they are related. Indeed, further experimentation and analysis is required to obtain a precise understanding of these structures.

6.2.3.2 Temperature

Experimentally, two techniques were used to determine the plasma temperature.

By analyzing the SBS spectra, a plasma temperature of $T_e=T_i=45$ eV was obtained. The fitting of a theoretical model to the spectral shape is very sensitive to the electron-ion temperature ratio and proved to be a useful diagnostic in determining the plasma temperature.

Thomson scattering of a ruby laser was also used in determining the plasma temperature. Normally this is a useful diagnostic in that it provides good temporal and spatial resolution. In this case, however, the scattered signal was too weak and had to be integrated over a large spatial area. This led to an anomalously low temperature of ~12 eV at very early times (t<60 nsec). At later times (t~250 nsec), when the plasma column has expanded and the temperature is more uniformly distributed over the probed region, a temperature of ~25 eV was obtained.

The simulation study produced plasma temperatures in good agreement with the experimental values. Due to the high laser flux and, consequently, strong electron heating, the electron temperature distribution is peaked near the focal region. Outside of this region the electron and ion temperature distributions are virtually identical, indicative of rapid equilibration.

The temperatures along the central axis, the core temperatures, are noticeably higher than those observed experimentally. When averaged over a short radial distance the levels decrease to the range 20 - 40 eV, in good agreement with the measured values.

Figure 6.2-b shows simulation results of radial temperature profiles (for both f/5 and f/15 focussing) at times of ~180 nsec into the plasma development. The late-time Thomson scattering result (averaged over the region indicated) and the SBS results are included. The theoretical value obtained from energy balance calculations is also included.

6.2.4 Stimulated Scattering

The long interaction length provided in this experimental apparatus produced very high levels of both stimulated Brillouin (SBS) and stimulated Raman (SRS) scattering. Peak reflectivities of 20-25% were observed for SBS. These levels are in good agreement with a convective growth model. The instability saturated rapidly due to rapid electron-ion equilibration and subsequent strong ion Landau damping.

The SRS signals were observed with peak reflectivities of .7%. A measured threshold intensity level of $4 \cdot 10^{10}$ W/cm^2 was in good agreement with an absolute instability model. As with SBS, the instability rapidly saturated. The saturation was well explained by enhanced electron Landau damping due to a population of hot electrons produced by the SRS process itself.

6.3 Problems for Further Investigation

1.Axial Propagation

Although the axial propagation velocity of the plasma front was found to depend on the laser intensity and plasma density, a better definition of this dependence or a dependence on other laser and plasma parameters would require a larger data base. This could be established by making the determination of the front velocity a shot-by-shot diagnostic. This might be done by the placement of probes over the first few centimeters of the solenoid.

2.Plasma Temperature

The simulation results showed some interesting features in the temperature distribution. It would be useful to map the temperature both axially and radially, however, higher spatial resolution than that which was used in this study would be necessary. This might require a more powerful ruby laser light source.

3.Plasma Density

Fluctuations observed in the interferograms suggest the possibility of local perturbations in the plasma density.

Alternative density diagnostics and/or improved inversion techniques may provide a better characterization of this phenomenon.

4.Stimulated Scattering

The hot electron population used to explain the enhanced Landau damping and subsequent rapid saturation of the SRS instability was not observed experimentally.

More sensitive methods to detect the x-rays generated by these electrons would seem to provide the most likely approach to detecting them. It should not be necessary to apply an axial magnetic field in order to generate a plasma column sufficiently uniform to allow for the growth of the SRS instability. This would provide a less noisy environment for the use of sensitive detection equipment.

Furthermore, because of the damage caused by the feed-back of the SBS signal into the CO_2 laser cavity, an investigation of the stimulated scattering processes might be more easily done with two lasers. The first would be used to produce the plasma column and of inadequate intensity to generate SBS. The second would generate a single, short-lived, high intensity pulse which when incident on the pre-formed plasma column would result in both SBS and SRS.

Such an arrangement would also allow for a more systematic approach to the characterization of the scattering phenomena.

4.Simulation Code

To provide a more complete simulation of the laser-heated solenoid, an ionization package should be included. A package similar to that presently being used in the CASTOR code for modelling laser-heated laminar gas jet experiments could be used.

Although, currently, most phenomena seem to be well produced by the code, the effect of ionization on the axial behaviour may be significant.

6.4 Final Conclusions

The laser-heated solenoid apparatus has proven to be a very useful device for scientific investigation.

The experiments performed were very successful in most respects. The most significant findings included the determination of the dependence of the axial propagation of the plasma front on laser intensity and density, the dramatic effect of the focussing ratio on the radial development of the plasma column and the observation of remarkably high levels of SBS and SRS.

The incorporation of a 2-D laser propagation package into the simulation code provided unique results which, in most cases, compared very favourably with the experimental results.

Efficient heating of the plasma by laser beam absorption and effective trapping of the laser beam by the plasma are both necessary in the laser-heated solenoid reactor scheme and both have been clearly demonstrated in this experiment. The very strong levels of stimulated scattering observed in this study indicate that this would be an area of concern in reactor design.

The formation of long, uniform plasma columns supports the development of x-ray lasers based on a device of this type. The success of the simulation study also suggests that, with the inclusion of ionization effects, these codes could provide useful design characteristics for these schemes.

References

Abramowitz, M., and I. A. Segun (1968). *Handbook of Mathematical Functions*, Dover Publications, New York.

Afanas'ev I.U., V.M.Krol', O.N. Krokhin, I.V. Nemchinov (1966). Gasdynamic Processes in Heating of a Substance by Laser Radiation; *P.M.M.* **30**, 1218-1225.

Ahlborn B. (1979). Nernst-Wienecke Equilibrium in Linear Magnetized Plasmas; *Can. J. Phys.* 57, 1090-1093.

Ahlborn B., and W. Liese (1981). Heat Flux Induced Wave Fronts ; *Phys. Fluids* **24**, 1955-1966.

Ahlborn B., and J.D. Strachan (1973). Dynamics of Step Heat Waves in Gases and Plasmas; *Can. J. Phys.* 51, 1416-1427.

Ahlborn B., G.C. Vlases, and Z.A. Pietrzyk (1982). A Scaling Model for Plasma Columns Produced by CO_2 Laser -Induced Breakdown in a Solenoidal Field; *Phys. Fluids* **25**, 2362-2371.

Braginskii, S.I. (1965). Transport Processes in a Plasma , in *Reviews of Plasma Physics, vol.1*, edited by M. A. Leontovich, Consultants Bureau, New York, .

Burnett N.H., and A.A. Offenberger (1974). Magnetohydrodynamic Behaviour of a Laser-Heated Solenoid; *J. Appl. Phys.* **45**, 2155-2162.

Burnett N.H., and A.A. Offenberger (1976). Bleaching Absorption Fronts and Beam Propagation in Laser-Heated Solenoids; *J. Appl. Phys.* **47**, 3377-3379.

Chen, F. (1974). *Introduction to Plasma Physics*, Plenum Press, New York. 329 pp

Cohen, B.I., and C.E. Max (1979). Stimulated Scattering of Light by Ions in a Homogeneous Plasma: Space-Time Evolution; *Phys. Fluids* **22**, 1115-1132.

Cohn, D.R., W. Halverson, B. Lax, C.E. Chase (1972). Effect of Magnetic Field upon Plasmas Produced by Laser-Induced Gas Breakdown; *Appl. Phys. Lett.* **20**, 225-230.

Dawson, J.M. (1964). On the Production of Plasmas by Giant Pulse Lasers; *Phys. Fluids* 7, 981-987.

Dawson, J. (1968). Radiation from Plasmas, in *Advances in Plasma Physics, vol. 1*, edited by A. Simon and W. Thompson, Interscience, New York, .

Dawson, J.M., A. Hertzberg, R. Kidder, G.C. Vlases, H.G. Ahlstrom, and L. Steinhauer (1971). *in Plasma Phys. and Contr. Nuc. Fusion*, I.A.E.A., Madison, WI, 673.

Drake, J.F., P.K. Kaw, Y.C. Lee, G.Schmidt, C.S. Liu, M.N. Rosenbluth (1974). Parametric Instabilities of Electromagnetic Waves in Plasmas; *Phys. Fluids* 17, 778-785.

Dubois, D.F., D.W. Forslund, and E.A. Williams (1974). Parametric Instabilities in Finite Inhomogeneous Media; *Phys. Rev. Lett.* **33**, 1013-1018.

Dufresne, D., P.A. Pincosy, J-P. Caressa, Ph. Bournot, and M. Autric (1979). Experiments on Radiation-Driven Waves Produced during the Production of a Radially Confined Plasma Column, in *Shock Tube and Shock Wave Research*, edited by B. Ahlborn, A. Hertzberg, and D. Russell, University of Washington Press, New York, 569-576.

Estabrook, K., W.L. Kruer, and B.F. Lasinski (1980). Heating by Raman Backscatter and Forward Scatter; *Phys. Rev. Lett.* **45**, 1399-1403.

Evans, D.E., and J. Katzenstein (1969). Laser Light Scattering in Laboratory plasmas; *Rep. Prog. Phys.* 32, 207-271.

Fedosejevs, R., W. Tighe, D.C.D. McKen, and A.A. Offenberger (1981). Stimulated Backscatter from Long Plasma Columns; *Opt. Comm.* **40**, 35-40.

Feit, M.D. and J.A. Fleck (1976). Amplitude and Phase Modulation Accompanying Laser Beam Trapping in Plasmas; *Appl. Phys. Lett.* **29**, 234-236.

Feit, M.D., J.A. Fleck, and J.R. Morris (1977). Propagation of Highly Aberrated Laser Beams in Nonquadratic Plasma Waveguides; *J. Appl. Phys.* **48**, 3301-3306.

Forslund, D.W., J.M. Kindel, and E.L. Lindman (1975). Theory of Stimulated Scattering Processes in Laser-Irradiated Plasmas; *Phys. Fluids* **18**, 1002-1016.

Forslund, D.W., J.M. Kindel, and E.L. Lindman (1975). Plasma Simulation Studies of Stimulated Scattering Processes in Laser-Irradiated Plasmas; *Phys. Fluids* **18**, 1017-1029.

Glasser, J., J. Chapelle, and J.C. Boettner (1976c). Abel inversion applied to plasma spectroscopy: a new interactive method; *Applied Optics* **17**, 3750-3754.

Johnson, L.C., and T.K. Chu (1974a). Measurements of Electron Density Evolution and Beam Self-Focusing in a Laser-Produced Plasma; *Phys. Rev. Lett.* **32**, 517-520.

Johnson, L.C., and T.K. Chu (1974b). Measurements of Electron Density and Laser Beam Self-Focusing of a CO_2 Laser-Induced Plasma in a Strong Magnetic Field; *Bull. Am. Phys. Soc.* **19**, 931.

Johnston, T.W., and J.M. Dawson (1973). Correct Values for High-Frequency Power Absorption by Inverse Bremsstrahlung in Plasmas; *Phys. Fluids* **16**, 722.

Kristiansen, M. and M.O. Hagler (1976). Laser Heating of Magnetized Plasmas; *Nuclear Fusion* **16**, 999-1033.

Krokhin, O.N. (1965). 'Matched' Plasma Heating Mode using Laser Radiation; *Sov. Phys.(Tech. Phys.)* **9**, 1024,1026.

Liu, C.S. and P.K. Kaw (1976). Instabilities in Homogeneous Unmagnetized Plasmas, in *Advances in Plasma Physics, vol. 1*, edited by A. Simon and W. Thompson, Interscience, New York, .

Loter, N.G., D.R. Cohn, W. Halverson, and B. Lax (1975). Beam Self-Trapping and Dynamics of Laser-Induced Magnetoplasmas; *J. Appl. Phys.* **46**, 3302-3309.

Loter, N.G., G.J. Raff, D.R. Cohn, and W. Halverson (1974). Effect of Magnetic Field upon Plasmas Produced by Laser-Induced Gas Breakdown; *J. Appl. Phys.* **45**, 97-104.

Makomaski A.H., and Z.A. Pietrzyk (1980). Two-Dimensional Lagrangian Calculation of a Laser-Heated Solenoid; *Phys. Fluids* **23**, 379-387.

Massey R., K. Berggren, and Z.A. Pietrzyk (1976). Observation of Stimulated Brillouin Backscattering from an Underdense Plasma; *Phys. Rev. Lett.* **36**, 963-966.

Mani, S.A., J.E. Eninger, and J. Wallace (1975). Laser Beam Propagation in a Long Solenoid; *Nuclear Fusion* **15**, 371-375.

McKen, D.C.D, W. Tighe, R. Fedosejevs, and A.A. Offenberger (1982). Dynamics of CO_2 Laser-Heated Solenoids ; *Can. J. Phys.* **60**, 1247-1256.

McMullin, J.N., C.E. Capjack, and C.R. James (1978). Normal Mode Analysis of Laser Beam Propagation in a Plasma Waveguide; *Phys. Fluids* 21, 1828-1831.

McMullin, J.N., C.E. Capjack, and C.R. James (1979a). Normal Mode Analysis with Absorption Effects of a Laser Beam in a Plasma Waveguide; *Phys. Fluids* 22, 953-956.

McMullin, J.N., C.E. Capjack, and C.R. James (1982). Heater: a 2-D Laser Propagation Subroutine for Underdense Plasmas; *Comp. Phys. Comm.* 23, 31-42.

McMullin, J.N., R.D. Milroy, and C.E. Capjack (1979b). Two-Dimensional Magnetic Flux Shell Model for Magnetohydrodynamic Simulations; *Phys. Fluids* 22, 1913-1921.

Meyerand, R.G. Jr, and A.F. Haught (1963). Gas Breakdown at Optical Frequencies; *Phys. Rev. Lett.* 11, 401-406.

Offenberger, A.A. (1977). Axial Heating of Magnetically Confined Plasmas with CO_2 Lasers; *Can. J. Phys.* 55, 412-418.

Offenberger, A.A. (1981). High-Intensity CO_2 Laser-Plasma Interaction Experiments; *Mod. Plasma Phys.* **IAEA-SMR-61/113**, 437-476.

Offenberger, A.A. and N.H. Burnett (1975). CO_2 Laser Breakdown and Heating of Hydrogen in a Magnetic Mirror Field. *In Plasma Phys. and Contr. Nuc. Fusion*, I.A.E.A., New York, 217-228.

Offenberger, A.A., N.H. Burnett, A.R. Strilchuk, and D.F. Way-Nee (1974). Gated Optical Multichannel Analyzer for Ruby Laser Scattering from Plasma; *Rev. Sci. Instrum.* **45**, 1400-1402.

Offenberger, A.A., M.R. Cervenan, and P.R. Smy (1976). CO_2-Laser-Produced Plasma Columns in a Solenoidal Magnetic Field; *J. Appl. Phys.* 47, 494-497.

Offenberger, A.A., M.R. Cervenan, A.M. Yam, and A.W. Pasternak (1976). Stimulated Brillouin Backscattering of CO_2 Laser Radiation from Underdense Plasma; *J. Appl. Phys.* 47, 1451-1458.

Offenberger, A.A., R. Fedosejevs, W. Tighe, and W. Rozmus (1982a). Stimulated Raman Backscatter from a Magnetically Confined Plasma Column; *Phys. Rev. Lett.* 49, 371-375.

Offenberger, A.A., R. Fedosejevs, W. Tighe, and W. Rozmus (1982b). Simultaneous Brillouin and Raman Scattering in CO_2 Laser-Plasma Interaction; *Physica Scripta* T2:2, 498-505.

Oldenburg, D.W., and J.C. Samson (1979). Inversion of interferometric data from cylindrically symmetric refractionless plasmas; *J. Opt. Soc. Am* 69, 927-941.

Phillion, D.W., W.L. Kruer, and V.C. Rupert (1977). Brillouin Scatter in Laser-Produced Plasmas; *Phys. Rev. Lett.* 39, 1529-1533.

Pietrzyk, Z.A., D.W. Scudder, and G. Nelson (1977). Two Temperature Effects in the Laser Heating of Short Plasma Columns; *Phys. Fluids* 20, 1204-1205.

Raizer, Yu. P. (1965). Heating of a Gas by a Powerful Light Pulse; *Sov. Phys.(J.E.T.P.)* 21, 1009-1017.

Raizer, Yu. P. (1977). *Laser Induced Discharge Phenomena*, Plenum Publications, New York.

Ramsden, S.A., and W.E.R. Davies (1964). Radiation Scattered from the Plasma Produced by a Focussed Ruby Laser Beam; *Phys. Rev. Lett.* 13, 227-229.

Ramsden, S.A., and P. Savic (1964). A Radiative Detonation Model for the Development of a Laser-Induced Spark; *Nature* 203, 1217-1219.

Rehm, R. G. (1970). Plasma Motion Induced by High-Intensity Laser Heating; *Phys. Fluids* 13, 921-934.

Rutkowski, H.L., D.W. Scudder, Z.A. Pietrzyk, and G.C. Vlases (1975). CO_2 Laser Heating of Plasma Columns in a Steady Solenoid Field; *Appl. Phys. Lett.* 26, 421-423.

Scudder, D.W. (1979). Laser Driven Breakdown-Heating Waves in Magnetized Hydrogen. *Doctoral Thesis*, University of Washington, Seattle, Wash.. 163pp

Scudder, D.W., Z.A. Pietrzyk, G.C. Vlases, and A.H. Makomaski (1978). A Study of Laser-Induced Plasma Motion in a Solenoidal Magnetic Field, in *Shock Tube and Shock Wave Research*, edited by B. Ahlborn, A. Hertzberg, and D. Russell, University of Washington Press, New York, 561-568.

Shkarofsky, I.P., T.W. Johnston, M.P. Bachynski (1966). *The Particle Kinetics of Plasmas*, Addison-Wesley Publishing Co., New York. 518 pp

Spitzer, L. (1962). *Physics of Fully Ionized Gases*, Interscience, New York.

Steinhauer, L.C. (1975). Plasma Motion Induced by Laser Heating; *Phys. Fluids* 18, 1131-1135.

Steinhauer, L.C. (1976). Laser Beam-Plasma Coupling in Laser Solenoid Plasmas; *Phys. Fluids* 19, 1740-1752.

Steinhauer, L.C. and H.G. Ahlstrom (1971a). One-Dimensional Laser Heating of a Stationary Plasma; *Phys. Fluids* 14, 81-93.

Steinhauer, L.C. and H.G. Ahlstrom (1971b). Propagation of Coherent Radiation in a Cylindrical Plasma Column; *Phys. Fluids* 14, 1109-1114.

Steinhauer, L.C. and H.G. Ahlstrom (1975). Laser Heating of a Plasma in a Solenoidal Magnetic Field; *Phys. Fluids* **18**, 541-545.

Suckewer, S., C.H. Skinner, D.R. Voorhees, H.M. Milchberg, C. Keane, and A. Semet (1983). Population Inversion and Gain Measurements for Soft X-Ray Laser Development in a Magnetically Confined Plasma Column; *IEEE J. Quantum Elec.* **QE-19**, 1855-1859.

Thompson, H.M., R.G. Rehm, and J.W. Daiber (1971). Laser-Driven Waves in a Freely Expanding Gas Jet; *J. Appl. Phys.* **42**, 310-314.

Watt R.W., R.D. Brooks, and Z.A. Pietrzyk (1978). Observation of Stimulated Raman Scattering from a Preformed, Underdense Plasma; *Phys. Rev. Lett.* **41**, 170-173.

Watt R.W. and Z.A. Pietrzyk (1980). Measurement of Stimulated Raman Scattering from Magnetically Confined Underdense Plasmas; *Appl. Phys. Lett.* 37, 1068-1070.

Wheeler, C.B., and A.E. Dangor (1973). Multiply Crowbarred Solenoids for Plasma Research; *J. Phys. E: Sci. Inst.* **6**, 332-338.

Yasutomo, Y., M., Katsuyuki, S.-I. Himeno, T. Enoto, and, Y. Ozawa (1981). A New Numerical Method for Asymmetrical Abel Inversion; *IEEE Trans. Plasma Sci.* **PS-9**, 18-21.

Yeun, S.Y., B. Lax, and D.R. Cohn (1975). Laser Heating of a Magnetically Confined Plasma; *Phys. Fluids* **18**, 829-835.

Zel'dovich, Ya. B., and Yu. P. Raizer (1968). *Elements of Gas Dynamics and the Classical Theory of Shock Waves*, Academic Press, New York.